



8-2021

Design and Experimental Evaluation of a Small-Scale Buckling Restrained Brace Analog

Lindsay K. Helferich

University of Tennessee, Knoxville, lhelferi@vols.utk.edu

Follow this and additional works at: https://trace.tennessee.edu/utk_gradthes



Part of the [Structural Engineering Commons](#)

Recommended Citation

Helferich, Lindsay K., "Design and Experimental Evaluation of a Small-Scale Buckling Restrained Brace Analog." Master's Thesis, University of Tennessee, 2021.

https://trace.tennessee.edu/utk_gradthes/6164

This Thesis is brought to you for free and open access by the Graduate School at TRACE: Tennessee Research and Creative Exchange. It has been accepted for inclusion in Masters Theses by an authorized administrator of TRACE: Tennessee Research and Creative Exchange. For more information, please contact trace@utk.edu.

To the Graduate Council:

I am submitting herewith a thesis written by Lindsay K. Helferich entitled "Design and Experimental Evaluation of a Small-Scale Buckling Restrained Brace Analog." I have examined the final electronic copy of this thesis for form and content and recommend that it be accepted in partial fulfillment of the requirements for the degree of Master of Science, with a major in Civil Engineering.

Nicholas E. Wierschem, Major Professor

We have read this thesis and recommend its acceptance:

Mark D. Denavit, Timothy J. Truster

Accepted for the Council:

Dixie L. Thompson

Vice Provost and Dean of the Graduate School

(Original signatures are on file with official student records.)

Design and Experimental Evaluation of a Small-Scale Buckling Restrained Brace Analog

A Thesis Presented for the
Master of Science
Degree
The University of Tennessee, Knoxville

Lindsay Kaye Helferich
August 2021

Acknowledgements

The work contained in this thesis would not have been possible without guidance and support from a multitude of people. I would first like to thank my advisor and committee chair, Dr. Nicholas Wierschem, for his continued mentoring over the past 2 years. His patience and skill at explaining complex concepts continually improved my understanding of pertinent topics. His focused mentoring in every phase of the process provided me the assistance I needed in researching, writing, and presenting. I would also like to thank Dr. Mark Denavit, who is the PI for the overall project and was also a member of my committee. His insight during all stages of the design development process was invaluable. I also want to thank Dr. Timothy Truster for serving as a committee member and providing me with explanations regarding the numerical modeling process. In addition, I would like to thank the National Science Foundation for providing funding for the project this work was a part of.

The experimental portion of this work was supported by many people. I want to thank Dr. Dayakar Penumadu for the use of his laboratory and testing equipment. I also want to thank Andy Baker and Larry Roberts for fabricating all the parts required for the experimental tests. Last but certainly not least, I want to thank Zach Arwood for his patience and assistance during all experimental tests conducted. The experimental evaluation of this device would not have been possible without the help of all of these individuals.

Finally, I would like to thank the friends and family who supported me and believed in me this entire time. A special thank you goes to my wonderful fiancé, Austin Kirk, for sharing in both the discouraging and exciting times and always having the words to say to bring a smile to my face. I also want to thank my parents, Mark and Beverly Helferich, for their support of my endeavors and for their love and encouragement that was felt all the way from Texas. Most of all, I would like to thank God for granting me the insight necessary to understand and solve many challenging problems. He blessed me with this opportunity and provided a way to complete the work I was given to do. Without Him, I am nothing.

Abstract

In the event of an earthquake, structures experience large lateral loads that can lead to weak story mechanisms and result in premature building collapse. Strongback braced frames (SBF) are a type of seismic force resisting system that aim to evenly distribute horizontal loads up the height of the building to mitigate this failure mechanism. Previous research shows that SBFs are a promising way to better design for seismic demands, but these systems have not been fully explored to best exploit the design space. This work is a part of a project that aims to provide both numeric and experimental verification of these SBF systems.

An important component of the SBF is the inelastic energy dissipating element. Often, this component is designed as a buckling restrained brace (BRB). As part of the experimental test set up, a small-scale BRB must be designed and tested. This thesis explains the relevance of the BRB to the project as a whole, discusses the scaling and design decisions that were made during initial prototyping, and presents initial results that suggest a small-scale device can effectively simulate the behavior of its full-scale counterpart. Following these initial tests, numerical modeling and experimental testing of a further improved design provides validation of device functionality over a range of brace strengths and stiffnesses. This work is instrumental in providing small-scale analogs of BRBs for future testing of SBFs and could be utilized by others to simulate the effects of other energy dissipating elements in the full-scale and small-scale experimental testing of structures.

Table of Contents

1	Introduction.....	1
2	Literature Review & Scaling Laws.....	4
2.1	Strongback Braced Frames	4
2.2	Buckling Restrained Braces.....	5
2.2.1	Conventional Buckling Restrained Braces.....	5
2.2.2	Alternative Buckling Restrained Braces	7
2.3	Small-Scale Experimental Testing.....	11
2.3.1	Similitude Theory	11
2.3.2	Shake Table Tests	13
2.3.3	Limitations of Small-Scale Testing.....	15
2.3.4	BRB Testing.....	16
3	Small-scale BRB Analog.....	20
3.1	Scaling from Prototype to Model.....	20
3.1.1	Prototype Geometry & Seismic Weight.....	20
3.1.2	Project Scaling Laws.....	21
3.1.3	Prototype Yield Strength & Stiffness.....	23
3.2	Functionally Similar, Geometrically Dissimilar Model.....	26
3.2.1	Initial Model.....	26
3.2.2	Fabrication Error Considerations	29
3.2.3	Second Iteration Model.....	31
3.2.4	Limitations of the Predictive Equations.....	33
3.3	Physical Design of the Circular BRB	33
3.3.1	Yielding Plate Design	35
3.3.2	Assembled Test Mechanism	35
4	Numerical Modeling.....	38
4.1	Initial Finite Element Model.....	38
4.1.1	Idealization of ABAQUS Boundary Conditions.....	38
4.1.2	Material Model for Initial Results.....	39
4.1.3	Element Type Selection	39
4.1.4	Mesh Refinement Study.....	41
4.2	Sizing the Initial Physical Specimens	42

5	Experimental Tests	47
5.1	Coupon Tests	47
5.2	Quasi-static BRB Testing.....	50
5.2.1	Testing Protocol for Initial Tests	50
5.2.2	Instrumentation	54
5.2.3	Initial Test Results	54
5.2.4	Testing Protocol for Second Tests	62
5.2.5	Connection Revisions and Second Test Results	62
5.3	Conclusions Based on Experimental Tests	68
5.3.1	Impact of Manufacturing Tolerances	68
5.3.2	Experimental Observations & Overview of Model Updating.....	70
6	Model Updating	72
6.1	Isotropic and Kinematic Hardening	72
6.1.1	Differences in the Hardening Models	72
6.1.2	Purely Isotropic Hardening	72
6.1.3	Bilinear Kinematic Hardening	74
6.1.4	Multilinear Kinematic Hardening Model.....	77
6.2	Combined Isotropic and Kinematic Hardening.....	79
6.3	Nonlinear Geometric Effects	84
7	Updated Model: The Rectangle-Type BRB.....	88
7.1	Conceptual and Physical Design.....	88
7.1.1	Targeted Improvements	88
7.1.2	Conceptual Validation.....	89
7.2	Parameter Calibration	89
7.2.1	The Initial Form of the Empirical Equations	91
7.2.2	Qualitative Basis for Predictive Equations	92
7.2.3	Suite of ABAQUS Analyses	97
7.2.4	Results of Regression Analysis.....	97
7.2.5	In-Bounds Test Set.....	99
7.2.6	Out-of-Bounds Test Set	100
7.2.7	Conclusions Drawn based on Empirical Equations	103
7.3	Experimental Testing of the Rectangle-type BRB.....	103
7.3.1	Small Rectangle-type BRB Experimental Results	106

7.3.2	Large Rectangle-type BRB Experimental Results	111
7.4	Conclusions on the Rectangle-type BRB	113
8	Conclusions & Future Work	116
	References	118
	Appendix A	121
	Appendix B	136
	Vita	146

List of Tables

Table 1. Scaling ratios used in previous shake table tests.....	14
Table 2. Dead loads for the prototype building.	22
Table 3. Project scaling ratios.	22
Table 4. Yield force and elastic stiffness values for prototype and model BRBs.....	25
Table 5. Initial model BRB geometry.....	30
Table 6. Comparison of parameters for 1 st and 2 nd model iteration.	34
Table 7. Mesh Refinement Analysis - Calculated Parameters.....	43
Table 8. Width and radius of circular-type BRBs using initial predictive equations.....	46
Table 9. Percent error in parameters of interest using initial predictive equations.....	46
Table 10. Geometry and predicted values for final experimental specimens to 3 significant figures.	46
Table 11. Calculated values for coupon tests.....	49
Table 12. Calculated values for Δ_{bm} . Values reported in inches.	53
Table 13. Calculated parameter values for large experimental BRBs.	69
Table 14. Measured manufacturing tolerances.	71
Table 15. Simplified stress-strain tabular input for kinematic hardening calibration.	82
Table 16. Isotropic hardening parameters.....	83
Table 17. Midspan deflection and moment for different support and loading conditions.	93
Table 18. Training data for empirical equations.	98
Table 19. "In-bounds" test data set.	101
Table 20. Out-of-bounds test data set.	104
Table 21. Waterjet tolerance for rectangle-type BRB specimens.	107
Table 22. ABAQUS estimated parameter values for BRB using predictive equations.	107
Table 23. ABAQUS estimated parameter values for BRB using experimental geometry.....	107
Table 24. Cyclic experimental results vs. cyclic ABAQUS results – small specimen.	108
Table 25. Cyclic experimental results vs. cyclic ABAQUS results - large specimen.....	114

List of Figures

Figure 1. Schematic representation of an SBF.....	2
Figure 2. Hysteretic curve of a typical buckling steel brace vs. a BRB.....	6
Figure 3. Diagram of a conventional BRB.	6
Figure 4. Alternative all steel BRB design, Type I.....	8
Figure 5. Alternative all steel BRB design, Type II.....	8
Figure 6. Potential buckling modes of the BRB.	9
Figure 7. YBS prototype. YBS component (left) and full scale frame (right).....	9
Figure 8. Yielding finger design of the YBS connector.....	10
Figure 9. Schematic two-step similitude process for geometrically dissimilar models.	17
Figure 10. Plan view of prototype building layout with moment frames designed in this study highlighted.	22
Figure 11. Beam bending model.....	27
Figure 12. Schematic of yielding plate design using the beam model.....	30
Figure 13. Circular bending model.....	32
Figure 14. Physical model of the BRB yielding plate. Plan view.....	36
Figure 15. Assembled test mechanism for small-scale BRB.....	36
Figure 16. Two-dimensional ABAQUS model of yielding plate.	40
Figure 17. True stress vs. true plastic strain curve for ABAQUS input.....	40
Figure 18. Calculation of parameters for mesh refinement study.....	43
Figure 19. Graphical Representation of Mesh Refinement Study.....	44
Figure 20. Sheet-type coupon for tensile testing.....	49
Figure 21. Nominal stress-strain behavior of 11 gauge A1011-CS-B steel.....	49
Figure 22. Representative stress-strain behavior.	51
Figure 23. Displacement control for specimen T1S2.....	55
Figure 24. Test setup & bolt layout.....	56
Figure 25. Force vs. displacement curve of specimen T1S1.....	57
Figure 26. Out-of-plane buckling of T1S1.....	57
Figure 27. Force vs. displacement curve of specimen T1S2. Bolts C1-C4 tightened.....	59
Figure 28. Force vs. displacement curve of specimen T1S2. Bolts C1-C4 loosened.	60
Figure 29. Disassembly of components showing wear on the contact surface (circled in red).	60
Figure 30. Force vs. displacement curve of specimen T1S3.....	61
Figure 31. First story of frame shown at prescribed story drift.	63

Figure 32. Displacement control for specimen T2S3.....	63
Figure 33. Initial improved connection.....	64
Figure 34. Initial flag shaped hysteresis of T2S2.....	66
Figure 35. Connection detail with tape removed.	66
Figure 36. Full hysteretic curve of T2S2 - No Tape.	67
Figure 37. Hysteretic curves of all large BRB specimens.	69
Figure 38. Schematic representation of (a) kinematic hardening and (b) isotropic hardening.	73
Figure 39. Isotropic hardening model from previous FE analysis.	73
Figure 40. Comparison of kinematic hardening moduli using different calibration points.	75
Figure 41. Average maximum strain in yielding plate. Ring only with no elements shown for clarity.	75
Figure 42. Bilinear kinematic hardening.....	76
Figure 43. Multilinear kinematic hardening model.....	78
Figure 44. Graphical representation of multiple backstresses defining kinematic hardening component. .	80
Figure 45. Visualization of parameters for isotropic hardening calibration.	82
Figure 46. Simplified stress-strain data for ABAQUS model.....	82
Figure 47. Combined hardening model.....	83
Figure 48. Deformed shape in tension (top) and compression (bottom). Showing contours for von Mises stress.....	85
Figure 49. Analytical hysteretic curves including nonlinear geometric effects vs. experimental results. ..	87
Figure 50. Force vs. displacement of square specimen using improved numerical model.	90
Figure 51. Physical rectangle-type device labeled with important design parameters. Only central yielding square shown for clarity of dimensions.	90
Figure 52. Comparison of x- (left) and y-direction (right) stresses for L = 2.00 in. and b = 0.15 in. Stress in psi.....	95
Figure 53. Comparison of x- (left) and y-direction (right) stresses for L = 2.00 in. and b = 0.35 in. Stress in psi.....	95
Figure 54. Original error in calculated yield force for in-bounds test data.	101
Figure 55. Error in calculated yield force when considering width correction factor.....	102
Figure 56. Percent error in stiffness estimation of all data points.....	104
Figure 57. Percent error in yield force estimation of all data points.....	105
Figure 58. Percent error in yield displacement estimation of all data points.	105
Figure 59. Graphical comparison of initial cyclic behavior for small rectangle-type BRB.....	108
Figure 60. Comparison of entire hysteresis for small rectangle-type BRB.	110
Figure 61. Updated connection detail to resist slip.....	112

Figure 62. Graphical comparison of initial cyclic behavior for large rectangle-type BRB. 114
Figure 63. Comparison of entire hysteresis for large rectangle-type BRB. 115
Figure 64. Comparison of small and large BRB experimental hysteretic curve..... 115

Chapter 1

1 Introduction

The main subject of this thesis is the numerical modeling and experimental testing of a small-scale buckling restrained brace (BRB) analog. However, this device is only one component of a larger experimental and analytical project entitled “Dual System Strongback Designs for Seismic Damage-Resistant Structures”. The overall project is one that experimentally verifies numeric simulations that quantify the behavior of different strongback braced frame (SBF) configurations. This work will aid in the advancement of using SBFs as seismic force resisting systems (SFRS) to lessen both the economic and structural impact to buildings during a large seismic event. A strongback, shown schematically in Figure 1, has two main parts – an elastic “spine” and an inelastic energy dissipating element. Often, the inelastic energy dissipating elements are BRBs. Proper functionality of these BRBs is critical to the overall performance of the SBF because these elements are the primary resistance to the inelastic lateral loads placed on the structure. Therefore, a small-scale analog for this device is a crucial portion of the overall experimental design.

There is extensive literature on the experimental testing and optimization of full-scale BRBs. There are also a number of papers that discuss small-scale modeling of concrete building systems and some that experimentally verify small-scale steel SFRS. However, to the best of the knowledge of the author, there has been little work focused on small-scale testing of BRBs. The small-scale tests that have been done are still large compared to the scale this project requires. This work will therefore address the need for a verified small-scale inelastic energy dissipation device that accurately mimics the behavior of its large-scale counterpart at deformation levels up to those expected during design level earthquake ground motions.

The subsequent chapters present the design process and final outcome of the small-scale model BRB. There were multiple significant pieces of the project performed simultaneously to efficiently work towards achieving the desired result. In order to clearly convey the findings of this work, the discussion is ordered linearly even though the workflow was completed in a nonlinear fashion. Chapter 2 provides an in-depth literature review and explains the basis of scaling laws used in design. Chapter 3 presents the initial conceptual design of the small-scale BRB, discusses the flaws noted, and concludes with an improved conceptual design paired with the actual physical realization of the specimen. Chapter 4 introduces the finite element analysis used to refine the physical model. Chapter 5 discusses results of both material

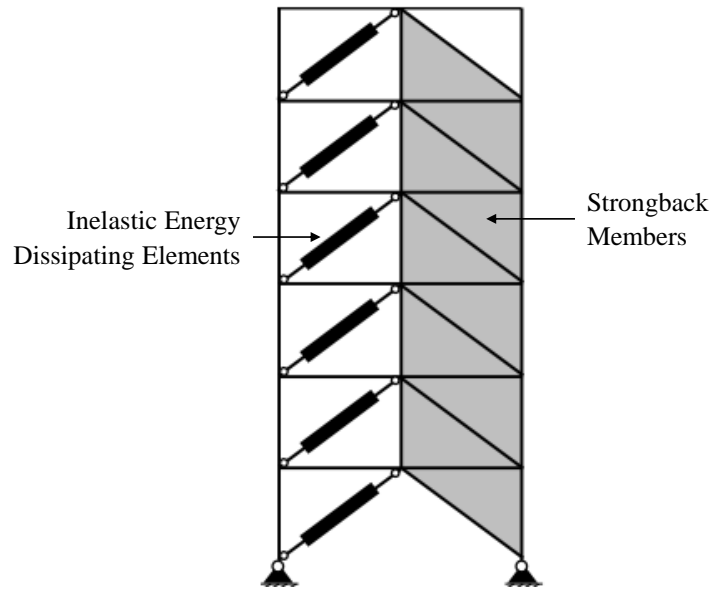


Figure 1. Schematic representation of an SBF.

coupon tests and experimental testing of the physical model. Chapter 6 provides an updated material model that addresses the inconsistencies between the initial material model and the experimental results. Chapter 7 then provides a different physical design that utilizes the strengths of previous models and mitigates the weaknesses identified via experimental testing. Finally, chapter 8 draws conclusions about device functionality and proposes potential pathways for future work.

Chapter 2

2 Literature Review & Scaling Laws

There is extensive literature available regarding SBF systems, BRB designs, and small-scale testing. This chapter begins by explaining the design goals of the SBF that provide a basis for the motivation of the overall project. Then, a review of the currently available large-scale BRB device designs is presented. While not at a scale applicable for this work, the design concepts upon which these large-scale devices are based aided greatly in the conceptual formulation of the small-scale product. Following this is a review of the accepted similitude laws that govern small-scale modeling, a summary of relevant shake table tests and the scaling factors used, and acknowledgement of the potential sources of error in this type of testing. To conclude this chapter, the gap in literature surrounding small-scale testing of BRBs is addressed and constructability concerns that guided the continued design of the device are discussed.

2.1 Strongback Braced Frames

As mentioned in the previous section, this work is a portion of a larger project that aims to quantify the contributions of different SBF elements to the earthquake resilience of structures. Because SBFs are not the main focus of this work, an in-depth literature review is not provided for this topic. However, understanding the functionality of these systems is necessary to understand the importance of the BRB. There are many options for SFRS, and each have strengths and weaknesses. One of the weaknesses of conventional buckling restrained braced frames (BRBF) is that they are subject to weak story mechanisms that undermine the ability of the structure to safely resist seismic load. These weak-story mechanisms occur when there is rapid loss of strength and stiffness in the braces after yielding has occurred. This leads to a concentration of load demand in the weakened member and a premature failure of the structure due to brace collapse.

To counter this, a different type of SFRS, called a strongback braced frame, has been introduced and is being studied. SBFs are comprised of two main components – a rather stiff, elastic “spine”, known as a strongback, and inelastic energy dissipating elements. The strongback truss is designed to remain elastic throughout the entirety of a seismic event, allowing it to distribute loads more evenly along the height of the building and thus preventing failure of one or a select few brace members (Simpson and Mahin 2018a; b). Energy is dissipated by specially designed inelastic elements along the height of the building. Often, these elements are BRBs. In order to meet the goal of experimentally verifying the SBFs, a scale model of

such a system must be constructed and tested on the shake table facility at the University of Tennessee. Because of shake table size and weight restrictions, the experimental portion of this project must be performed at a small-scale. Therefore, all components must be designed and tested to ensure they produce the small-scale analog of the prototype behavior.

2.2 Buckling Restrained Braces

The component of interest in this thesis is the inelastic energy dissipating element – the buckling restrained brace (BRB). There are several different BRB designs, but they all have a common feature – stable, repeatable hysteretic behavior. They are designed in such a way that the steel brace core is prevented from buckling and can therefore reach much higher axial forces than traditional steel braces, which are significantly affected by buckling (Dehghani and Tremblay 2018). Because of this, BRBs are often used as the inelastic energy dissipating element in SBFs. Figure 2 shows the full hysteretic curve characteristic of a typical BRB using a solid line and the undesirable hysteretic curve of a typical buckling steel brace using the dashed line. The difference in these two curves lies in the compression behavior of the brace. It is commonly known that slender members cannot support the same axial load in compression that they can in tension due to global buckling. This causes the area under the hysteretic curve to be low on the compression side, meaning that the energy dissipated is reduced. The buckling behavior is also a failure mechanism that can lead to weak story collapse. The BRB improves the energy dissipation of the brace by providing transverse restraint that prevents global buckling. Typically, this design actually raises the compression capacity slightly higher than the tension capacity due to the steel core interacting with the outer restraining mechanism during local buckling in compression.

BRBs consist of two main components – a steel core and a restraining mechanism. The steel core will extend out of the restraining mechanism to form connections with other framing members. Tensile and compressive forces are resisted mainly by the restrained portion of the steel core. Because of Poisson's effect, the steel core will expand laterally during compression. Therefore, a small gap is left between the restraining mechanism and the steel core. There is also a debonding agent applied to the steel surface to decrease frictional interaction between the restraining mechanism and the steel core (Talebi et al. 2014). This lowers any contribution from the restraining mechanism to the overall axial strength.

2.2.1 Conventional Buckling Restrained Braces

Both conventional and alternative BRBs have a yielding mechanism and a restraining mechanism. A conventional BRB is shown in Figure 3. The restraining mechanism used is a concrete filled steel casing. The yielding mechanism is the steel core, which has three distinct areas: the yielding region, transition

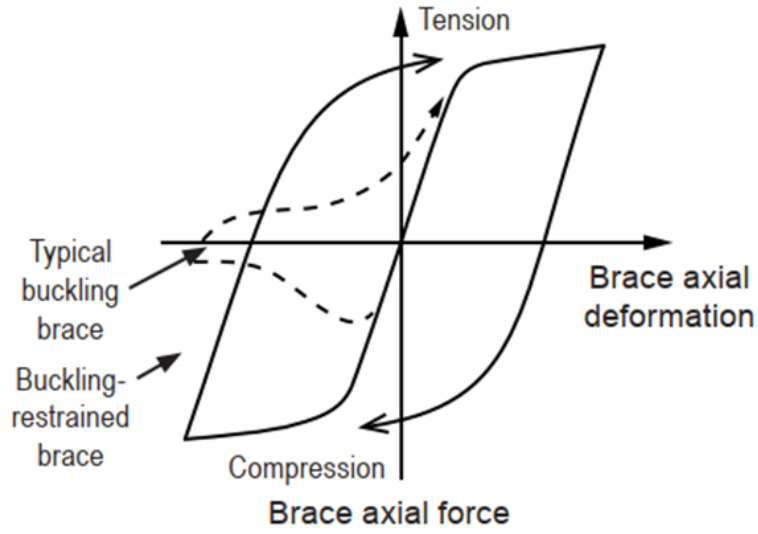


Figure 2. Hysteretic curve of a typical buckling steel brace vs. a BRB.

Reproduced from (Kersting et al. 2016)

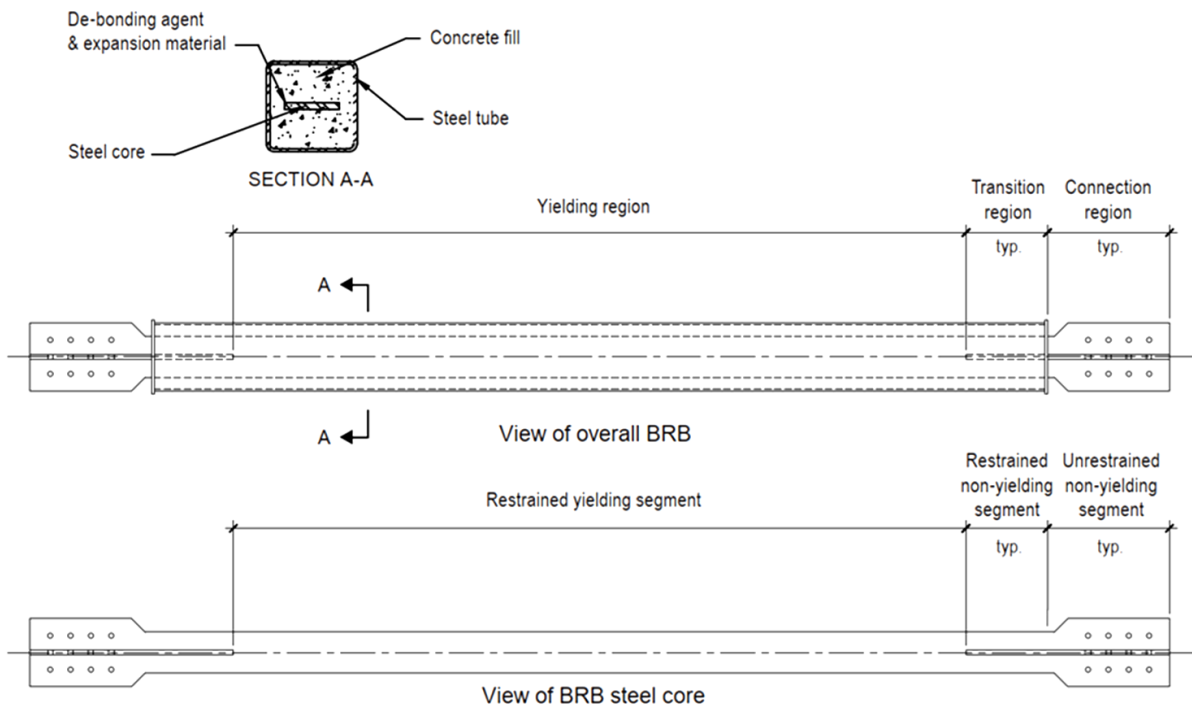


Figure 3. Diagram of a conventional BRB.

Reproduced from (Kersting et al. 2016)

region, and connection region. The specific design of the core concentrates deformation in the yielding region. The transition region and connecting region are stiffened so as to ensure stable elastic response in the portion of the core that is unrestrained (Tremblay et al. 2004).

2.2.2 Alternative Buckling Restrained Braces

Although Figure 3 is the typical design used for BRBs, there are alternative designs presented in the literature that have also proven to provide the full, stable hysteretic curve shown in Figure 2. The first of these designs follows the same basic design presented previously but employs steel members as the restraining mechanism rather than the typical concrete filled steel tube. The steel restraining mechanism can use a combination of steel plates and HSS members (Dehghani and Tremblay 2018; Koetaka et al. 2001), or may only use a specially fabricated steel plate (Jia et al. 2017). Figure 4 and Figure 5 show the layout of these all steel BRBs.

Experimental tests were done on the all steel BRB designs to confirm the desired hysteretic behavior and determine the effect of changing different design parameters. According to Dehghani and Tremblay (2018), there was no recommended debonding agent, but it was noted that the lack of proper detailing and lubrication can lead to a significant increase in compressive axial force. The performance of the steel restraining mechanism also depended on the spacing of the bolts connecting the restrainer plates. When the spacing was less than required, the core could experience both strong and weak axis buckling, as seen in Figure 6. This shows that once the main buckling mode of a slender element is constrained, there are other buckling modes that may become important, such as higher mode buckling or strong axis buckling.

A second alternative type of buckling restrained brace found in the literature does not use a restraining mechanism along the core area of the brace. This brace does not buckle because it is not a slender member. This design utilizes a specially designed Yielding Brace System (YBS) connector at the end of a typical wide-flange brace member to produce the desired hysteretic behavior. The design is shown in Figure 7 and Figure 8. It concentrates plastic deformation in a series of yielding fingers that bolt into slotted holes at the end plate connection. The yielding fingers then undergo flexural bending during a seismic event. The shape of the yielding fingers is meant to promote plasticity along the entire length of the finger. The YBS geometry was designed using first principles in mechanics and confirmed with quasi-static cyclic testing (Gray et al. 2012, 2017). This design provided a theoretical basis for the work presented in the remainder of this thesis.

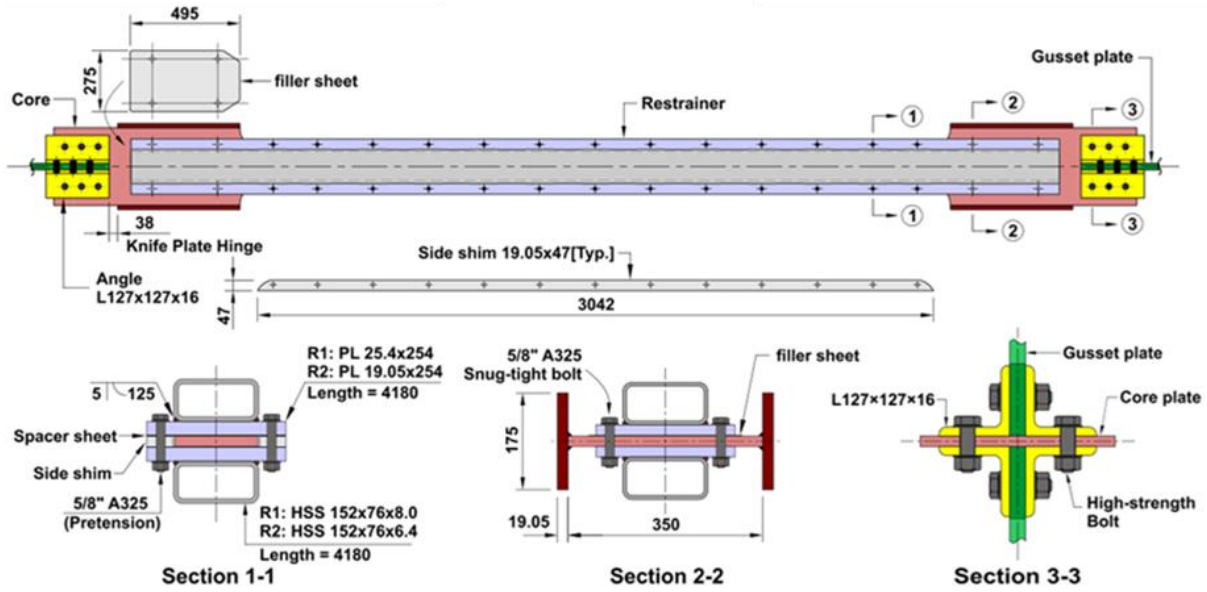


Figure 4. Alternative all steel BRB design, Type I.

Reproduced from (Dehghani and Tremblay 2018)

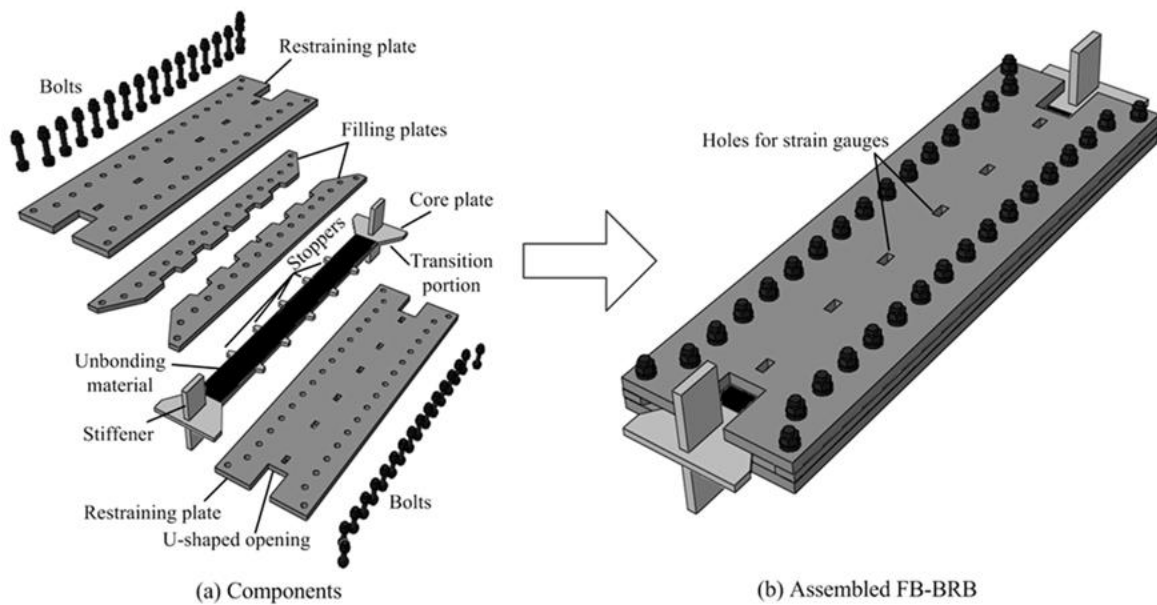


Figure 5. Alternative all steel BRB design, Type II.

Reproduced from (Jia et al. 2017)

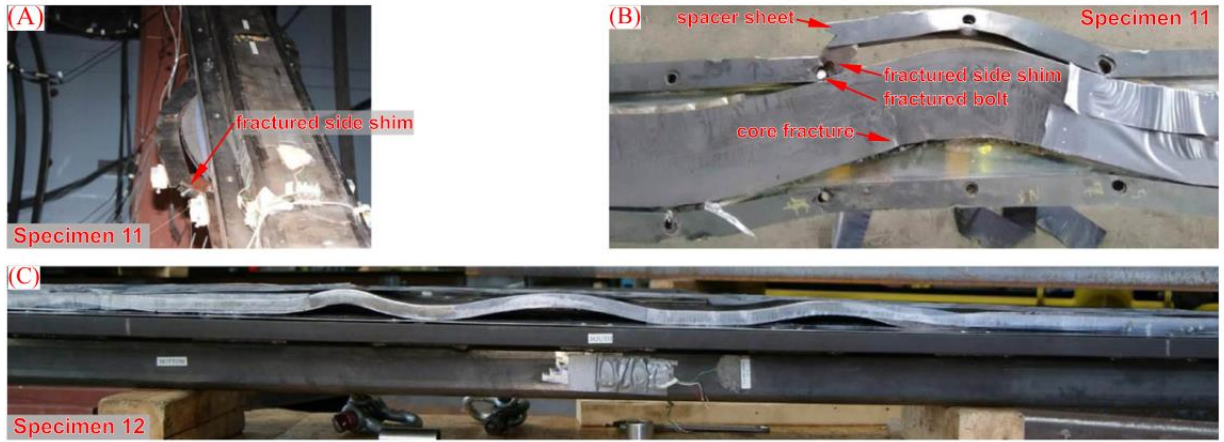


Figure 6. Potential buckling modes of the BRB.

Figure (A) and (B) show strong axis buckling of the core; Figure (C) shows higher mode weak axis buckling of the core

Reproduced from (Dehghani and Tremblay 2018)



Figure 7. YBS prototype. YBS component (left) and full scale frame (right).

Reproduced from (Gray et al. 2012)

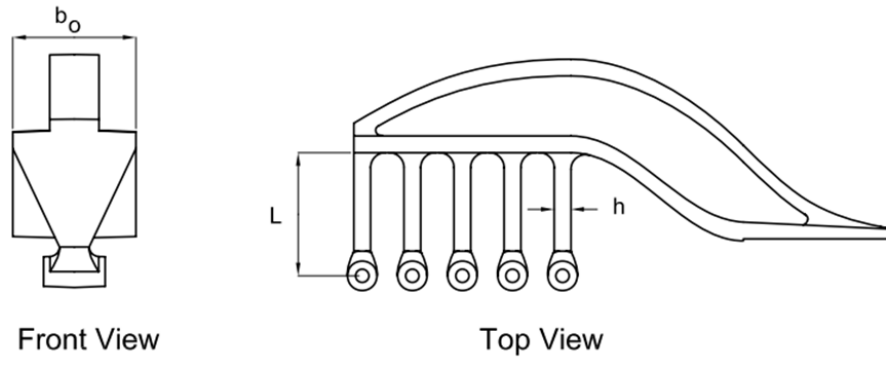


*Figure 8. Yielding finger design of the YBS connector
Reproduced from (Gray et al. 2012)*

2.3 Small-Scale Experimental Testing

2.3.1 Similitude Theory

While there is an absence of literature discussing small-scale BRB testing at the magnitude of scaling required for this project, there is an abundance of literature exploring the topic of similitude. Similitude provides a basis for creating a useful model. A model is a device related to the physical system (prototype) in such a way that observations made on the model may be used to accurately predict the performance of the physical system (Murphy 1950). These models can be created by a variety of different methods, but the most useful and general method is that of dimensional analysis. This tool is widely used across many engineering disciplines and has been discussed in many resources. What is now known as the Buckingham Pi Theorem is the accepted basis for performing dimensional analysis (Buckingham 1914). A summary of the methodology of dimensional analysis and its applicability to modeling is provided below (Casaburo et al. 2019; Murphy 1950).

Similitude theory has its basis in dimensional analysis. Dimensional analysis takes into account the knowledge that physical variables can be represented by a set of basic units. These basic units are often taken as mass (M), length (L), and time (T), but for engineering purposes, force (F) is sometimes used in place of mass. There are a set number of physical variables that can be used to fully represent a system. Using the Buckingham Pi Theorem, N number of physical variables that are represented by K basic units can be translated from their original form into $(N - K)$ non-dimensional variables, known as Π terms. This reduces the number of independent variables to be experimentally validated for a given problem. Because each Π term is dimensionless, they can be used as a general tool to equate model and prototype behavior. Scale modeling using these Π terms requires that the following be true:

$$\Pi_i^{(m)} = \Pi_i^{(p)} \text{ for } i = 1, 2, \dots, (N - K)$$

This provides proportionality constants for the important physical variables between the prototype and the model. An example is shown in order to make the concept clear.

One of the Π terms that can be obtained in the case of structural analysis is $\frac{P}{El^2}$, where P represents an axial load, E represents Young's modulus, and l represents an arbitrary length defining the scale of the system. Using F, L, and T as the basic units for this example, the three physical variables can be expressed as $P = [F]$, $E = [FL^{-2}]$, and $l = [L]$. Therefore, the Π term is dimensionless. Setting the Π term for model and prototype equal to each other, the following is obtained:

$$\frac{P_m}{E_m l_m^2} = \frac{P_p}{E_p l_p^2}$$

$$P_m = P_p \left(\frac{E_m}{E_p} \right) \left(\frac{l_m}{l_p} \right)^2$$

The ratio $\frac{E_m}{E_p}$ is defined as the modular ratio, E_r , and the ratio $\frac{l_m}{l_p}$ is defined as the length ratio, L_r . These ratios are independent from each other and therefore do not have to equal the same value. The equality relating the axial force in the model to the axial force in the prototype can then be rewritten.

$$P_m = P_p E_r L_r^2$$

The problem could be continued by equating other Π terms and solving for ratios that define the necessary scaling of all physical variables. Only as many ratios as there are basic units can be arbitrarily chosen based on physical constraints of the model. All other ratios are dependent on these K independent ratios. This method is generally applicable to many problems, but it requires a deep knowledge of the problem at hand to determine the important physical variables to include in the analysis. Inclusion of physical terms that do not heavily influence parameters under investigation can lead to unnecessary constraints on the model formulation (Casaburo et al. 2019).

Another method of dimensional analysis that has been used (Torkamani et al. 2008) and is similar to the Buckingham Pi Theorem applies similitude theory to the governing equations of a problem (Casaburo et al. 2019; Coutinho et al. 2016). Instead of equating general Π terms, this method equates a governing physical equation for the prototype to the same governing physical equation for the model. The scaling ratios are then determined in the same manner presented above. This method can be used to define all scaling ratios pertinent to a problem in order to achieve either complete or partial similarity. Depending on the complexity of the problem, complete similarity may not be achievable, but partial similarity can still be useful as long as the concessions made in scaling are carefully considered.

No matter the method chosen for dimensional analysis, it is important to recognize the limitations of the model and the implications of any assumptions made during the scaling process. In some cases, the limitation is physical, such as a space constraint in the testing facility limiting the additional weight that could be added to the specimen at specified locations (Li et al. 2006). In this case, the implications are that the model is somewhat distorted and the scaling parameters that depend on mass must be revised. In other cases, the limitation may lie in the control system being used. If the time ratio is not defined by the user,

similitude may require that time be compressed (and therefore frequency be increased) for proper dynamic input (Kim et al. 2004). Depending on the time history of the prototype ground motion and the maximum input frequency of the control, this can be a limitation that needs to be considered. A third limitation to consider is the practicality of a true model. A true model is one in which no similitude law is violated. If there is any relaxation of the similitude requirements, the model is said to be distorted. It is most often the case that a model is somewhat distorted, but this can still lead to accurate results as long as the expected behavior of the model is known beforehand (Wissmunn 1968). A pertinent example of this is given in the complexity of scaling all compatibility and equilibrium equations, boundary conditions, etc. from a supertall prototype building to a model structure. While exact replication is impractical, the study of seismic effects is most dependent on the similarity of the lateral force resisting system (Lu et al. 2012). Therefore, exact replication could reasonably be sacrificed for the sake of proper simulation of lateral resistance.

2.3.2 Shake Table Tests

There have been many small-scale shake table tests conducted for multi-story structures using both steel and reinforced concrete members. While all of these tests differ in the ratio values chosen for modeling purposes, they are all similar in the fact that they utilize similitude scaling laws. Below is a list of the tests referenced with a short description of the testing goal. Table 1 lists the defined and calculated scaling factors used in each listed experiment. It is important to note that this is by no means an exhaustive list of all shake table experiments, but it does adequately explore the use of similitude in shake table testing for the purposes of this project.

- Small-scale testing of low-rise base isolated structures under seismic loads (Chung et al. 1999)
- Small-scale testing to experimentally validate the use of transfer plate design in high-rise building systems (Li et al. 2006)
- Small-scale testing to experimentally test the effect of viscous wall dampers on reinforced concrete structures (Lu et al. 2008)
- Collapse testing of small-scale steel moment resisting frames (Lignos 2008)
- Small-scale testing of seismic performance of the Shanghai Tower (Chunyu et al. 2012)
- Small-scale testing to experimentally validate the use of transfer stories in the design of supertall structures (Lu et al. 2012)

The range of tests presented from the literature vary widely in size – from 1:2 length scale up to 1:40 length scale. This wide range of accepted shake table length ratios shows that it is possible to gather valid data from very small-scale tests. However, one must take into account the differences in selected ratios between these tests. As previously discussed, similitude theory only allows the designer to choose as many ratios as

Table 1. Scaling ratios used in previous shake table tests.

Ratios shaded in blue are independently chosen. All other ratios are dependently calculated.

Author & Year	Length Ratio	Acceleration Ratio	Modular Ratio	Mass Density Ratio	Stress Ratio	Mass Ratio	Force Ratio	Time Ratio
Chung et al. 1999	0.250	1.00	1.000	4.00	1.000	0.0625	0.0625	0.500
Li et al. 2006	0.050	1.16	0.177	3.04	0.177	0.0004	0.0004	0.207
Lu et al. 2008	0.500	1.00	1.000	2.00	1.000	0.2500	0.2500	0.707
Lignos 2008	0.125	1.00	1.000	8.00	1.000	0.0156	0.0156	0.354
Chunyu et al. 2012	0.025	2.40	0.313	5.20	0.313	0.0001	0.0002	0.102
Lu et al. 2012	0.033	2.50	0.370	4.44	0.370	0.0002	0.0004	0.115

there are pertinent basic units. All other pertinent ratios are subsequently calculated based on the chosen values. All 6 papers defined a length scale as the geometric scaling constraint. Following this decision, there are mixed usages of material constraints, loading constraints, and dynamic constraints. For example, Chunyu et al. (2012) bases the length scale on the size constraints of the shake table, then chooses a modular scale based on the differing material properties between the prototype and model. Finally, the mass density ratio is chosen based on the bearing capacity of the shake table. The subsequently calculated parameters include the time, acceleration, and frequency ratios that define the dynamic components of the experiment, as well as the stress and strain ratios that define the interpretation of the results. The same concept is true for tests done by the other authors listed; however, the reasoning for defining the selected ratios varies. For example, after choosing a length ratio based on geometric constraints and recognizing the need for a modular ratio less than unity, Lu et al. (2012) decided to define the acceleration ratio as something greater than unity to resolve issues with material selection difficulty as well as mitigate noise issues in the data acquisition system at small amplitude ground motion. The authors recognized that this decision implied the acceleration due to gravity was also greater than unity. Since this was not the case, additional weights were distributed throughout the structure to properly simulate vertical loads. It is clear that the force ratio and mass ratio are usually quite small. This makes sense, as there are often weight limitations specific to the shake table facility that must be taken into consideration. The time ratio is also always less than unity in the examples presented, indicating that the input frequency of the earthquake simulation must be increased.

2.3.3 Limitations of Small-Scale Testing

The similitude laws presented previously and used in the shake table tests listed above properly consider similarities between the prototype and the model in the elastic range. This can be seen in the formulation of the similitude laws used. The scaling law for material properties is a ratio of the elastic modulus between model material and prototype material. Clearly, an accurate modular ratio does not guarantee the similarity of material behavior in the plastic strain range. Since high level earthquakes inherently cause lateral forces that induce inelastic effects, it is imperative that the effectiveness of similitude in the plastic strain range be properly examined. It has been proven through both mathematical analysis and physical testing that geometrically similar models can accurately predict the stress and strain behavior of their prototype counterpart into the elastic range when properly constructed (Goodier and Thomson 1944). The proper construction of such a model requires that the stress-strain behavior be similarly scaled at all strain values, thus ensuring a similar hysteretic response of the model and prototype. In order for this to be true, the model material must have similar hardening and/or softening characteristics and an appropriately scaled yield point as compared to the prototype (Murphy 1950). For the model to be a true model, this similarity would

need to be exact for the extent of the strain range of interest. However, similarity requirements can be relaxed and the model material deemed “adequate” if the model is to be acceptably distorted. The use of adequate material models is implicitly seen in the formulation of similitude requirements in the previously identified literature by way of the chosen elastic modular ratio used to define model similarity. It is also explicitly stated in a previously mentioned concrete shake table test (Li et al. 2006). The ability of similitude theory to properly define model parameters is therefore maintained. It is only necessary that the designer analyze the similarity of the entire stress-strain curves of both model and prototype material to decide if the model will adequately produce a scaled energy dissipation response in the strain range of interest.

In the case of this work, the material stress-strain behavior is not as important as the force-displacement behavior. The above discussion is still applicable to the focus of this work, but some modifications must be addressed. Accurate stress-strain behavior is important if one designs a geometrically similar model that is meant to provide accurately scaled stress and strain data at specific points on each member. This is not the case for the current project. A geometrically dissimilar model is acceptable as long as the overall force-displacement behavior of the device is accurate. Force-displacement behavior is related to but does not directly correlate to the material stress-strain relationship. It is therefore possible to fabricate a device from a material with a distorted modular ratio and still obtain the proper behavior of interest. This is seen schematically in Figure 9. Many small-scale tests utilize only the first step in this process. This limits the material chosen to the previously discussed stress-strain laws. The process used in this design utilizes the strengths of the two-step process that frees the designer from the material constraint and leaves only the functionality constraint. This will be further discussed in chapter 3.

2.3.4 BRB Testing

While there is extensive literature on large-scale BRB testing, there is little to no literature on small-scale BRB testing. There has been work done on low-tech devices that are both simpler in design and smaller in size than the average large-scale specimen (Palazzo et al. 2009); however, even this design is much larger than necessary for this project. While there has not been small-scale testing of typical BRB devices, there has been small-scale testing of individual components of a traditional BRB – steel and concrete. “Small-scale” can refer to any device that is not tested at its full structural size. However, the applicability of small-scale testing depends on the material, the magnitude of scaling, and the desired model similarities. There are documented problems in the literature associated with small-scale reinforced concrete testing. While this research does not explore reinforced concrete, there is potential for use of concrete as a restraining mechanism, so the difficulties associated with scalability have been documented. The strength of concrete is associated with crack propagation, which depends on the flaws in the concrete specimen. Since the

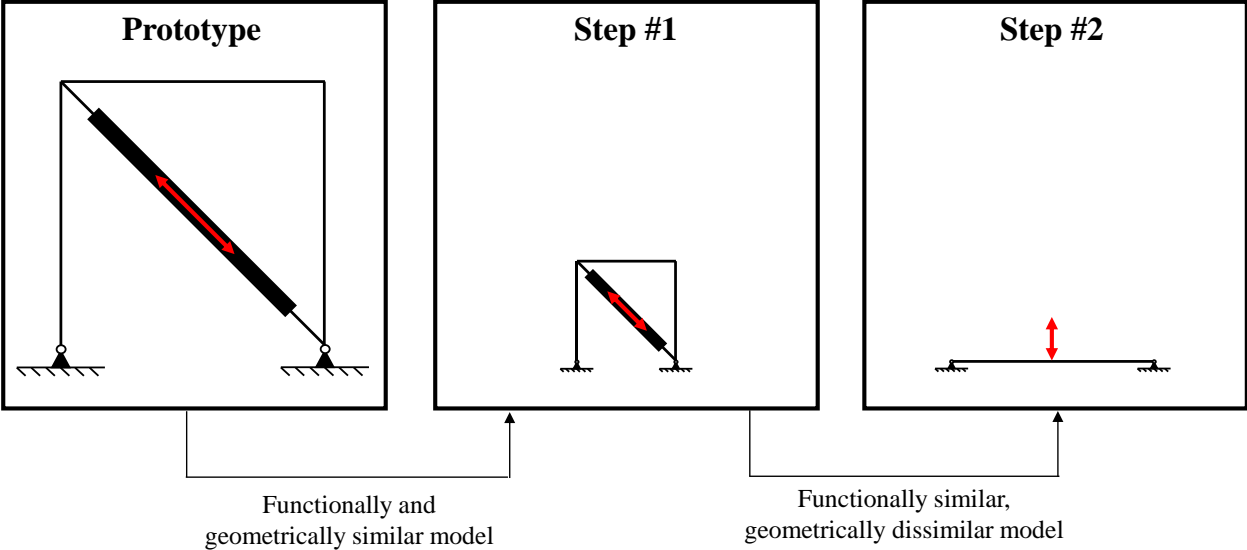


Figure 9. Schematic two-step similitude process for geometrically dissimilar models.

aggregate size of concrete mixtures cannot be scaled down in the same proportion that the size of the member is scaled, the crack propagation is not comparable from small- to large-scale failure. Problems in modeling the interface conditions between cement and aggregate and the variety of factors influencing the concrete mixture strength (i.e. aggregate size, water content) causes small-scale concrete models to show significant overstrength when compared to their large-scale counterparts, with the amount of overstrength increasing as the size of the model decreases (Kim et al. 1988; Knappett et al. 2011; Leicester 1973). While this overstrength is significant, there have also been tests conducted on microconcrete (concrete made from Portland cement, water, and no coarse aggregate) that show the effectiveness of using microconcrete as a small-scale modeling material (Kim et al. 1988). Many tests in the literature use microconcrete for acceptable results. Since the concrete in a BRB is only acting as a restraining mechanism and is not expected to carry a large axial load, overstrength issues are not as much of a concern and the accepted microconcrete mixture could likely be effectively used. However, another important consideration in the design of this component is its manufacturing ease. One of the overall goals of the experimental design is to manufacture parts that are easily replaced after testing or upon failure so that the number of tests completed in a certain time frame can be maximized. The use of a concrete filled steel tube as a restrainer mechanism does not yield itself to this type of quick replacement, as new concrete would have to be cast and cured for each new brace. This type of restrainer mechanism also severely limits the geometry of the brace core. Because the brace yield capacity and elastic stiffness are expected to necessarily be scaled to a very small value, any severe limitation on brace core design presents the likelihood that proper scaled values will not be obtainable. Based on this information, the conventional BRB setup was deemed unacceptable, and focus was redirected to a small-scale all steel BRB device.

Steel is a much easier material to work with when considering issues that may arise with small-scale modeling because it is inherently a more homogeneous material as compared to concrete. Regardless of the materials, the main concern of these development efforts is that the load-deformation behavior of the model accurately simulate the load-deformation behavior of the prototype. A concern for steel that is documented in the literature is the issue of higher than expected strength and lower than expected ductility. This behavior can be attributed to differences in the forming process. Cold formed metals can behave in this way due to internal strain induced during the forming process. While this is an issue, it is usually resolved with a heat treatment process (Kim et al. 1988). There has also been a documented difference in yield strength of steel coupons for samples cut perpendicular to the direction of rolling vs. those cut parallel to the direction of rolling (Jia et al. 2017). However, the difference is small, especially considering the inherent variation in testing and potential for slight material differences throughout a steel sheet. Overall, mild steel has a repeatable load-deformation behavior that can be easily assessed to a reasonable degree of certainty.

Therefore, it is likely that it is possible to design and manufacture a BRB model made of mild steel that both has accurate, predictable behavior and is easy to assemble.

Chapter 3

3 Small-scale BRB Analog

This chapter provides a detailed design overview of the small-scale BRB from the conceptual phase to the physical device design. To begin, the scaling laws necessary for overall project completion are discussed, along with the logical reasoning that led to the adoption of the scaling factors used for the duration of device design. Then, the design concepts used in creating large-scale, all steel BRBs as previously discussed are transferred to the design of a small-scale, all steel BRB device. During the process of designing this device, there were multiple iterative models conceptualized. Two of these models are presented in this chapter: the beam-type design and the ring-type design. Their strengths and weaknesses, as understood at the time of the initial prototyping, are then addressed. Following this, the ring-type design is chosen as the model to proceed into the physical design stage, and the physical component drawings are discussed.

3.1 Scaling from Prototype to Model

Chapter 2 discussed both the properties of full scale BRBs and similitude rules for accurate prototype to model scaling. It also addressed two of the main design goals that led to the decision to focus effort on an all steel geometrically dissimilar small-scale analog. The first of these goals was to design a device that is easily replaced after testing at design level earthquake ground motions. The second goal was to design this device with functional similarity at relatively low force and deformation levels. A concrete restraining mechanism is not as useful for quick replacement as compared to a steel restraining mechanism. A geometrically similar design severely limits the range of functionality of the device. Therefore, this section discusses design decisions made to achieve a geometrically dissimilar but functionally analogous small-scale BRB. The main goal of the model BRB is to dissipate energy in such a way that it achieves a full hysteretic curve characteristic of the prototype BRB. The design method must be accurate and repeatable over a range of sizes so that prototype BRBs of differing core areas can be properly simulated at the scale chosen.

3.1.1 Prototype Geometry & Seismic Weight

Recall that the focus of this thesis is the design of a small-scale BRB, but the overall goal of the work is to design a component that dissipates energy as expected as part of a larger SFERS model. Therefore, the first step in the process of meeting this goal is to evaluate the necessary scaling laws for the project as a whole and relate them to the scaling of the individual BRB. In order to do this, some preliminary features of the

prototype building must be established. A plan view of the building prototype is seen in Figure 10. For the initial evaluation of gravity loads, the frame bays were considered to be 20 ft. x 20 ft. and the story heights were considered to be 13 ft. at all levels with a maximum of six stories. The dead loads and seismic loads were defined with the guidance of ASCE 7-16 and are tabulated in Table 2 (ASCE 2017). The decking at each floor is considered as a composite slab weighing 50 psf, while the roof decking is considered as plain steel weighing 3 psf. The structural framing members are considered as an average of 20 psf over the entire tributary floor area. The 10 psf miscellaneous allowance considers the addition of fireproofing, mechanical & electrical systems, etc. The 42 inch roof parapet and all story walls have the same weight of 25 psf. The seismic weight is calculated as the sum of the dead load and a 10 psf provision for partitions at all story levels. Dividing the seismic load evenly between the two SFRS shown, the total calculated seismic load per typical story is 201 kips. The total calculated roof seismic load is 89 kips. Therefore, the maximum total seismic weight per lateral frame is 1,094 kips.

3.1.2 Project Scaling Laws

Adequate scaling laws must be defined that follow the similitude theory presented in chapter 2 while also meeting the specifications of the shake table at the University of Tennessee. The shake table has dimensions of 1.2 m x 1.2 m (3.9 ft. x 3.9 ft.) and a payload of 1 metric ton (2,200 lbs.). This places constraints on both the model length and model seismic load. It is impractical to scale the gravitational acceleration, so in order to simulate both inertial and gravitational loads, the acceleration ratio is constrained to 1.0. It is acknowledged that some of the small-scale tests in the literature use an acceleration ratio greater than 1.0; however, this effectively increases the necessary seismic mass and is contrary to the goal of meeting the relatively low payload constraint. Because the acceleration ratio is now chosen, there are only two more independent ratios that can be selected. One of these ratios is necessarily the length ratio. This is chosen as 1:12 for the purpose of designing a model that has a bay width less than the dimensions of the shake table but is still large enough to physically manufacture all components and connections. Finally, the force ratio is chosen as 1:700 to ensure the maximum seismic load of a 6-story SFRS model frame is less than 1,600 lbs. This seismic load limit is 600 lbs. less than the maximum payload of the shake table. This ensures that all measurement equipment, additional bracing systems, etc. may be placed on the shake table along with the required seismic mass plates while still remaining at or under the maximum payload of the system. The three chosen scaling ratios and pertinent dependent scaling ratios are shown in Table 3.

Before accepting these scaling ratios, one must evaluate the implications of the calculated ratios and determine if the limitations and/or distortions they present are reasonable. The first distortion recognized is

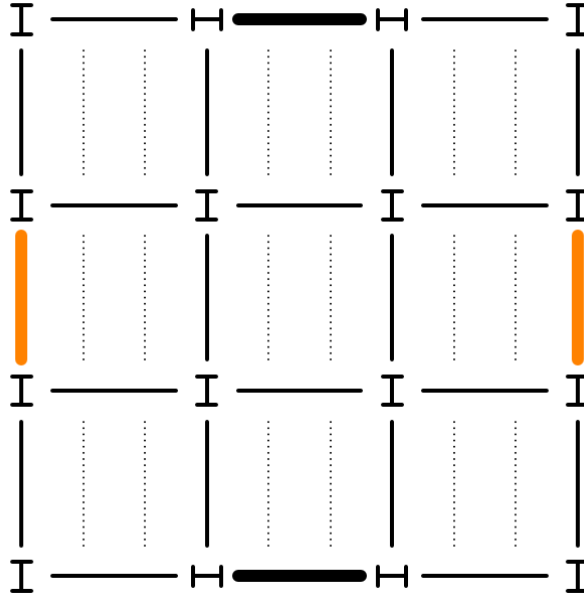


Figure 10. Plan view of prototype building layout with moment frames designed in this study highlighted.

Reproduced from (Talley 2018)

Table 2. Dead loads for the prototype building.

Load Source	Floor (psf)	Roof (psf)
Decking	50	3
Structural Framing	20	20
Miscellaneous	10	10
Wall & Parapet	25	25

Table 3. Project scaling ratios.

Chosen (Independent) Ratios			Calculated (Dependent) Ratios			
Length Ratio	Acceleration Ratio	Force Ratio	Stiffness Ratio	Modular Ratio	Time Ratio	Frequency Ratio
0.0833	1.00	0.00143	0.0171	0.206	0.289	3.46

the stress-strain distortion evidenced in the modular ratio not being equal to 1.0. In order for the stress behavior of the model to properly simulate the prototype, the modulus of elasticity of the model material, as well as the ratio of stress to strain for the entire plastic strain range considered, must be 0.206 times that of the prototype. If steel is considered as the prototype material, this implies the model material must have a modulus of approximately 6,000 ksi and a stress-strain behavior that follows the typical behavior of mild steel (linear-elastic range, yield plateau, strain hardening and strain softening). There is no common material that meets these specifications. However, this does not mean that the model scaling ratios are unacceptable because the goal of the project is not to measure stress and strain but rather to accurately simulate force and displacement. This can be accomplished using the scaling ratios in Table 3 along with the two-step similitude process previously discussed.

The other implication of these scaling ratios is that the frequency of ground motion input must be over three times higher than the earthquake ground motion histories used in numerical analysis of the prototype. The limiting frequency for adequate control of the shake table is 50 Hz. This means the input frequency for the prototype is limited to 14.4 Hz. While this is limiting, it is estimated that the maximum fourth mode frequency will be less than 1.5 Hz for the prototypes considered (Talley 2018). Therefore, the frequency input limit will not limit effects of higher modes of vibration. While the previous discussion established the initial parameters used in this study, it is also acknowledged that the choice of scale factors can be easily changed should future work on the project necessitate such a change.

3.1.3 Prototype Yield Strength & Stiffness

Before the model BRB can be designed, the strength and stiffness of the prototype BRB must be calculated. The nominal yield force of a BRB is calculated using AISC 314-16 (AISC 2016).

$$P_{y_{sc}} = F_{y_{sc}} A_{sc} \quad (3.1)$$

Where:

$P_{y_{sc}}$ = design yield strength of BRB steel core

$F_{y_{sc}}$ = design yield stress of BRB steel core

A_{sc} = cross-sectional area of BRB steel core

The stiffness of a BRB is more complex than a simple truss element due to the varying cross-sectional area of the core, transition region, and connection region. Therefore, an appropriate stiffness modification factor, KF , is applied to the stiffness calculation as follows (Kersting et al. 2016):

$$K = KF \frac{A_{sc} E}{L} \quad (3.2)$$

Where:

KF = stiffness modification factor

A_{SC} = cross-sectional area of BRB steel core

E = Young's modulus of BRB steel core

L = work point-to-work point length of BRB steel core

The minimum design yield stress is 38 ksi and Young's modulus for steel is 29,000 ksi. The work point-to-work point length is dependent upon the structural layout of the larger building model and the chosen brace pattern of the buckling restrained brace. Using a chevron bracing pattern and the previously given building layout, the length of the prototype BRB is 16.4 ft. The area of the steel core is dependent upon detailed prototype design that is not yet complete at this time. However, based on previous work (Simpson and Mahin 2018b; Talley 2018) and preliminary calculations by Peter Talley, an appropriate range of cross-sectional areas is identified as 3.0 – 9.0 in². KF is also unknown but is estimated as 1.5, which is the median value of the acceptable range given in (Kersting et al. 2016).

Equations (3.1) and (3.2) are used to calculate the design yield force and stiffness of the prototype BRB. These values are then multiplied by the force and stiffness scaling factors, respectively, to determine the small-scale model yield force and elastic stiffness. These values are shown in Table 4 for three BRB core area sizes that define the range of interest: 3.0 in², 6.0 in², and 9.0 in².

A previously identified problem was that of achieving the desired yield strength and elastic stiffness using the determined force and stiffness ratios while still manufacturing the model out of a common material with an adequately ductile behavior. This is not physically realistic using the same geometry as the prototype BRB. If a simple axially loaded steel bar was to be used to reproduce the hysteretic behavior of the steel prototype BRB, the required area ranges between 0.004 in² – 0.013 in². If a different material is used, the material properties must be very specific to satisfy the chosen scaling constraints. This is illustrated by analyzing the yield displacement, which is simply the yield force divided by the elastic stiffness. Using equations (3.1) and (3.2), the yield displacement is written as:

$$\delta_y = \left[\frac{F_y}{E} \right] \left[\frac{L}{KF} \right] \quad (3.3)$$

The yield displacement and the brace length both have units of [L], which is multiplied by the length ratio to determine the appropriate value for the model. In order for both the yield displacement and the brace length to equal their appropriate scaled values in the model, the ratio of material yield strength to Young's modulus must remain constant. So, not only is the required area of the model brace core unrealistically

Table 4. Yield force and elastic stiffness values for prototype and model BRBs.

Prototype Values			Model Values	
A_{sc} (in. ²)	P_{ysc} (kips)	K (kips / in.)	$P_{y,m}$ (lbs.)	K_m (lbs. / in.)
3.00	114	663	163	11,367
6.00	228	1,326	326	22,734
9.00	342	1,989	489	34,100

small, but the material properties must be scaled to exactly match behavior of the prototype material in order for the model to function properly. This is not a practical solution.

3.2 Functionally Similar, Geometrically Dissimilar Model

Since it is not practical to design a similarly shaped BRB analog due to the model scaling ratios required, a different solution needed to be employed. Inspiration was drawn from the several all steel prototype BRBs presented in chapter 2. Most notably, the idea of energy dissipation through plate bending (Gray et al. 2012, 2017) was used to design an appropriate small-scale BRB analog. The guiding principle behind this design is that the stress and strain at particular points within the small-scale BRB are not important. Rather, the force-displacement curve of the device as a whole is the main item of interest. Therefore, a device of a different shape with different derived equations that define yield force and elastic stiffness can produce the desired behavior with fewer constraints on material properties and part geometry. This is the core concept of the two-step scaling process previously presented in Figure 9.

3.2.1 Initial Model

Using the same predictive modeling technique found in Gray et al., the first prototype design was based on a simple fixed beam with a central concentrated load, as shown below in Figure 11. Assuming an elastic perfectly-plastic stress-strain relationship and a rectangular cross-section, the plastic bending moment of a section is found using the following formula:

$$M_p = \frac{F_y db^2}{4} \quad (3.4)$$

Where:

M_p = plastic bending moment of the section

F_y = yield stress of the material

b = depth of the cross-section

d = thickness of the part

Assuming a constant value of Young's modulus and constant beam cross-sectional geometry, the maximum bending moment at the center of the beam in the model shown in Figure 11 is:

$$M = \frac{PL}{8} \quad (3.5)$$

Where:

P = magnitude of the concentrated load

L = length of the beam

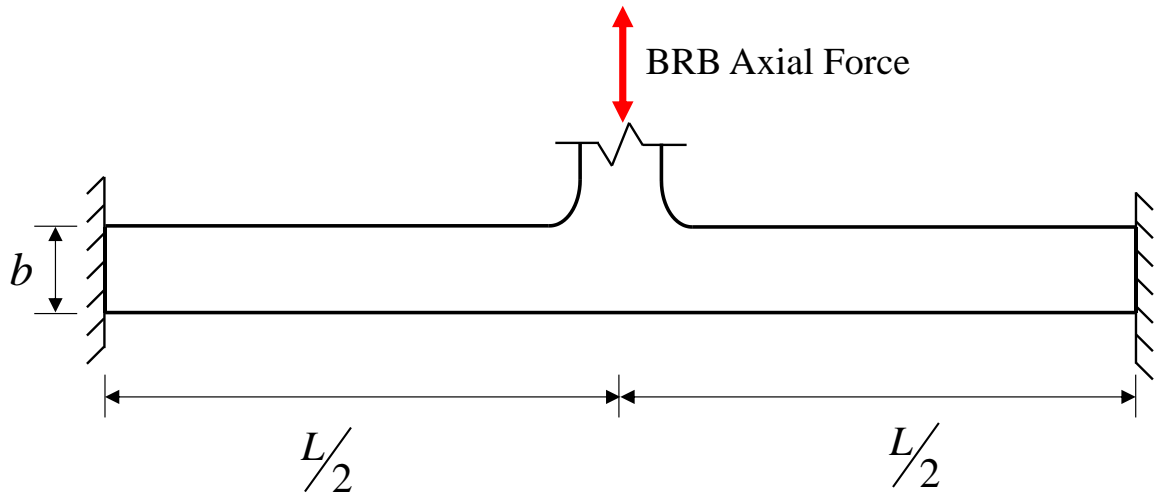


Figure 11. Beam bending model.

The maximum beam deflection at the beam center is:

$$\delta = \frac{PL^3}{192EI} \quad (3.6)$$

Substituting the moment of inertia into equation (3.6), the maximum beam deflection is:

$$\delta = \frac{PL^3}{16bd^3} \quad (3.7)$$

In order to form the predictive equation for the yield strength of the bending beam, the plastic moment from equation (3.4) is set equal to the maximum bending moment in equation (3.5) and solved for the magnitude of the concentrated force required to yield the beam in bending. Equation (3.7) is simply rearranged to represent the bending stiffness of the beam. These two representative equations are presented below, with all variables having the same definitions as previous.

$$P_y = \frac{2F_y db^2}{L} \quad (3.8)$$

$$K = \frac{16Edb^3}{L^3} \quad (3.9)$$

The predictive equations have four variables that can be changed to yield different results. Yield stress (F_y) and Young's modulus (E) are material dependent, and therefore considered as one variable. The beam length (L), beam section depth (b), and part thickness (d) are the other three variables. Since there are only two equations, it then follows that two of the four variables are chosen by the designer (independent variables), and the other two are then solved for using the above equations (dependent variables). Out of necessity, one of the chosen independent variables is the material, as it is impractical to solve for material properties based on geometry and attempt to match a certain material to these values. The other independent variable is the part thickness, as most metals are manufactured in standard sheet thicknesses. Therefore, equations (3.8) and (3.9) can now be rearranged to determine the necessary values for the two dependent variables – length and section depth. The closed-form solution is seen below:

$$b = \left(\frac{P_y}{F_y} \right)^{\frac{1}{3}} \sqrt[3]{ \left(\frac{2}{d^2} \right) \left(\frac{E}{K} \right) } \quad (3.10)$$

$$L = \left(\frac{P_y}{F_y} \right)^{\frac{1}{3}} \sqrt[3]{ \left(\frac{32}{d} \right) \left(\frac{E}{K} \right)^2 } \quad (3.11)$$

From these equations, three conclusions about the relationship of beam length and depth to the independent variables are drawn:

- 1 The ratio of BRB yield force to material yield stress impacts both dependent variables to the same degree.
- 2 Both are dependent on the ratio of Young's modulus to BRB stiffness. However, any change in this ratio impacts the length calculation to a greater degree.
- 3 Both are dependent on the reciprocal of part thickness. However, any change in this design value impacts section depth to a greater degree.

Two choices for material type were explored – aluminum and mild steel. For both materials, a yield stress of 40 ksi was used in calculations. Young's modulus was set to 10,000 ksi and 29,000 ksi for aluminum and steel, respectively. The calculated values for necessary beam length and section depth are shown in Table 5. Since both materials have the same yield stress, the difference in geometry due to increased elastic modulus is clearly seen. Steel is the material with the higher elastic modulus and also has higher required beam length and section depth. The impact of part thickness is also seen. For both materials, the thinner part has a higher required beam length and section depth.

3.2.2 Fabrication Error Considerations

The relationship between material type and thickness to model geometry informs decisions on the part fabrication, but the accepted tolerance of the manufacturing process also influences design. The parts are to be cut using a waterjet machine, and this machine has a previously observed tolerance of +/- 0.015 inches. Therefore, there is potential for inaccurate cutting of the yielding plate parts that will introduce error into the yield force and stiffness of the physical specimen. This is an absolute error, so it is desirable that the section depth be larger to decrease the percent error caused by manufacturing tolerances. For example, a prototype BRB with a core area of 3 in² requires a beam depth of 0.197 inches if it is made of 0.125-inch-thick aluminum. If the same part is made of 0.125-inch-thick steel, it requires a beam depth of 0.280 inches. In the event of the part being cut at the maximum negative tolerance, the depth of the aluminum part would be 0.182 inches, and the depth of the steel part would be 0.265 inches. For the aluminum part, this translates to a percent error in yield force of 14.6% and a percent error in stiffness of 21.1%, based on the current closed-form solution. For the steel part, the percent error is reduced to 10.4% and 15.2% for yield force and stiffness, respectively. This shows that the percent error decreases as the overall width of the part increases. So, while it is still undesirable to have this much error due to manufacturing, it is best to increase the geometric dimensions of the part in order to decrease the potential percent error. Using this information, as well as the previously discussed relationships, 0.125-inch-thick steel is the preferable material. Figure 12 shows the schematic design of the entire yielding plate. As the beam length increases, the overall dimensions of the part increase in the direction perpendicular to loading. This is problematic because the

Table 5. Initial model BRB geometry.

A_{sc} (in. ²)	$P_{y,m}$ (lbs.)	K_m (lb. / in)	0.125" Aluminum		0.250" Aluminum		0.125" Mild Steel		0.250" Mild Steel	
			b (in.)	L (in.)	b (in.)	L (in.)	b (in.)	L (in.)	b (in.)	L (in.)
3.00	163	11,367	0.197	2.374	0.124	1.884	0.280	4.827	0.177	3.831
6.00	326	22,734	0.312	2.991	0.197	2.374	0.445	6.082	0.280	4.827
9.00	489	34,100	0.409	3.423	0.258	2.717	0.583	6.962	0.367	5.525

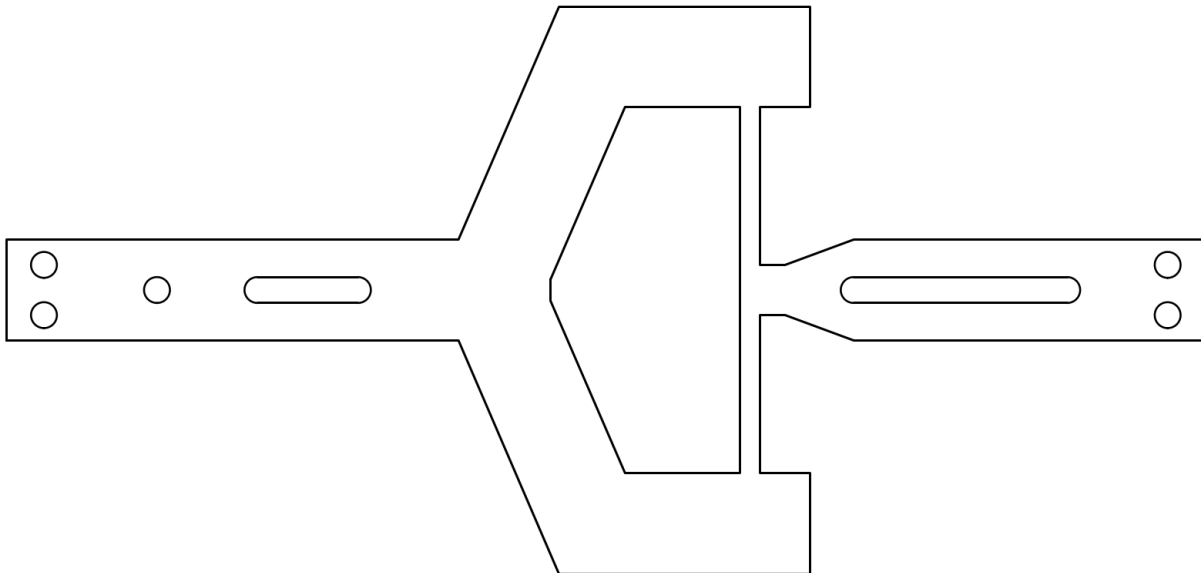


Figure 12. Schematic of yielding plate design using the beam model.

0.125-inch-thick steel produces the longest necessary beam lengths. When considering higher force BRB analogs this longer beam length may cause the BRB to not fit well in the frame bay. Therefore, a different part geometry needed to be considered. This led to the next iteration of this device – the ring-type yielding plate BRB.

3.2.3 Second Iteration Model

The main requirement of the model BRB is that it produces the desired hysteresis. The shape of the BRB yielding plate is not as limited as is the axial force-displacement behavior it produces. Therefore, the second iteration of the model design used a different shape for the yielding section. Instead of simple beam bending, a circular yielding mechanism was explored. The simplified conceptual model is shown in Figure 13. The same procedure as previously described for the bending beam was followed for the circular yielding mechanism in order to determine an initial estimate of geometric constraints.

The formula for the maximum moment and the vertical displacement due to a concentrated load on a thin ring are seen below (Engineering Library 2021).

$$M = 0.3183PR \quad (3.12)$$

$$\delta = 0.149 \frac{PR^3}{EI} \quad (3.13)$$

Where:

M = moment at the point of load application

P = magnitude of concentrated load

R = average ring radius

δ = vertical displacement of the ring due to the concentrated load

E = Young's modulus

$$I = \frac{db^3}{12}$$

d = thickness of the yielding plate

b = width of the ring

Setting equation (3.12) equal to equation (3.4) and solving for P, an equation for yielding force is determined.

$$P = \frac{F_y db^2}{1.2728R} \quad (3.14)$$

Rearranging equation (3.13) and substituting in the moment of inertia, the equation for stiffness is determined.

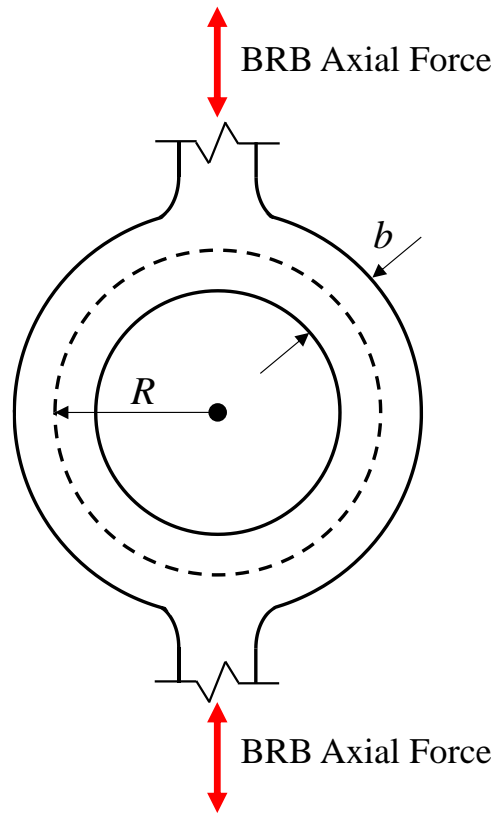


Figure 13. Circular bending model

$$K = \frac{Edb^3}{1.788R^3} \quad (3.15)$$

As was done for the initial model, equations (3.14) and (3.15) can be solved simultaneously to determine the appropriate ring thickness and average ring radius for different prototype BRB core areas.

$$b = \left(\frac{P_y}{F_y} \right) \sqrt[3]{ \left(\frac{1.153}{d^2} \right) \left(\frac{E}{K} \right) } \quad (3.16)$$

$$R = \left(\frac{P_y}{F_y} \right) \sqrt[3]{ \left(\frac{0.645}{d} \right) \left(\frac{E}{K} \right)^2 } \quad (3.17)$$

It is clear from these equations that, using the simplified model, the required width of the beam and the ring are comparable. However, the average radius is only about a quarter of the required beam length, which means the circular model has only half the width of the beam model. This is a considerable improvement in being able to fit the model BRB in the building frame bay. See Table 6 for a numeric comparison of required geometric values for 0.125-inch-thick steel plate.

3.2.4 Limitations of the Predictive Equations

While the predictive equations in the previous section yield promising results, there is introduced error due to the simplified modeling technique that limits the usefulness of these results. The first simplification made was to assume the load was a concentrated force rather than a distributed load. Assuming a concentrated load increases the maximum moment in the ring, which increases the calculated ring width. The equations for maximum moment and vertical deformation are also for “thin” rings, in which the ring width is much smaller than the ring radius. That is not the case for the model BRB. Therefore, the thickness of the ring is not negligible in the formulation of the moment and deformation equations. Because of these two major simplifications, this model is expected to produce results with a level of accuracy that is less than desired. However, these values for thickness and radius form a good basis for initial BRB geometry when iteratively refining the small-scale BRB using numerical modeling software.

3.3 Physical Design of the Circular BRB

Up until this point, the design of the functionally similar model BRB has been based completely on the assumed elastic response. However, as mentioned, it is likely that the equations defining moment in a thin ring are not an accurate prediction of the behavior of the BRB central ring design due to the relatively large thickness in comparison to the ring radius. Also, this simplified model provides no information on the functionality of the device in the inelastic range. Therefore, three main steps are necessary:

Table 6. Comparison of parameters for 1st and 2nd model iteration.

A_{sc} (in²)	P_{y,m} (lbs)	K_m (lb / in)	Beam		Circular	
			b (in)	L (in)	b (in)	R (in)
3.00	163	11,367	0.280	4.827	0.233	1.314
6.00	326	22,734	0.445	6.082	0.370	1.655
9.00	489	34,100	0.583	6.962	0.485	1.895

- Design a physical device that incorporates ring bending to dissipate energy.
- Numerically model the device in finite element software to better predict both elastic and inelastic behavior.
- Manufacture the physical device and experimentally test its behavior to evaluate the accuracy of the numeric simulation.

These goals are necessarily intertwined. In order to clearly convey the findings of this work, the physical model will first be presented without reference to numeric simulation of its functionality. Then, the finite element analysis process will be presented in the context of its relation to the physical part. Next, the experimental evaluation of the device will be discussed. Finally, necessary model updating will be presented and further improvements will be discussed.

3.3.1 Yielding Plate Design

The theoretical design of this device was based on energy dissipation through plate bending. The yielding force and elastic stiffness of this energy dissipator must be predictable and controllable. Therefore, the first consideration in the design process is the fabrication of the main energy dissipation mechanism – the yielding plate. The central portion of this yielding plate is to be circular, and the load is to be transferred axially through the center of the circle. All portions of the plate outside the central ring are to remain elastic. This concentrates plasticity in the specially shaped ring, giving the designer more control over the total load-deformation behavior. See Figure 14 for the schematic of the physical model of the yielding plate. Notice the three dimensions labeled as “A”, “B”, and “C”. Dimension “A” and “B” define the inner and outer diameter of the central ring. These are the two dimensions that control the yielding force and elastic stiffness of the device. Dimension “C” adjusts to accommodate smaller or larger ring diameters while still maintaining the same overall length. The plate is designed to have a thickness of 0.125 inches, as discussed in earlier sections.

3.3.2 Assembled Test Mechanism

Figure 15 shows the assembled mechanism with the yielding plate highlighted in orange. A full set of drawings is in Appendix A. The first important component of the BRB mechanism is the confining plate. There are two confining plates attached to the yielding plate – one on either side – to prevent out-of-plane buckling during axial compression. The slotted holes in the yielding plate accommodate the connection of these confining plates along the yielding plate length while also allowing free relative movement between the yielding plate and the confining plates. While friction may still influence the load carried by the yielding plate, the free relative movement between components encourages most of the axial load to be carried solely by the yielding plate. This mimics the design of full-scale BRBs by uncoupling the restraining mechanism

and the brace core. The screws inserted through the slotted connections provide resistance against in-plane buckling of the yielding plate. The yielding plate is then connected to a thicker grip plate through a series of fillers and splice plates. This grip was designed at a thickness of 0.375 inches to fall within the thickness range of the machine grips to be used during testing. The last important part of the design involved accounting for the expected relative axial movement between the yielding plate and other components of the BRB. The test protocol, which will be discussed more in depth in chapter 5, had a prescribed maximum displacement of 0.26 inches in both tension and compression. Both slotted holes were designed to have at least 0.50 inches of free space on either side of the connecting screw, and the space between the confining plates and the end connection on one side was designed to be 0.50 inches. This ensured there was adequate free space for the yielding plate to displace. It is also required that an LVDT be attached during testing. This will also be addressed later in chapter 5.

Chapter 4

4 Numerical Modeling

In order to gain a comprehensive understanding of the behavior of the physical mechanism at varying axial loads, it is necessary to fabricate several sizes of the yielding plate. Recall from previous discussion that the closed form solutions for yield force and elastic stiffness are not considered reliable for exact calculation due to the necessary simplifications made to obtain them. Therefore, exact sizing of the yielding plate is done using finite element (FE) analysis in a software called ABAQUS. Prior to sizing the physical specimen, the physical design needed to be adequately transferred to the numerical design space by properly applying boundary conditions, using an appropriate material model, and performing a mesh refinement study to validate the accuracy of the given results. After this was completed, the yielding plate was modeled in ABAQUS, displacement-controlled deformation was applied, the resulting force-displacement curve was obtained, and the resulting yield force and elastic stiffness was then compared to the predicted values. The ring radius and thickness were then modified based on the difference between the ABAQUS result and the predicted value, and the process was repeated until ABAQUS calculated results that were close enough to the desired values to justify a physical test of the mechanism. This initial modeling process is later reviewed and revised after initial experimental test results were available; however, this chapter only includes the initial FE modeling steps taken to obtain the first experimental results.

4.1 Initial Finite Element Model

4.1.1 Idealization of ABAQUS Boundary Conditions

While FE analysis is more refined than the initial analytical model, there are still choices made to simplify the modeling process and complexity of calculations so that the numeric simulation was both effective and efficient. First, because the yielding plate is very thin and under only axial load, the stress in the direction normal to the plate surface will be at or close to zero. Therefore, the part was simplified from a three-dimensional plate to a two-dimensional, plane stress plate. There are also many connecting parts in the physical BRB. However, defining frictional forces and contact surfaces for all pieces of the BRB is complex and does not add much value to the final result. It is actually likely that complete modeling could decrease accuracy if any portions of the part were incorrectly input into ABAQUS. So, the second simplification was to remove all parts from the FE analysis except the central yielding plate and to replace these missing pieces with boundary conditions. But, even these boundary conditions were too complex and were again

simplified. Instead of applying boundary conditions to the yielding plate at the holes, a pinned boundary condition was applied at the left edge of the plate. Vertical rollers were applied at discrete points along the slotted holes to prevent in-plane vertical displacement. The right edge of the part was then given a specified horizontal displacement pattern. Any frictional interaction between the yielding plate and confining plates was ignored. See Figure 16 for a visual representation of the two-dimensional part and associated boundary conditions. Note that divisions shown are not elements, but rather are boundaries created for part meshing.

4.1.2 Material Model for Initial Results

At this phase of the project, material had not yet been ordered for yielding plate fabrication. This meant that actual tensile test data was unavailable for material calibration. To overcome this difficulty, tensile test data was obtained from a different test of 3/16-inch thick mild steel (Tanamal et al. 2009). While this material data is not expected to exactly match the actual steel used, it should have a similar elastic modulus and yield strength, which are the main parameters that influence the yield force and elastic stiffness. The material data used was provided as nominal stress and strain data points. This is the usual presentation of such data, however, ABAQUS expects tabular input of true plastic strain and true stress for calibration of material hardening. The process to transform the given data to the expected ABAQUS input is documented below and considered valid until necking (Dassault Systèmes Simulia Corp. 2010).

- Transform the nominal stress, ϵ_{nom} , to true stress, ϵ , using the equation $\epsilon = \ln(1 + \epsilon_{nom})$
- Transform the nominal stress, σ_{nom} , to the true stress, σ , using the equation $\sigma = \sigma_{nom}(1 + \epsilon_{nom})$
- Using these transformed values, find the true plastic strain, ϵ^{pl} , using the equation $\epsilon^{pl} = \epsilon - \sigma/E$
- Identify key points on the σ vs. ϵ^{pl} curve that well represent the material model. These are the tabulated values that will be input into ABAQUS.

Using this process, the initial material data was transformed to the proper format and used for initial FE analysis. The true stress vs. true plastic strain curve is seen in Figure 17. The initial point on this graph is the yield point. The elastic portion of the stress-strain curve is defined in a different ABAQUS module using Young's modulus. For initial results, isotropic hardening with tabular input was used for the plasticity model. This provides sufficient data for determination of an elastic stiffness and yield strength since these parameters are not dependent upon cyclic testing results.

4.1.3 Element Type Selection

There are strengths and weaknesses of each element type in ABAQUS. It is important to choose an efficient element, but one must be careful to ensure there are no large errors introduced into the model results due to element selection. Initially, a linear, plane-stress quadrilateral with neither reduced integration nor

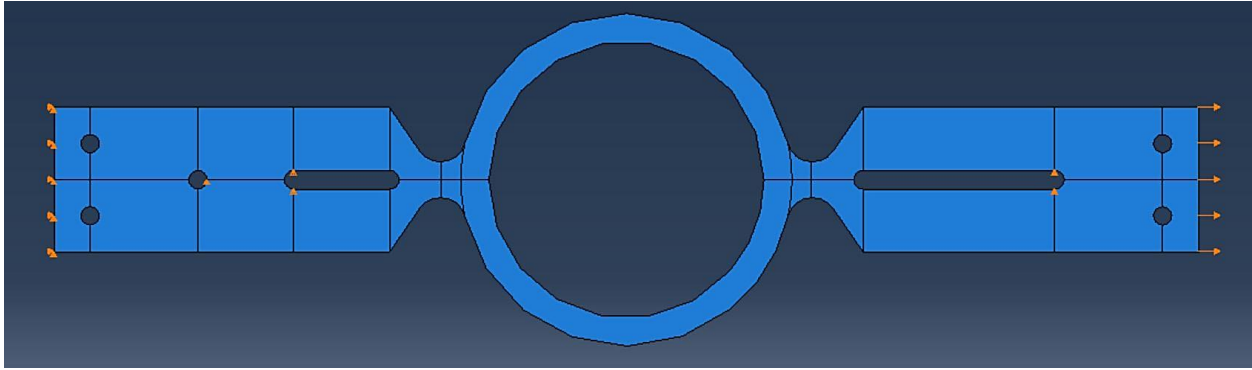


Figure 16. Two-dimensional ABAQUS model of yielding plate.

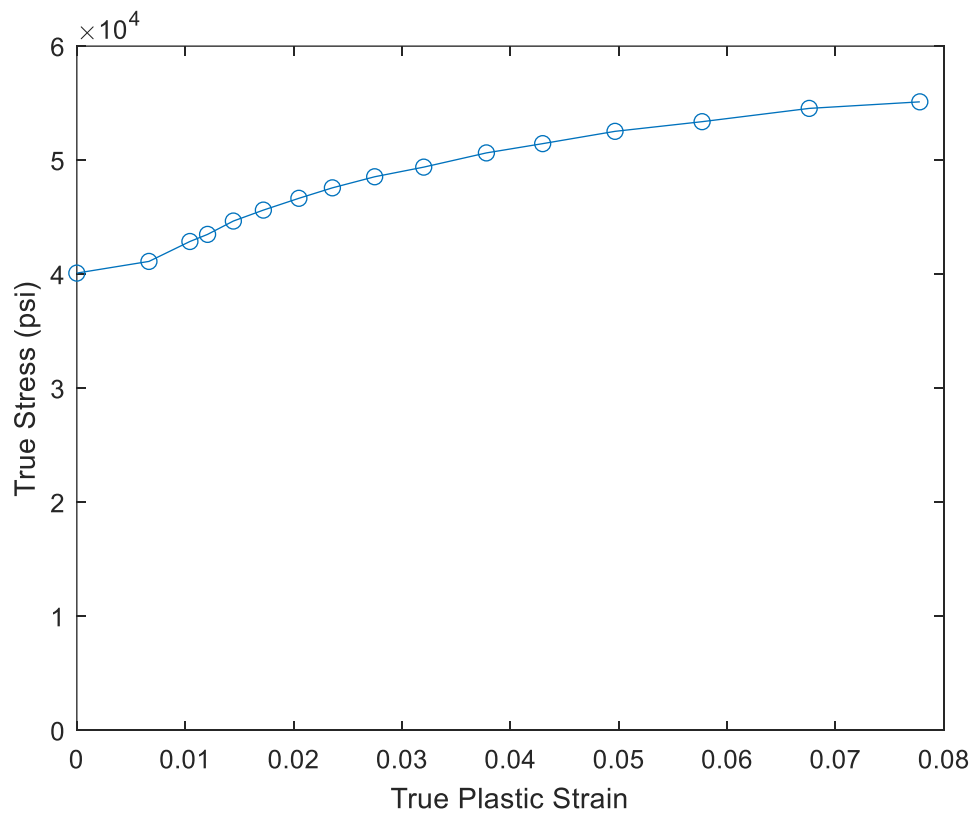


Figure 17. True stress vs. true plastic strain curve for ABAQUS input

incompatible modes (CPS4) was chosen. This element seemed to work, but it provided seemingly unreliable maximum stresses for some elements. As shown in Figure 17, the material used in the initial design phase was a mild steel with an ultimate stress of approximately 55,000 psi. Using CPS4 elements, the averaged stress in some locations was higher than the given ultimate stress of the material. In order to determine the problem, one must know what the FE analysis is doing. FE software solves for the different parameters, which are in this case stress and strain, at discretized nodes along an element. The values of these parameters at each node are then used to interpolate the value of such data at any point on the part. After confirming the stresses at all nodes were at or less than the ultimate stress, it was theorized that the interpolation mechanism of the program caused ABAQUS to interpolate elemental stresses higher than those at the actual element nodes, therefore providing strange results. This was further validated by confirming the maximum strains were much less than fracture strain.

While this reasoning provided circumstantial evidence that the original element type could be justified, other element types were still explored. One such element type was the linear, plane stress quadrilateral with reduced integration (CPS4R). The premise of reduced integration is that the element is evaluated at a reduced number of points rather than all integration points. This “unlocks” the element, reducing the amount of parasitic strain and shear developed during the solution process. One problem with this element type is the potential for “zero-strain” deformation modes, but commercial software implements stabilization techniques to counteract this. This method calculates the value of interest as only one integration point per element (located in the element center) as opposed to four integration points per element (one at each corner) for the linear quadrilateral element. When unaveraged, this meant that each finite element had a single stress associated with it, and the maximum stress calculated during the simulation was at or equal to the ultimate stress of the material. The reduced integration process also simplified the analysis, making it run quicker without sacrificing the overall accuracy of the results. Therefore, this was the chosen element used in all FE analyses.

4.1.4 Mesh Refinement Study

After determining the element type to be used, the next step was to perform a mesh refinement analysis to increase confidence in the accuracy of the results. The circular portion of the yielding plate is where the majority of stress and strain is concentrated. Therefore, this is the portion of the model that requires the most refinement. Since the ring is expected to undergo bending, it is known that one element across the width of the ring is unstable, thus the refinement analysis began with two elements across the ring thickness. The parameters under investigation in this study were: initial stiffness, yield displacement, yield force, and post-yield stiffness.

First, an FE analysis was completed for a yielding plate with 2 elements across the ring thickness. Then, successive analyses were completed for the same yielding plate geometry and one more element than previous across the ring thickness until 20 elements were reached. After all analyses were complete, the initial stiffness, yield force, yield displacement, and post-yield stiffness were calculated for each. Figure 18 shows how these values were determined. The slope of the labeled lines are the elastic stiffness and post-yield stiffness. The post-yield stiffness was an average slope of the curve after yield. It is acknowledged that the accuracy of these parameters is only as valid as the method used to determine them, and that the method itself has limitations. However, if the methodology is consistent for the duration of the mesh refinement study, the integrity of the conclusion is maintained. Finally, the percent difference between successive calculated values was determined.

These final results are tabulated in Table 7 and plotted in Figure 19. The mesh is considered adequate once the percent difference reaches a value of 1.0% or less. Initial stiffness, yield displacement, and yield force each reach and maintain adequacy at 7 elements. The post-yield stiffness, however, oscillates back and forth between a median value for a time before reaching the desired accuracy at 14 elements. It is desirable to have a smaller number of elements across the ring thickness because this will increase the speed of each analysis. Since the main parameters of interest are the elastic stiffness and yield force, the oscillation in post-yield stiffness is considered secondary, and either 7 or 8 elements is deemed sufficient for accurate prediction of yielding plate parameters. When considering either an even number or odd number of elements, the integration scheme of the analysis must be considered. Odd numbered elements have an element directly in the center of the bending portion of the ring, and therefore on the neutral axis. Since there is only one integration point at the center of the element, this element experiences a strain at or near zero. It is undesirable to have the possibility of such an element, so the final conclusion drawn is that using 8 elements across the thickness of the ring is preferred.

4.2 Sizing the Initial Physical Specimens

Now that the FE model has been established, the initial physical specimens needed to be sized for testing. At this stage in the project, stress-strain data was still unavailable for the actual yielding plate material, so it was accepted that the actual yield force and elastic stiffness of the manufactured specimens would be different than the predicted values using the sample stress-strain data detailed above. However, at this time, it is not vital that the BRB conform to any specific strength or stiffness values. Rather, it is important that the overall behavior of the BRB is similar to the goal behavior of the final specimen design. It was assumed that initial rough estimates of sizing would provide an adequate starting point for physical testing. After the

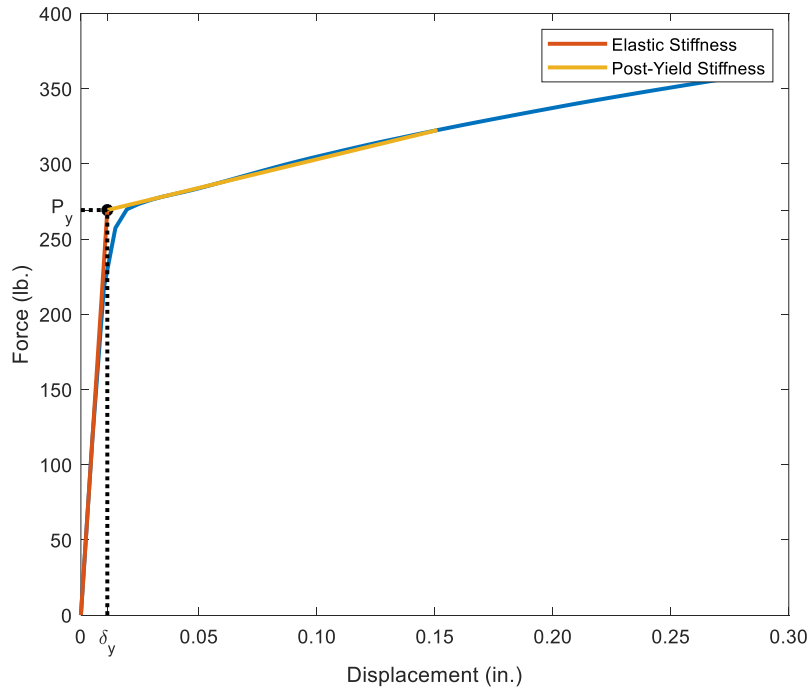


Figure 18. Calculation of parameters for mesh refinement study.

Table 7. Mesh Refinement Analysis - Calculated Parameters

Number of Elements	Initial Stiffness (lb/in)	Percent Difference	Post-yield Stiffness (lb/in)	Percent Difference	Yield Displacement (in)	Percent Difference	Yield Force (lb)	Percent Difference
2	19,351	-	350	-	0.0132	-	256.2	-
3	21,790	12.6%	356	1.9%	0.0113	-14.9%	245.7	-4.1%
4	22,086	1.4%	351	-1.5%	0.0120	6.6%	265.5	8.1%
5	22,081	0.0%	371	5.8%	0.0119	-0.6%	263.8	-0.6%
6	22,142	0.3%	355	-4.5%	0.0121	1.6%	268.6	1.8%
7	22,235	0.4%	377	6.3%	0.0121	-0.5%	268.5	-0.1%
8	22,320	0.4%	359	-4.6%	0.0121	0.2%	270.0	0.6%
9	22,335	0.1%	380	5.8%	0.0121	-0.2%	269.6	-0.2%
10	22,328	0.0%	363	-4.4%	0.0121	0.4%	270.7	0.4%
11	22,341	0.1%	378	4.1%	0.0121	-0.3%	270.1	-0.2%
12	22,356	0.1%	368	-2.8%	0.0121	0.3%	271.1	0.3%
13	22,379	0.1%	376	2.1%	0.0121	-0.3%	270.6	-0.2%
14	22,388	0.0%	372	-0.9%	0.0121	0.1%	271.0	0.2%
15	22,377	-0.1%	374	0.6%	0.0121	0.0%	270.9	-0.1%
16	22,376	0.0%	375	0.2%	0.0121	0.1%	271.1	0.1%
17	22,382	0.0%	374	-0.2%	0.0121	0.0%	271.1	0.0%
18	22,392	0.0%	376	0.3%	0.0121	0.0%	271.2	0.0%
19	22,397	0.0%	375	-0.1%	0.0121	0.0%	271.1	0.0%
20	22,397	0.0%	375	-0.1%	0.0121	0.1%	271.3	0.1%

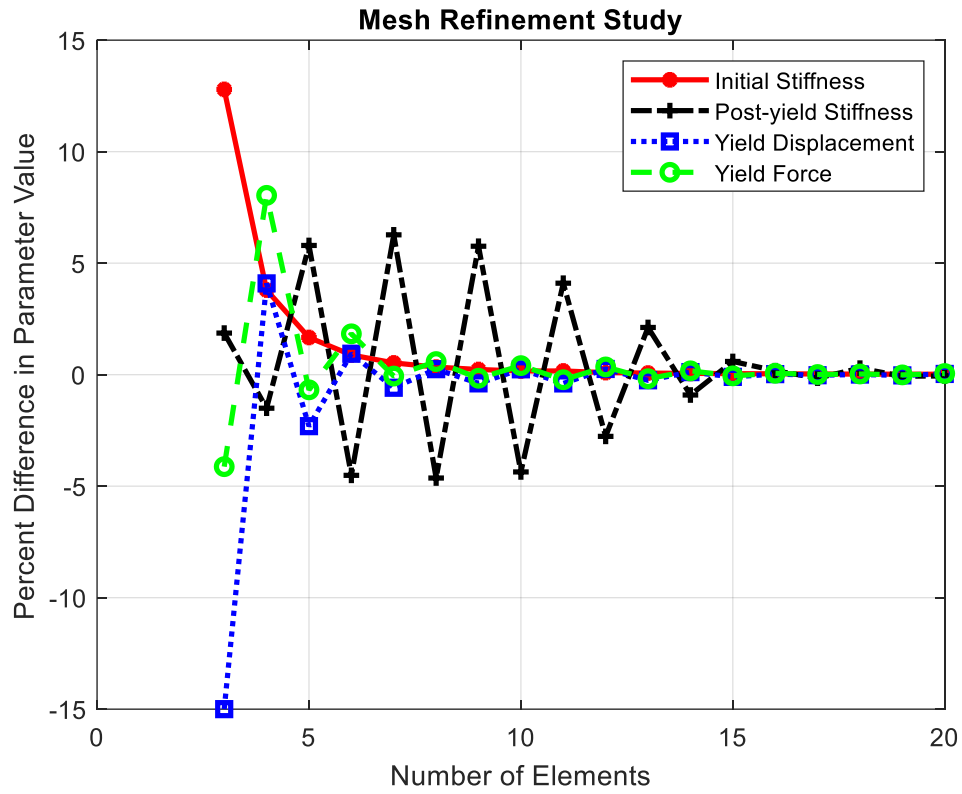


Figure 19. Graphical Representation of Mesh Refinement Study

initial physical tests were complete, the FE model was refined to better describe the mechanism behavior. This is discussed in detail in chapter 6. The initial predictive equations are known to have inherent inaccuracy due to simplifications made in the model when forming them. They are useful for providing a rough estimate of the required dimensions of this device as starting values from which the part can be further refined. As previously explained, it was desired to test three sizes of BRBs in initial testing – one each that corresponded to a 3.0 in² prototype core area, a 6.0 in² prototype core area, and a 9.0 in² prototype core area. From now on, these three sizes will be referred to as “small”, “medium”, and “large”, respectively. Using equations (3.16) and (3.17), Table 8 shows the starting values for average radius, R , and ring width, b , for each considered size of BRB. Using this geometry for a 0.125-inch-thick steel plate and the ABAQUS model previously described, Table 9 shows the calculated yield force, elastic stiffness, and yield displacement of each considered BRB, along with the percent difference between the expected result and the calculated FE result for each parameter.

It is obvious that the initial predictive equations are not as accurate as necessary for estimating geometry of the model BRB. The most likely reason for the large error is that the equations used were for rings which had such a large radius as compared to their thickness that deflection theory for straight beams could be applied (Engineering Library 2021). This is not the case, so the error in actual vs. goal values is quite high. Although the error was high, there were no alternative predictive equations, so an iterative process was used to determine the geometry of initial test specimens. The “goal” values were either raised or lowered, depending on if the calculated error was positive or negative, geometry was recalculated, and the ABAQUS analysis was re-run. This iterative process was able to produce geometries that came close to the “goal” values for yield force and elastic stiffness for each of the three BRB sizes. The final iterative ring width and average radius for each specimen were then used in the plan set for initial manufacturing. The final average ring radius, ring width, estimated yield force, estimated elastic stiffness, and estimated yield displacement are shown in Table 10.

Table 8. Width and radius of circular-type BRBs using initial predictive equations.

A_{sc} (in ²)	$P_{y,m}$ (lbs)	K_m (lb / in)	b (in)	R (in)
3.00	163	11,367	0.233	1.314
6.00	326	22,734	0.370	1.655
9.00	489	34,100	0.485	1.895

Table 9. Percent error in parameters of interest using initial predictive equations.

A_{sc} (in ²)	$P_{y,m}$ (lbs)	PE _P	K_m (lb / in)	PE _K	δ_y (in)	PE _{δ}
3.00	272	66.9%	14,097	24.0%	0.0193	35.0%
6.00	505	54.9%	23,767	4.35%	0.0212	48.3%
9.00	753	54.0%	34,019	-0.24%	0.0221	54.5%

Table 10. Geometry and predicted values for final experimental specimens to 3 significant figures.

A_{sc} (in ²)	R (in)	b (in)	$P_{y,m}$ (lbs.)	K_m (lb. / in)	δ_y (in)
3.00	0.908	0.144	132	8,450	0.0156
6.00	1.050	0.230	269	22,300	0.0121
9.00	1.129	0.297	398	33,000	0.0121

Chapter 5

5 Experimental Tests

There were three distinct phases of the initial experimental testing. First, monotonic tension tests were carried out on steel coupons to characterize the specific material properties of the mild steel being used. Next, quasi-static cyclic tests were conducted on a set of three ring-type specimens with dimensions conforming to Table 10 from the previous chapter. While not conclusive due to testing error, these first tests did identify both numerical modeling improvements and physical design improvements necessary for improved precision in predicting brace hysteretic response. Physical improvements are then discussed and the third portion of experimental test results are presented. These results evaluate the effectiveness of the physical design modifications as well as identify another area of necessary improvement in the FE model.

5.1 Coupon Tests

It is necessary to know the actual material properties of the steel used to cut the yielding plates, as these properties will directly influence the yield force and elastic stiffness. Therefore, coupon tests were performed following the standards of ASTM E8 (E28 Committee 2016). The material ordered for fabrication of the yielding plate was 11-gauge A1011-CS-B steel. According to ASTM standard specifications, this material is expected to have a yield strength between 30 and 50 ksi and a maximum strain at or above 25% (A01 Committee 2018). This material should therefore have a high amount of ductility, which is necessary for the purposes of this application. The thickness of 11-gauge standard steel is 0.1196 inches, and may vary due to allowable tolerance. While this is not the exact dimension of the originally designed part, it is the closest thickness of plate possible. The steel plate ordered was 4 ft. x 8 ft., so the remainder of yielding plates for this project can be cut from the same steel specimen. This avoids the necessity of having to retest different steel sheets prior to production of these devices in the future.

ASTM E8 testing methods specify specific coupon shapes for different types of materials. For standard, rectangular tension test specimens, there are two categories – plate-type and sheet-type. The minimum metal thickness for a plate-type specimen is 0.188 inches, and the maximum thickness for a sheet-type specimen is 0.750 inches. Because the thickness of the metal tested was 0.1196 inches, it did not meet the minimum requirement for plate-type specimens. It did, however, fall under the maximum allowable

thickness for sheet-type specimens, so this was the standard that was used. Figure 20 shows the dimensions specified for each coupon.

Coupons were cut using a waterjet at the same time the initial BRB testing specimens were cut. Three specimens were tested using the MTS 858 Table Top System. This machine has a load capacity of 25 kN (5.6 kips) and uses 647.25A hydraulic wedge grips. This is the same system that was used to conduct all cyclic component tests for model BRBs. The testing procedure is as follows:

- Lightly scratch the side of the specimen to mark a 2 inch axial distance in the reduced portion of the specimen.
- Center the specimen in the lower grip. Tighten.
- Place the machine in force control. Tighten the upper grip, ensuring the specimen remains plumb.
- Place the extensometer in the center of the reduced section.
- Begin the test using a crosshead speed control of 0.04875 in/min as specified by ASTM.
- Once the specimen reaches 2% strain, remove the extensometer and test at the same rate until failure.
- Measure the distance between the marks on the specimen at the end of testing to calculate the final elongation at failure.

This testing procedure was carefully followed and the resulting data analyzed for all three tests to determine the representative material properties for continued numeric analysis. All data sets had a distinct upper yield strength (UYS), lower yield strength (LYS), and yield plateau, matching the analysis case listed in ASTM E8 Section 7.7.3 for materials that exhibit discontinuous yielding (E28 Committee 2016). For the purposes of this project, the UYS was determined but ultimately neglected, and the LYS was used as the material yield strength because it corresponded more closely to the stress at level at the yield plateau. Figure 21 shows the calculated nominal stress-strain curve for all three tests. The calculated strain was determined using the extensometer up until 2% strain, which adequately defines the elastic zone. The calculated strain outside of this region used the machine displacement readings and assumed a uniform average strain across the reduced section length. The stress is calculated using axial force readings from the machine and assuming a uniform stress across the reduced section area. There may be slight error in this calculation method due to potential stress or strain concentrations and inaccuracies in machine displacement data; however, these errors are minimal and the resulting behavior is considered adequate for the purposes of the project. Table 11 reports the values for elastic modulus (E), LYS, UYS, and ultimate strength (F_u). Aside from the calculated elastic moduli, all values are very close for the three tests. This yields confidence in the accuracy of the data. The initial stress-strain relationship was not truly linear, so the elastic modulus was

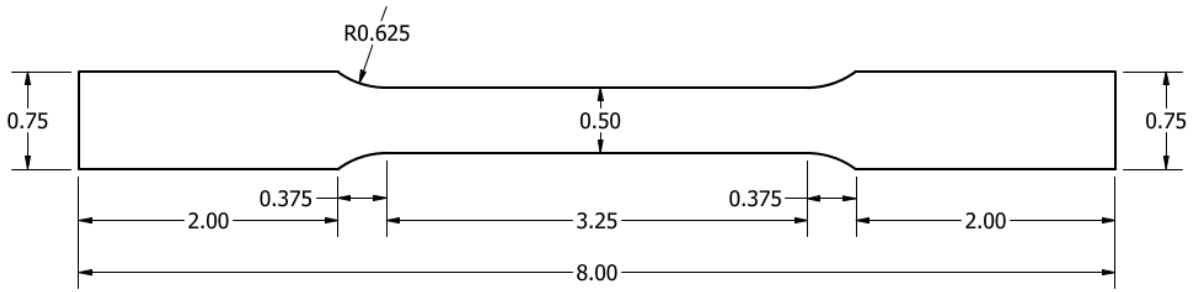


Figure 20. Sheet-type coupon for tensile testing.

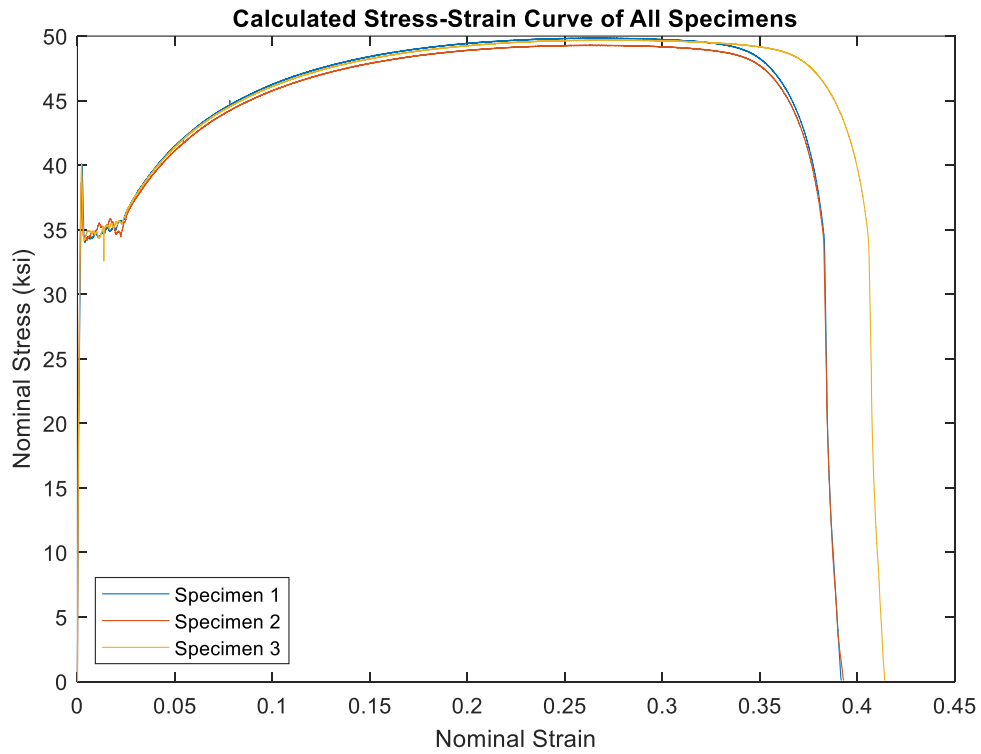


Figure 21. Nominal stress-strain behavior of 11 gauge A1011-CS-B steel.

Table 11. Calculated values for coupon tests.

Specimen #	E (ksi)	LYS (ksi)	UYS (ksi)	F _u (ksi)
1	29,100	34.2	40.0	49.9
2	32,900	34.7	38.6	49.3
3	30,000	34.4	40.2	49.7

estimated using the secant modulus measured from the first to the fifth reading. The secant modulus was then used to define the elastic zone as having a linear stress-strain relationship based on Hooke's Law, as is common accepted engineering practice. The yield strain was then approximated as:

$$\varepsilon_y = \frac{LYS}{E} \quad (5.1)$$

Steel is known to have a modulus of approximately 29,000 ksi, so Specimen 1 was used as the representative sample to form the simplified material relationship shown in black on Figure 22. This simplified curve had to be manipulated even more for entry into the ABAQUS material module; however, this will be discussed in the following section when the numerical updating is addressed. Additionally, it was noted that the specimens fractured at very low loads and had a very high modulus of toughness. While measurements of final elongation at failure are prone to human error, both physical measurements and strains based on machine displacements indicate that the material has a failure strain of approximately 40%. This is high enough to provide the ductility necessary for the model BRB to function well as an inelastic energy dissipator.

5.2 Quasi-static BRB Testing

5.2.1 Testing Protocol for Initial Tests

The American Institute of Steel Construction (AISC) provides accepted BRB testing protocols in Section K3 of the Seismic Provisions for Structural Steel Buildings that are followed in the relevant literature (AISC 2016; Dehghani and Tremblay 2018; Gray et al. 2017). While this work is not a full scale BRB, it will still be subjected to the testing protocol of the current standard in order to validate the brace behavior. This testing protocol is described as follows. The variables used define the axial brace displacement value during testing (Δ_b), the expected brace axial displacement value at brace yield (Δ_{by}), and the expected brace axial displacement at the design story drift (Δ_{bm}).

- Two cycles of loading at the deformation corresponding to $\Delta_b = \Delta_{by}$
- Two cycles of loading at the deformation corresponding to $\Delta_b = 0.5 \Delta_{bm}$
- Two cycles of loading at the deformation corresponding to $\Delta_b = 1.0 \Delta_{bm}$
- Two cycles of loading at the deformation corresponding to $\Delta_b = 1.5 \Delta_{bm}$
- Two cycles of loading at the deformation corresponding to $\Delta_b = 2.0 \Delta_{bm}$
- Additional cycles of loading at the deformation corresponding to $\Delta_b = 1.5 \Delta_{bm}$, as required for the brace test specimen to achieve a cumulative inelastic axial deformation of at least 200 times the yield deformation

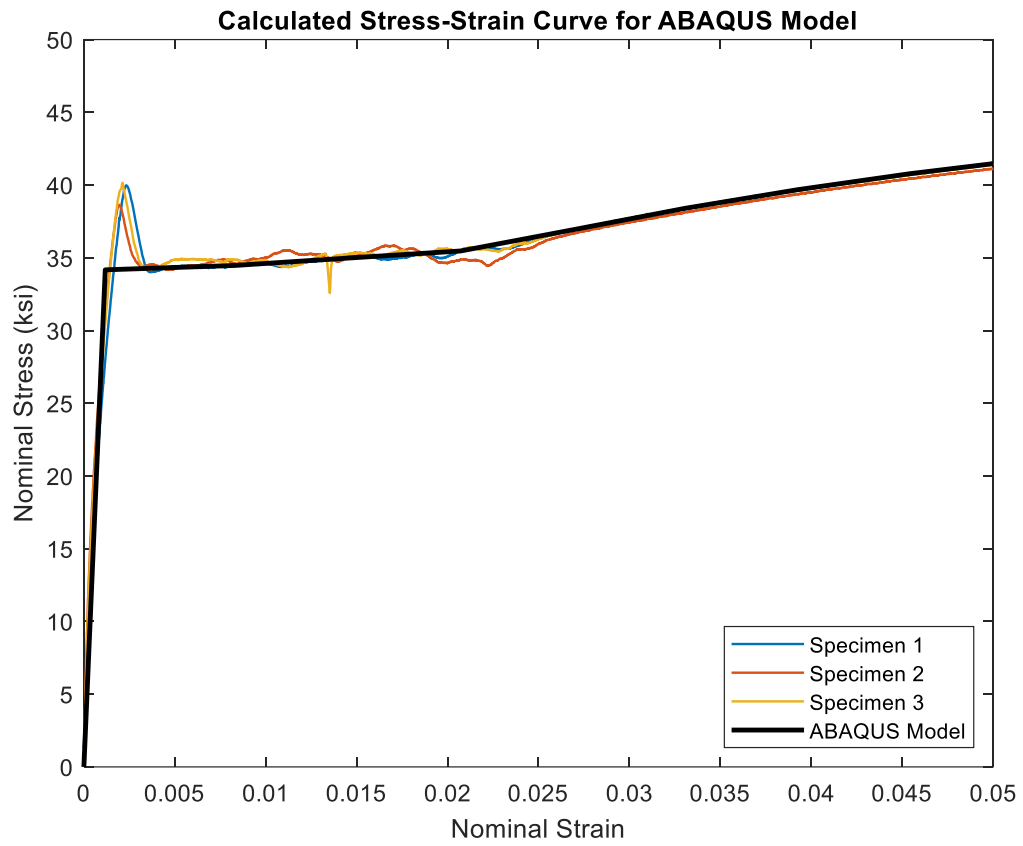


Figure 22. Representative stress-strain behavior.

Showing only 0 to 0.05 strain to better see the fit of the simplified model.

The above protocol was followed, but an additional step was added at the beginning of the test protocol:

- Two cycles of loading at the deformation corresponding to $\Delta_b = 0.5 \Delta_{by}$

These additional two cycles of load were added to ensure the elastic response of the BRB was captured since the estimate of yield displacement was not known to be accurate.

The first set of tests featured three sizes of BRB – small, medium, and large. The small BRB is named “T1S1”, the medium BRB is labeled “T1S2”, and the large BRB is labeled “T1S3”. The yield displacement value for testing protocol was estimated using the procedure described in chapter 4. The values of these estimated yield displacements were previously presented in . Determination of Δ_{bm} was less straightforward. This quantity represents the expected brace axial displacement at the design story drift, and is not to be taken less than $0.01h_s$, where h_s represents the story height. It is not currently known what the exact design story drift is for the experimental structure. Therefore, previous works in the literature were consulted to determine a reasonable assumption for the brace deformation at design levels. Tremblay et al. concluded that using $\Delta_{bm} = 5.0 \Delta_{by}$ was sufficient, based on the then proposed NEHRP provisions (Tremblay et al. 2004). Simpson used a different approach and defined the brace axial deformation as being $\Delta_{bm} = 2 C_d \Delta_{by}$, where C_d is the deflection amplification factor for BRBs as defined in ASCE-7-16 (ASCE 2017). Using all three methods to calculate Δ_{bm} , the values presented in Table 12 are obtained. The minimum AISC requirement controlled for both T1S2 and T1S3. The estimation from Simpson was slightly higher for T1S1. As stated before, the yield displacement of the specimens was estimated using ABAQUS, but was not certain. In light of this, and in order to keep the displacement control as similar as possible for all tests, the minimum AISC requirement of $\Delta_{bm} = 0.13$ inches was chosen. After choosing the design Δ_{bm} , it was determined that there was no need for additional cycles after $\Delta_b = 2.0 \Delta_{bm}$ because the brace had already reached a cumulative inelastic deformation of over 200 times the yield deformation by this point.

The next step in the displacement control process was to determine the loading rate. This was accomplished via guidance from the previous coupon testing protocol. According to ASTM, tensile specimens are to be loaded at a rate of 0.015 times the reduced section length (in./min.). The model BRB is not a simple mechanism and therefore does not have a reduced section length. However, it seems reasonable to use an average specimen diameter as the “length of the reduced section” since the majority of strain is to be concentrated in the central ring. Using an average diameter of 2.0 inches, the initial displacement rate was set at 0.030 in./min. This is a reasonable rate for the initial test cycles, but it is unreasonable to continue the test at such a slow pace for all cycle amplitudes. Guidance from ASTM specifies an acceptable displacement

Table 12. Calculated values for Δ_{bm} . Values reported in inches.

Specimen	Minimum per AISC	Tremblay et al.	Simpson
T1S1	0.13	0.078	0.156
T1S2	0.13	0.0605	0.121
T1S3	0.13	0.0605	0.121

rate of between 3 – 33 times the initial rate for post-yield displacement in specimens where the expected maximum strain is greater than 5% and the material behavior is not sensitive to displacement rate. Fracture of the material is not expected before 40% strain, and the application of the device as an energy dissipator during earthquake ground motions implies that the testing rate should not affect performance. Therefore, the displacement rate was increased for cycles after yield such that the total test time per specimen was approximately 45 minutes. A visual representation of the displacement pattern is shown in Figure 23.

5.2.2 Instrumentation

The MTS testing machine has the capability to measure both axial force and axial displacement, but it was initially unknown if the axial displacements measured by the machine would be representative of the axial displacements between connection points of the specimen yielding plate. So, an external LVDT was attached between the yielding plate connection points. To accomplish this, several LVDT brace components were manufactured from 1/2-inch-thick aluminum. These are shown in detail in the drawing set in Appendix A. The overall test setup and bolt connection layout is shown in Figure 24. The LVDT used has a displacement range of ± 1 inch, so the height of the lower brace resting point was set to accommodate this. The thickness of the gripping plates was decided specifically for these component tests. The serrated grips that were compatible with the MTS testing machine required a gripping thickness of 0.28-0.57 inches. The gripping plates were therefore fabricated from 0.375-inch-thick steel to comply with these requirements. The use of the serrated grips was preferable to decrease likelihood of slipping within the grips during testing.

5.2.3 Initial Test Results

Specimen T1S1 and T1S2 were tested prior to realizing there had been a mistake in machine set-up that resulted in unwanted crosshead movement. While this meant the results from these two tests could not be fully trusted, there were still valuable lessons learned about the device from these failed attempts. Figure 25 shows the force-displacement curve of specimen T1S1 using both the LVDT displacement readings and the machine displacement readings. It is evident that there is disagreement between the two forms of displacement readings, which visually confirms the error in test set up. Additionally, there was a displacement programming error captured during this test in which the last cycle did not include the negative displacement amplitude. This issue was fixed prior to continuing testing. Other than the set-up errors, the lesson learned during this test was that the bolts holding the mechanism together need to be tighter. There are visible points of load reduction at high tensile force, which indicates there is slip in at least one of the connections. In addition, a small gap between the yielding plate and the confining plate was observed at high compressive load, which indicated out-of-plane buckling, shown in Figure 26. To counteract the first phenomena, bolts 1A and A2 were torqued to 40 ft-lb prior to testing of specimen T1S2. It was noted bolts C1 – C4 were initially tightened less than finger tight in an attempt to decrease frictional

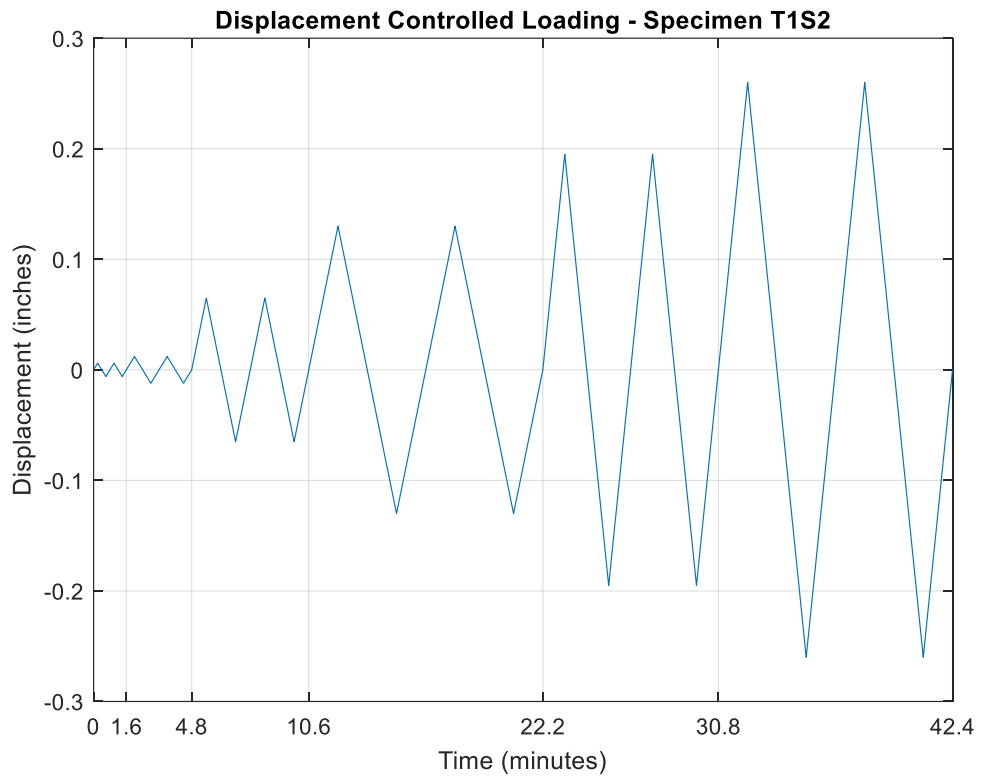


Figure 23. Displacement control for specimen T1S2.

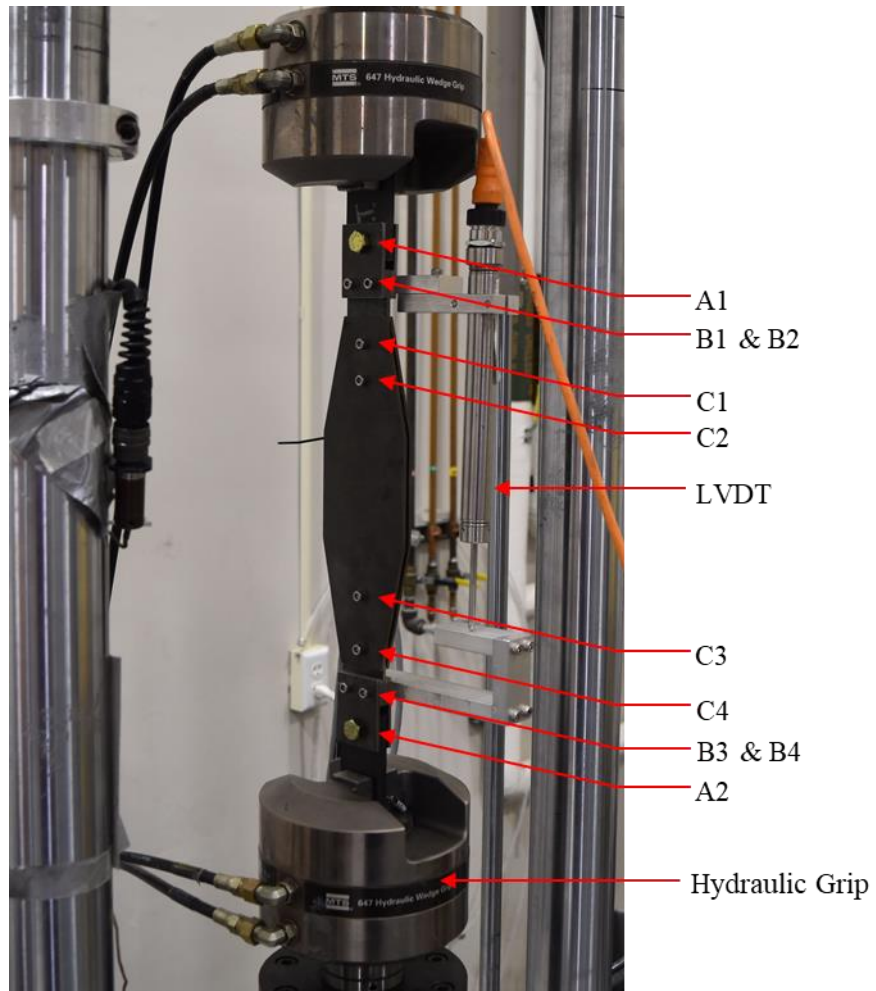


Figure 24. Test setup & bolt layout.

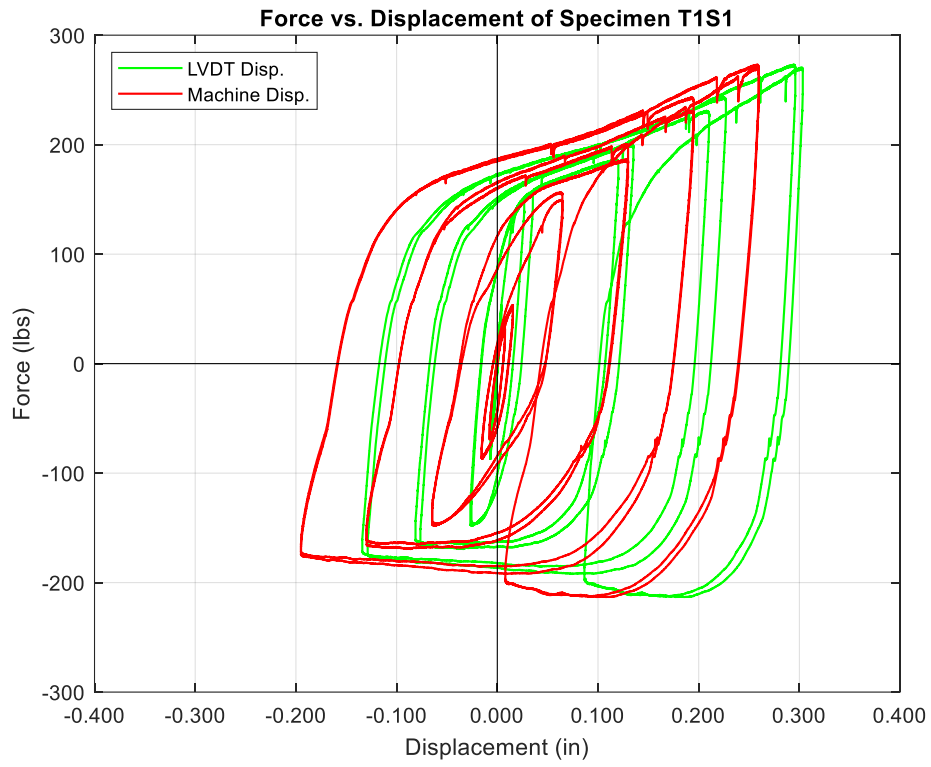


Figure 25. Force vs. displacement curve of specimen T1S1.

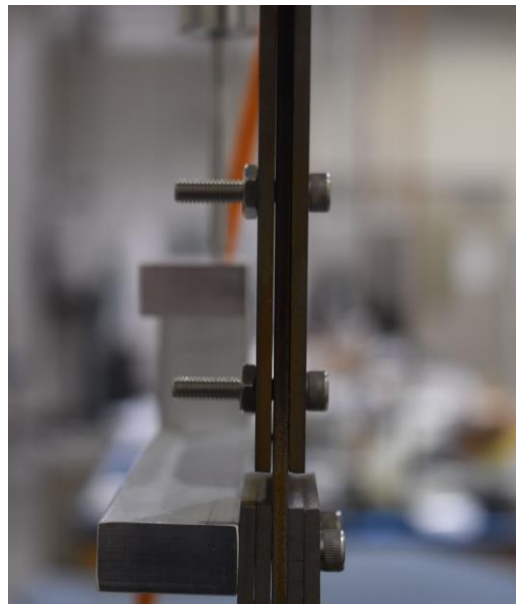


Figure 26. Out-of-plane buckling of T1S1.

interaction between the plates. While the friction may have been lowered by this choice, the usefulness of the restraining mechanism was also lowered. To reduce the potential for buckling, bolts C1 – C4 were tightened with a wrench at the beginning of the test for specimen T1S2.

The error in the displacement readings was initially attributed to a poorly calibrated LVDT within the MTS testing machine, so the error in crosshead movement was not fixed prior to testing of specimen T1S2. The crosshead movement was identified part way through the second test. Once this was fixed, it was decided to cycle the BRB at the two highest displacement cycles to capture the end of the desired response. Figure 27 shows the initial cycle at the second highest displacement value. The axial forces were almost 3 times the expected value based on the numeric analysis at the time. This was very unexpected, and was hypothesized to stem from overtightening bolts C1 – C4, which led to increased friction that enabled the restraining mechanism to resist some of the axial load and led to increased axial force capacity. The test was again stopped and a third set of data was gathered after loosening bolts C1 – C4 to be finger tight. After this, the maximum recorded load was only 1.2 times the expected load at that displacement level, shown in Figure 28. This shows that the tightness of bolts C1 – C4 is very important. They cannot be too loose because this renders the confining plates less effective than necessary, as seen in specimen T1S1. However, they cannot be too tight because this restricts the necessary relative displacement between the confining plates and the yielding plate. The effect of this restriction was seen when the mechanism was disassembled. Figure 29 clearly shows the wear around the slotted holes where the bolt tightening caused increased frictional resistance between contact surfaces as the yielding plate attempted to displace.

Specimen T1S3 gave the best result from this initial testing. Bolts A1 and A2 were torqued to 40 ft-lb as done for specimen T1S2, and bolts C1 – C4 were tightened to finger tight – no looser, but also no tighter. Figure 30 shows the experimental data on the same graph as the initial ABAQUS analysis results. There are several key takeaways from this comparison. First, the device seems to provide a full, stable hysteretic response as desired. Second, the elastic region appears to be well estimated using FE analysis. The initial stiffness and yield behavior match quite well. Third, there is a slight jog in the curve just before 200 lbs. in both tension and compression on all cycles past yield. This indicates that there is some slip in the connections. This slip is present in both the displacement data gathered from the MTS testing machine and from the LVDT. This indicates that the slip is occurring at bolts 1B – 4B, not in bolts A1 and A2. Updated connection detailing to fix this problem will be discussed in the subsequent chapter. Lastly, it is clear that while the FE analysis estimated the elastic response quite well, the estimated force levels of the higher amplitude cycles are much too high. This indicates that the hardening model used in the numerical analysis was incorrect. This will also be addressed in chapter 6.

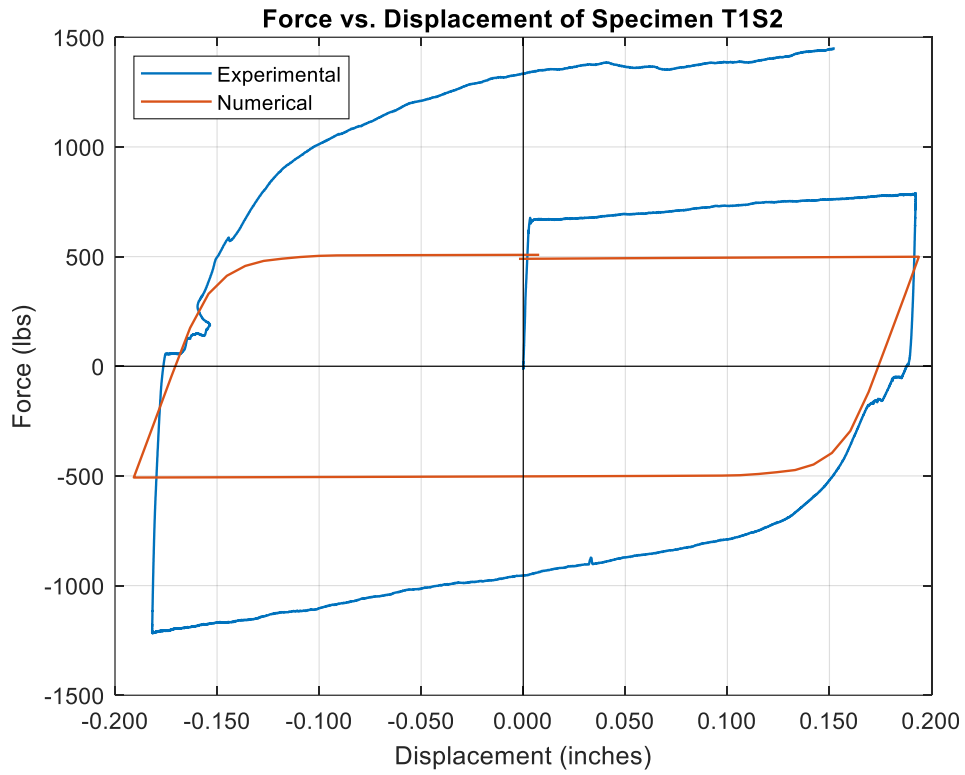


Figure 27. Force vs. displacement curve of specimen T1S2. Bolts C1-C4 tightened.

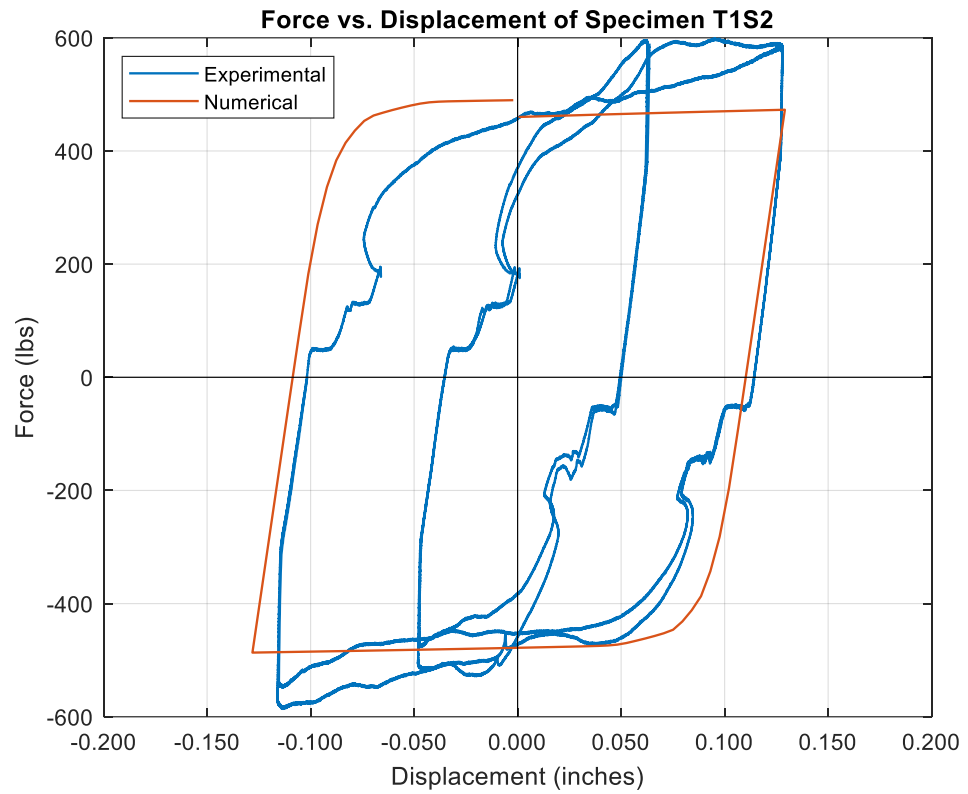


Figure 28. Force vs. displacement curve of specimen T1S2. Bolts C1-C4 loosened.

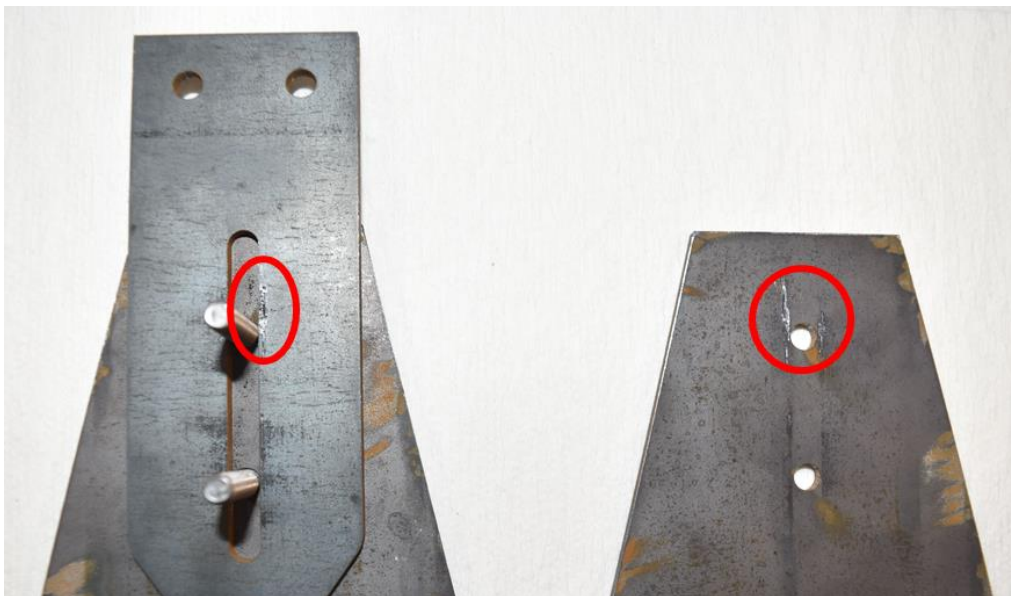


Figure 29. Disassembly of components showing wear on the contact surface (circled in red).

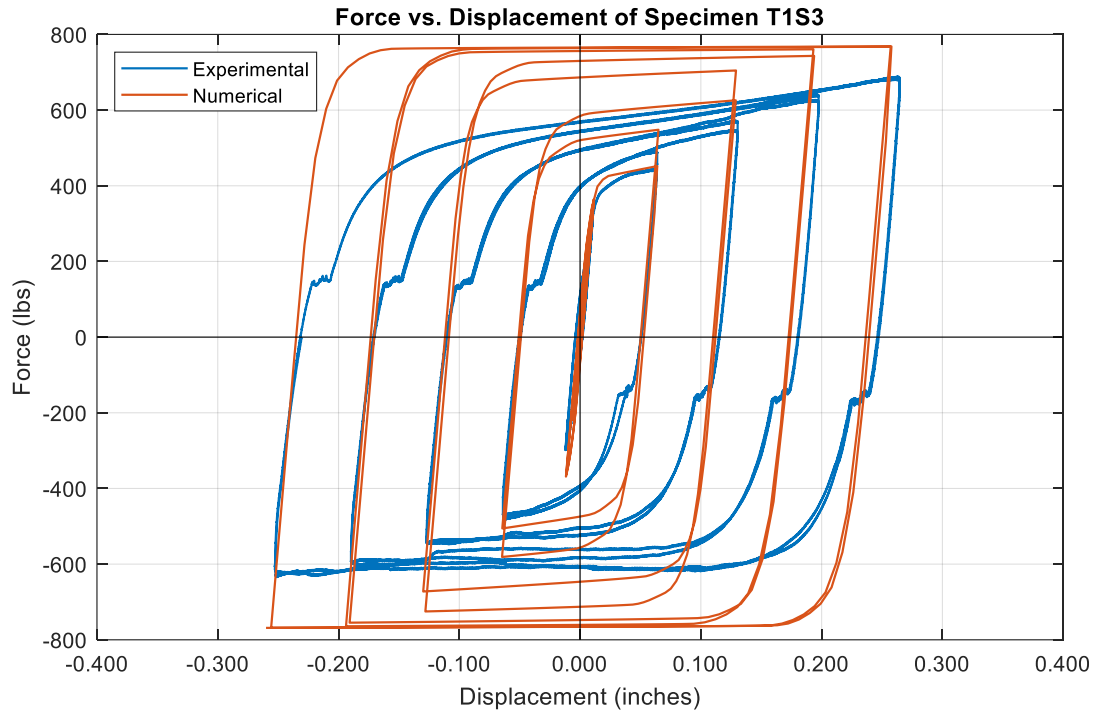


Figure 30. Force vs. displacement curve of specimen T1S3.

5.2.4 Testing Protocol for Second Tests

Initially, the model BRB displacement control included $\Delta_b = 2.0\Delta_{bm}$ as the maximum amplitude displacement. As previously stated, the actual expected maximum displacement is currently unknown, but it may be higher $\Delta_b = 2.0\Delta_{bm}$. For the second set of tests, a modified displacement protocol was designed such that the BRB was subjected to a 5% story drift at the maximum amplitude. Using terms as defined in Figure 31, the original length of the model BRB, L , is:

$$L = \sqrt{h_s^2 + (w/2)^2} \quad (5.2)$$

At 5% drift, small angle approximations are still valid, and the new brace length is:

$$L_{new} = \sqrt{h_s^2 + [(w/2) + \Delta_s]^2} \quad (5.3)$$

Where : $\Delta_s = 0.05 \times h_s$.

The change in length of the model brace is then calculated to be 0.4042 inches at 5% story drift. This is less than the maximum brace axial displacement of 0.50 inches. To test the brace behavior at larger displacement, two cycles at a displacement of $\Delta_b = 0.4042$ inches were added after the original cycles described previously. In order to keep the test time at approximately 45 minutes, the displacement rates were increased more than original for cycles after yield. The highest rate of displacement was still less than the ASTM recommended maximum. Figure 32 is a visual representation of the displacement control for specimen T2S3.

5.2.5 Connection Revisions and Second Test Results

While the initial model needed improvement, the overall initial results provided good confidence that the device would function adequately with some revision. The main concern identified was that of slip between the plates at the connections. This problem was addressed by tightening bolts A1 and A2 to a specified torque. The connection at bolts B1 – B4 was not so easily resolved because of the necessary connection to the LVDT brace. This connection location is especially critical because there are four faying surfaces and thus ample opportunity for slip. The initial connection was designed to tighten as the bolts were screwed into the aluminum braces, as shown in the bottom of Figure 26. This figure also shows the space between different pieces in this connection during compressive load, indicating that the connection was not secure. To fix this, the solution shown in Figure 33 was designed. Each splice plate was welded to its corresponding filler plate, since there is no need for these pieces to be taken apart. Vinyl friction tape was wrapped around the end of the yielding plate to increase the coefficient of friction at the connection surface. The bolt length was increased at location B1 – B4 to accommodate the placement of a nut between the filler plate and the

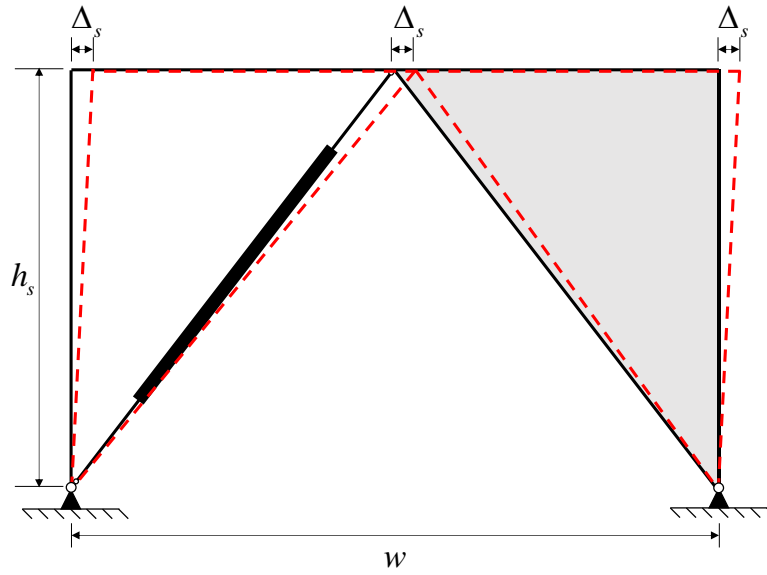


Figure 31. First story of frame shown at prescribed story drift.

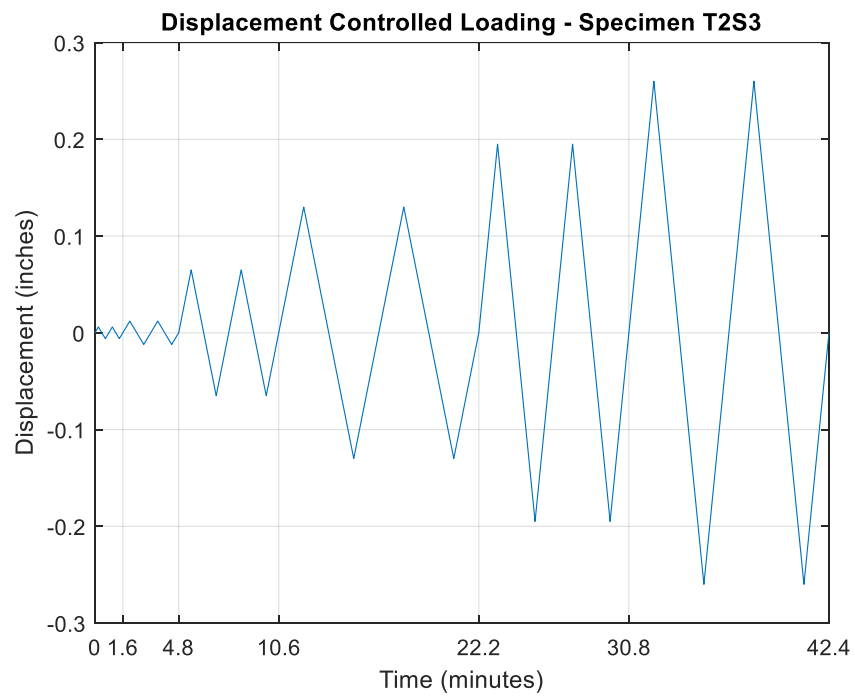


Figure 32. Displacement control for specimen T2S3.

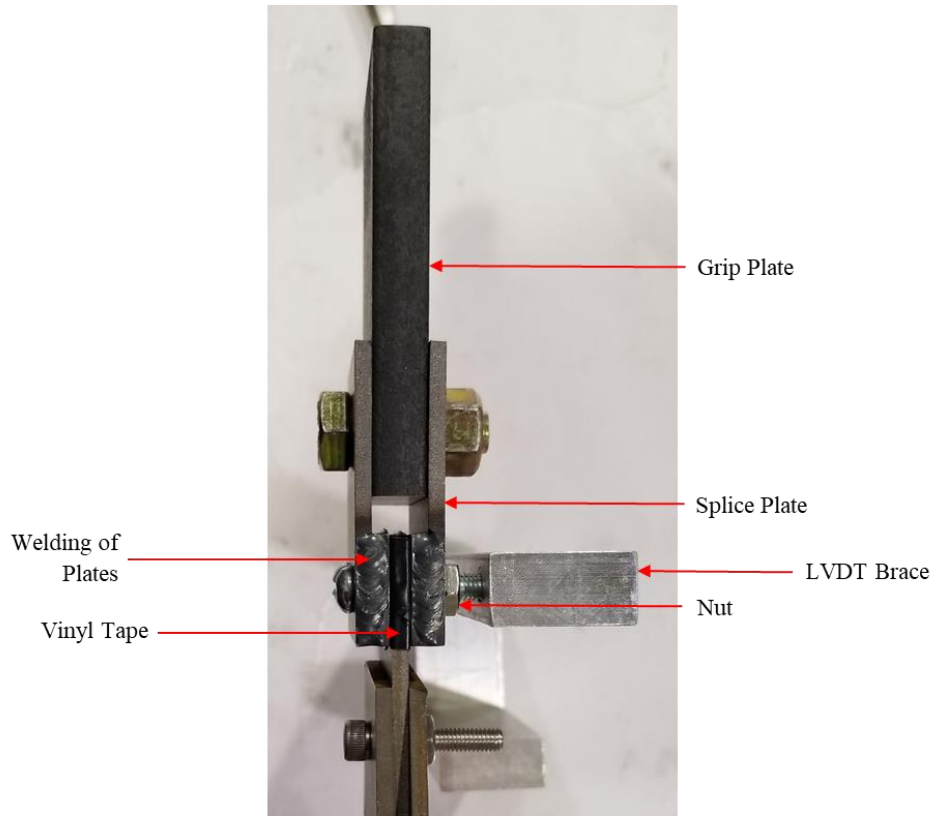


Figure 33. Initial improved connection.

LVDT brace. Upon assembly, the bolts were first screwed securely into the LVDT brace. Then, the nuts were tightened as tight as possible with a wrench.

The following tests will be referred to as “T2SX”, where X represents the test number. Dimensions of the yielding plates remained unchanged, which facilitates easier comparison to initial results. Specimens T2S1 and T2S2 were the small BRB size. Specimens T2S3 and T2S4 were the large BRB size. There was visual misalignment of the holes at bolts B1 and B2 after connections were complete for T2S1. This was initially considered a manufacturing error unique to the T2S1 yielding plate, and no conclusive tests were performed. However, specimen T2S2 appeared to have the same misalignment. It was then determined that the holes in the splice plate/filler plate connection had more clearance than originally thought, likely due to slight expansion from heat due to welding. This problem was overcome by manually aligning the connection prior to complete tightening of bolts B1 and B2. This did not appear to negatively affect brace performance. However, another issue was identified during the first two amplitudes of displacement for T2S2. Figure 34 shows the initial hysteretic curve. The behavior is not repeatable, and the measured displacements do not match the amplitude given for the cycle. Also, instead of the expected full hysteretic curve, the unloading curve shown by the red arrows is more similar to a flag shaped hysteretic curve that one would observe in a mechanism such as a friction spring damper (Wang et al. 2019). This behavior, coupled with the lower than expected forces at yield displacement, showed there was a significant problem with design improvements. Because of the abrupt softening of the curve upon unloading, it was theorized that the vinyl tape was causing more slip rather than creating less slip as intended. While the tape does increase the static coefficient of friction, the vinyl material has both a low shear strength and a low bond strength with the metal. This enabled more relative movement between the yielding plate and the filler plate at lower force.

The tape was removed and the connection updated to reflect that of Figure 35. After this, the full test protocol, including the two cycles at 5% story drift, was completed for T2S2. Results are shown in Figure 36. There are two main conclusions drawn from this data. First, the elastic portion of the data again matches the elastic analysis previously performed in ABAQUS. Calculating the average slope of the elastic tensile and compressive regions provided an experimental elastic stiffness of 10,483 lb./in. Finding the intersection point between the average elastic slope and average initial plastic slope in the tensile region provided an experimental yield force of 130.5 lbs. and an experimental yield displacement of 0.0127 in. These values are compared to the estimated elastic stiffness of 8,450 lb./in., a yield force of 132.0 lbs., and a yield displacement of 0.0156 in. Specimen T2S2 was stiffer than predicted, which led to a lower yield displacement value. But, the estimation of yield force was still close to accurate. Secondly, one can observe

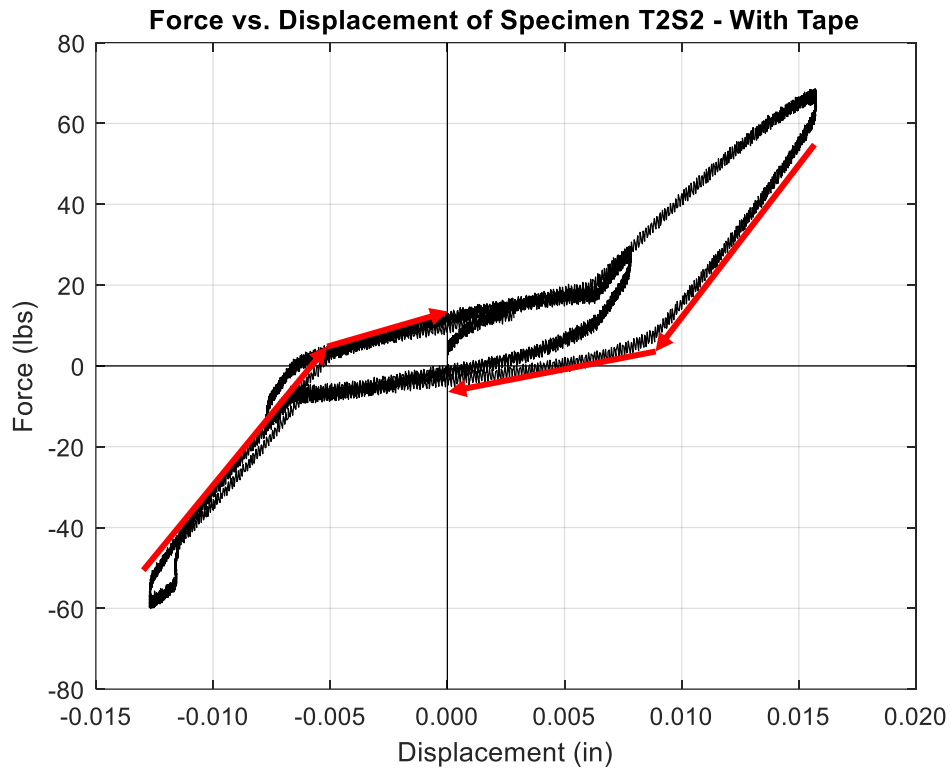


Figure 34. Initial flag shaped hysteresis of T2S2.

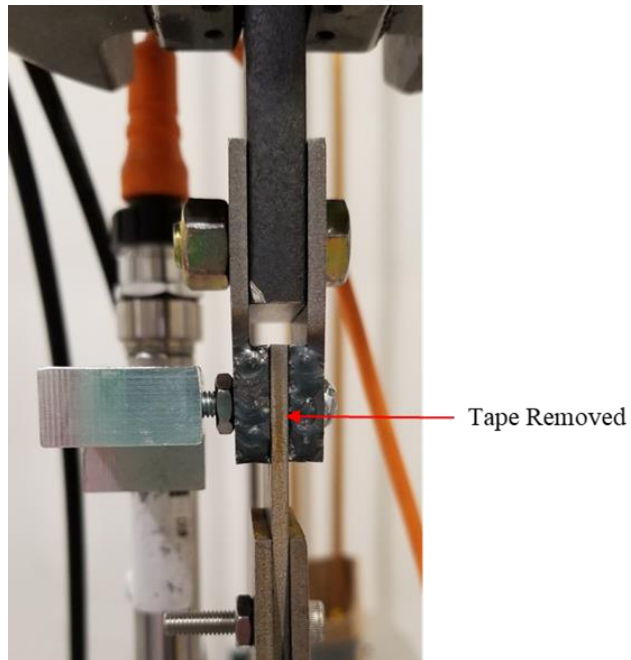


Figure 35. Connection detail with tape removed.

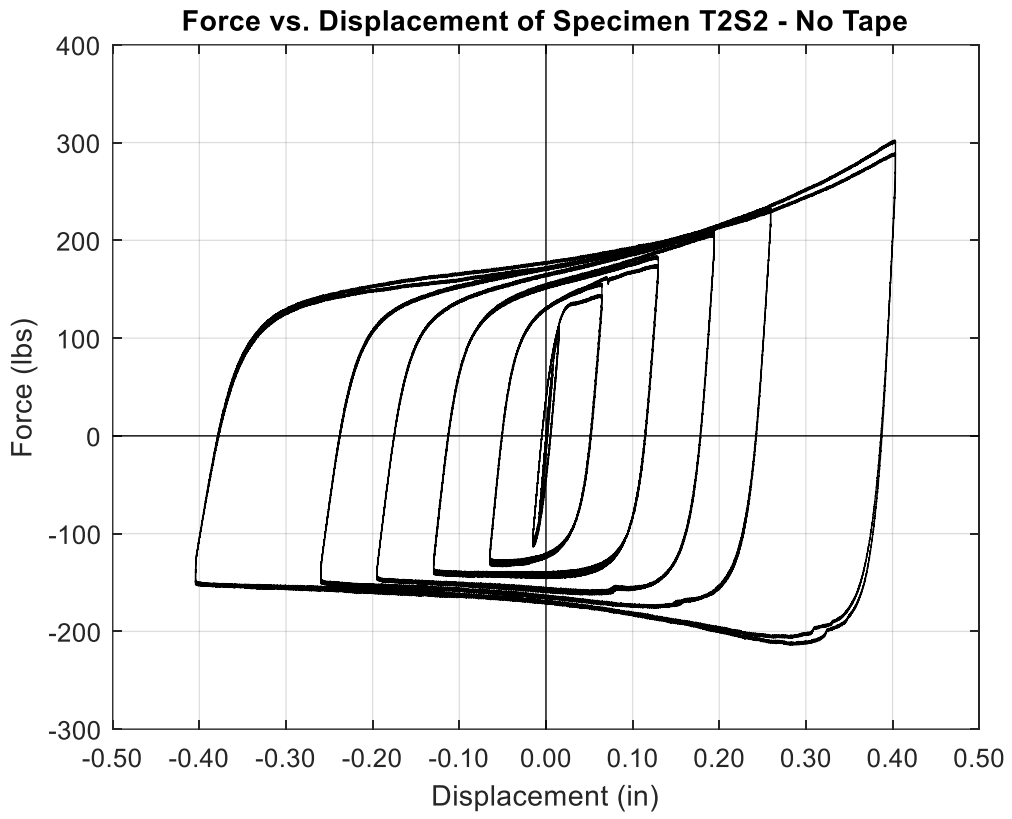


Figure 36. Full hysteretic curve of T2S2 - No Tape.

the continually increasing tensile capacity in conjunction with the softening behavior of the compressive curve. Similar to the material hardening inconsistencies, this phenomenon was not initially present in the FE analysis. Both of these behaviors are essential to proper design and will be addressed in the model updating portion of this thesis in chapter 6.

Specimens T2S3 and T2S4 were both large BRB yielding plates. These results, combined with the initial large specimen (T1S3), provided a good basis for determining the average behavior of this size of model BRB. The initial elastic stiffness, yield force, and yield displacement were calculated using the same method as previously described. The results from these calculations, the mean value, and the maximum deviation from the mean for each parameter are shown in Table 13. Notice that the calculated yield force and yield displacement are much higher for specimen T2S3 than for the other two specimens. This could be an area of concern; however, overall hysteretic behavior does not appear to be significantly affected by this variation. This shows that even if the yield force is higher than expected, the overall hysteretic behavior of the device is predictable. Ignoring the outlier in the experimental data, the calculated values are close to expected. Similar to the small BRB, the estimated yield force and yield displacement was slightly high. The estimated elastic stiffness was slightly low. The difference in tensile force capacity and compressive force capacity is evident in Figure 37 just as it was for the small specimen in Figure 36. Therefore, this behavior is not limited to low force model BRBs. However, it is not as exaggerated in the larger specimen. A final observation that can be made from these results is that the updated detailing in the connection appears to mitigate the slip present in the hysteretic curve. However, there is still a very slight amount of slip noticeable at a higher force. This solidifies the theory that the connections must be as tight as possible so as to provide smooth force-displacement behavior.

5.3 Conclusions Based on Experimental Tests

5.3.1 Impact of Manufacturing Tolerances

An observed trend was that the estimated yield force and yield displacement were slightly high, while the estimated elastic stiffness was slightly low for both sizes of BRB when compared to experimental data. Some of these differences are attributed to the simplifications used in the ABAQUS analysis. For example, the numerical model ignored the impact of friction. There was physically some friction present due to the interaction between the confining plates and the yielding plate. This frictional force could have resisted initial movement, which would have caused the experimental force values to be higher than those obtained in numerical simulation. These higher forces at the same displacement would produce a higher calculated stiffness. While this is a potential concern, the overall impact of ignoring friction in the numerical model

Table 13. Calculated parameter values for large experimental BRBs.

Absolute Values				
Specimen #	C/T	Yield Force	Yield Displacement	Elastic Stiffness
T1S3	T	394.2	0.0110	35,257
T2S3	T	461.1	0.0131	34,889
T2S4	T	397.7	0.0108	36,878
Average		417.7	0.0116	35,675
Max. % Deviation		10.4%	12.6%	3.4%

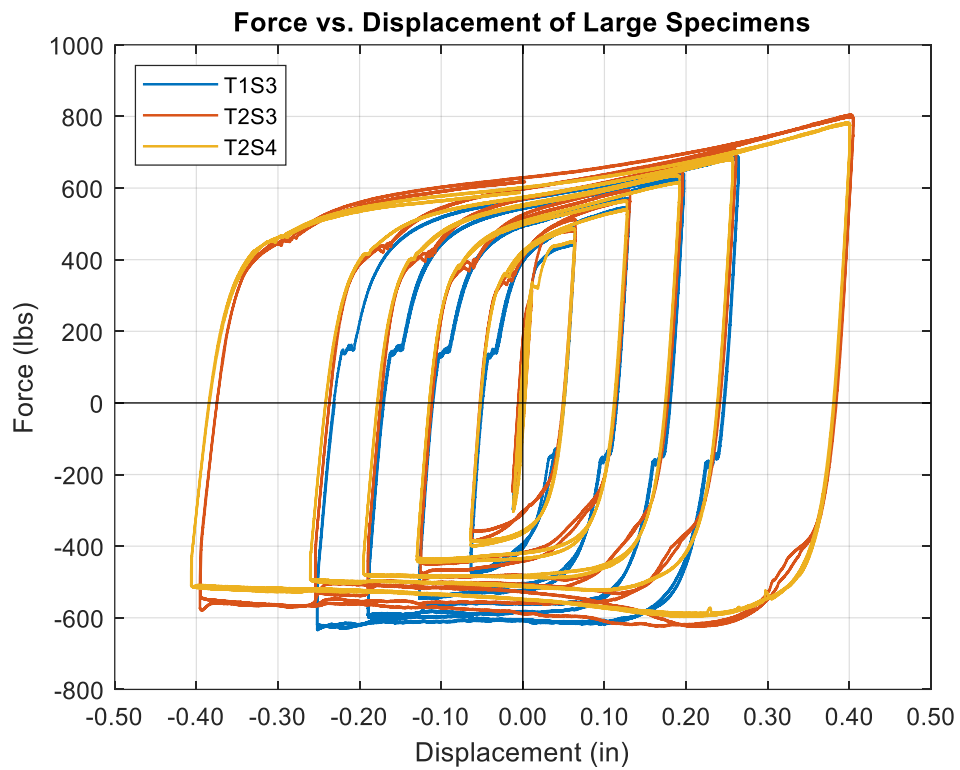


Figure 37. Hysteretic curves of all large BRB specimens.

seems negligible. Also, the percent error in stiffness decreases with an increase in BRB size and force demand. This indicates an absolute error, which is not characteristic of frictional forces.

Another likely explanation for the difference in expected and observed parameters are the manufacturing tolerances discussed in chapter 3. The estimated parameter values in Table 10 assumed nominal dimensions for average ring radius and ring width. As shown in Table 14, the measured average ring radius was within the expected tolerance of ± 0.015 in. previously observed for the waterjet machine, but the measured ring width was sometimes outside of these observed boundaries. The tolerance values were calculated by subtracting the nominal dimension from the measured dimension. Therefore, a negative tolerance means the actual value was smaller than nominal, and a positive tolerance means the actual value was larger than nominal. In all cases, the measured average ring radius was smaller than nominal. A smaller radius makes the ring stiffer, which correlates well with the higher experimental elastic stiffness values. In some cases, the ring width was smaller than nominal, and in other cases it was larger than nominal. It is therefore difficult to form any hypothesis on what effects this variation in parameter had on final results. Even so, it is reasonable to conclude that the manufacturing tolerances likely caused some of the observed differences between experimental and estimated parameters.

5.3.2 Experimental Observations & Overview of Model Updating

While experimental testing did not validate the original design, it did provide important insight into improvements that must be made for accurate FE analysis of future improved designs. The main two improvements that must be made are (1) updating the hardening model and (2) modifying the analysis procedure such that the increased tensile capacity is adequately captured. Both of these improvements will be discussed in the following chapter. Another important conclusion of the experimental portion of this work is that the tightness of the connections is an important factor in the fullness and smoothness of the hysteretic curve. This conclusion does not require any more attention at the current time, but it is important for future work involving connection of the BRB analog to the larger test frame.

Table 14. Measured manufacturing tolerances.

Manufacturing Tolerances			
Identifier	Specimen Size	b (in.)	R (in.)
T1S1	Small	0.0058	-0.0020
T2S1	Small	-0.0022	-0.0004
T2S2	Small	0.0006	-0.0015
T1S2	Medium	0.0056	-0.0012
T1S3	Large	0.0072	-0.0002
T2S3	Large	-0.0016	-0.0002
T2S4	Large	-0.0011	-0.0008

Chapter 6

6 Model Updating

The experimental results showed that, while the initial FE analysis provided in chapter 4 was adequate for the elastic region of the cyclic test, it was not adequate to predict the specimen plastic behavior. While the elastic zone parameter predictions were not exact, it was previously discussed that this disparity was likely due to manufacturing tolerances, not the material model used. However, the large differences in material hardening behavior observed cannot be attributed to inconsistencies in the experimental geometry. Therefore, significant changes in the ABAQUS plasticity model are necessary.

6.1 Isotropic and Kinematic Hardening

6.1.1 Differences in the Hardening Models

There are two main models used for material hardening definitions – isotropic and kinematic. The basic difference between these two models is in the constraints placed on the movement and expansion of the yield surface. Kinematic hardening, schematically shown on the left in Figure 38, causes the center of the yield surface to move in stress space once the state of stress causes the stress level to reach the edge of the original surface. This means the size of the yield surface remains constant but the center of the surface can move. Isotropic hardening, schematically shown on the right in Figure 38, causes the yield surface to expand in stress space once the state of stress causes the stress level to reach the edge of the original surface. This means that the center of the yield surface always remains at the origin but the size of the yield surface changes (Gong et al. 2010). In actuality, metals subjected to cyclic loads often behave in a manner that combines these two descriptors of hardening.

6.1.2 Purely Isotropic Hardening

Using the initial test data from T1S3, an investigation of differences due to material hardening was performed. Recall Figure 14 from chapter 3, which shows the geometry of the central yielding plate. For T1S3, nominal dimensions were as follows: dimension “A” was 2.555 inches, dimension “B” was 1.962 inches, and dimension “C” was 0.690 inches. Figure 39 shows the original cyclic numerical analysis using purely isotropic hardening on the same graph as the experimental results for T1S3. The original model allowed the yield surface to expand to the limits set by the ultimate stress. Once this stress state was reached, ABAQUS considers the model to behave in a perfectly plastic manner. This led to multiple errors, two of which are visually evident on the force-displacement curve shown in Figure 39. The axial force predicted

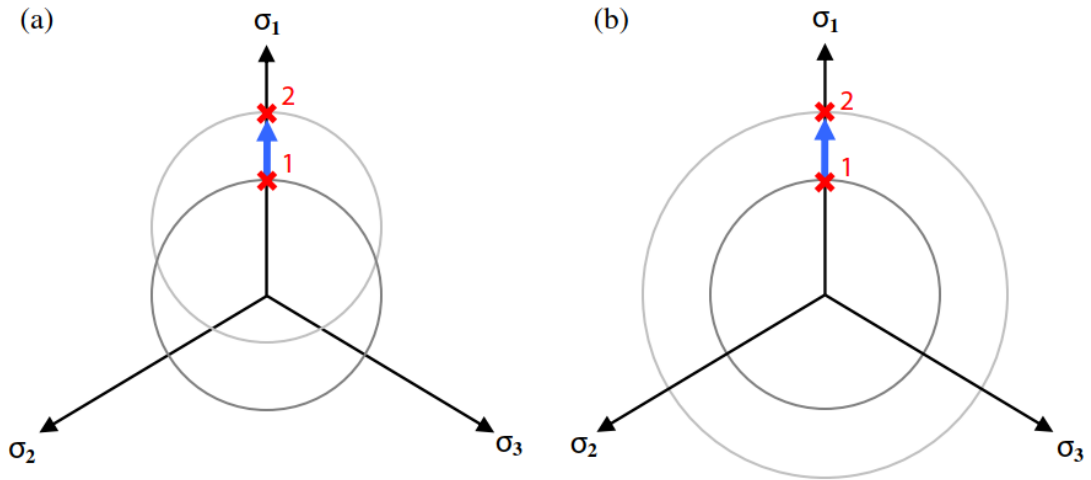


Figure 38. Schematic representation of (a) kinematic hardening and (b) isotropic hardening.

Reproduced from (Gong et al. 2010).

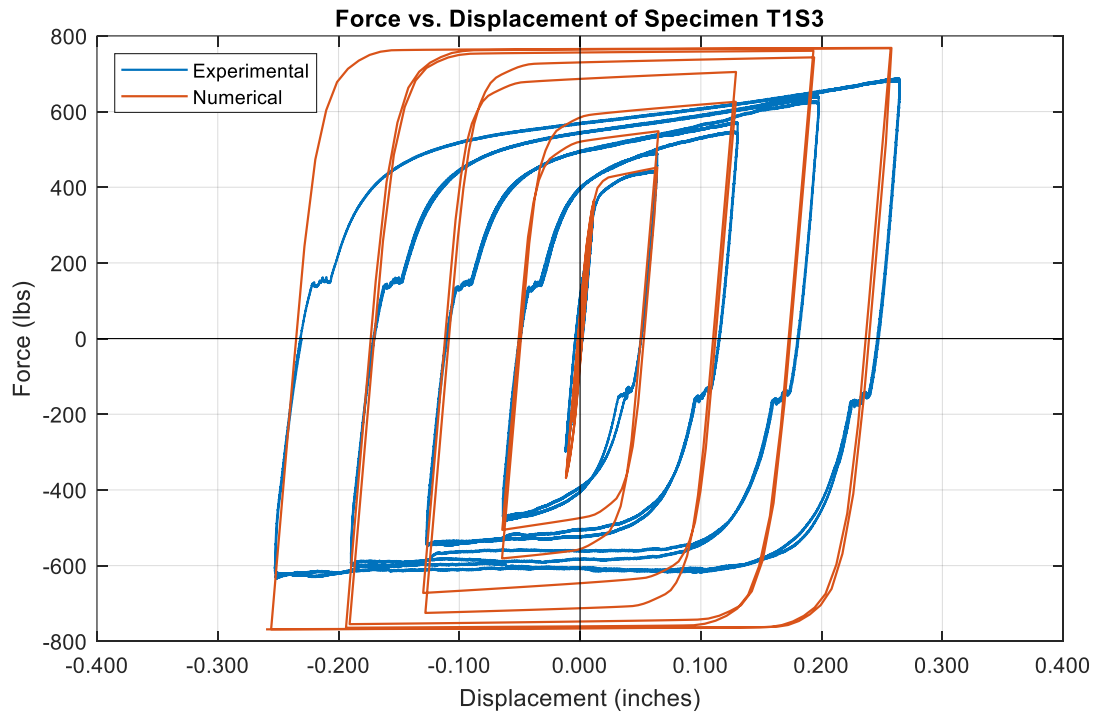


Figure 39. Isotropic hardening model from previous FE analysis.

by the model grows much faster than the experimental results. This inaccuracy leads to another inaccuracy – by the time the model reaches the last two displacement amplitudes, the hysteretic response is that of an elastic perfectly-plastic model.

6.1.3 Bilinear Kinematic Hardening

The purely isotropic hardening model has obvious and severe deficiencies in this application, so the next hardening model evaluated was a purely kinematic hardening. When using the “kinematic” hardening model in ABAQUS, one must define a constant hardening modulus using tabular data. The analyst inputs the stress at zero plastic strain in the first row of the table and then inputs a true stress-true plastic strain data point on the second row of the table that defines the post-yield kinematic hardening modulus of the material. Since this singular modulus will not represent the entire material behavior, the analyst retains the right to choose a hardening modulus that best describes the hardening in the strain range of interest. The strain range does not have to encompass the entire monotonic behavior. Rather, it is acceptable to enter a stress-strain point that is nearer to the maximum strain the part experiences during the test, or a stress-strain point that defines the average hardening modulus over the expected strain range. This is visually explained in Figure 40. In this figure, 4 different points along the true stress-true plastic strain curve were used to calibrate the kinematic hardening modulus. The theoretical behavior of the material is noticeably different for the different points used. If the ultimate point is used for calibration (shown in magenta), the material model misses the effect of strain hardening. If a point midway through the strain hardening range is used for calibration (both the green and red line shown), the numerical material model will achieve much higher stress capacities than physically available if the plastic strain is high. Therefore, one must have a good understanding of both the strain range of interest and the expected hardening behavior within that range of interest before deciding on a proper kinematic hardening modulus for use in the numerical simulation.

In this case, observed strains were at or below 0.1 during the entire test protocol, as seen in Figure 41. Therefore, a true stress-true strain pair at a plastic strain just past 0.1 strain was chosen to define the hardening modulus. This is shown in green in Figure 40. It is acknowledged that the unconventional part geometry of the yielding plate may lead to increased or decreased strains for different sizes of model BRB. While this means that the actual stress state of each element may be either under- or over-estimated using the bilinear kinematic model, the chosen hardening modulus provides true stress values that are within $\pm 5\%$ of average measured true stress for a plastic strain range of approximately 0.0 – 0.15. Therefore, this is considered as an adequate model for the purposes of this work. The result of this analysis is seen in Figure 42. The model now has the opposite problem as previously noted – the axial forces in the numerical analysis are much less than the experimental values. As previously discussed, this model also neglects the effects of

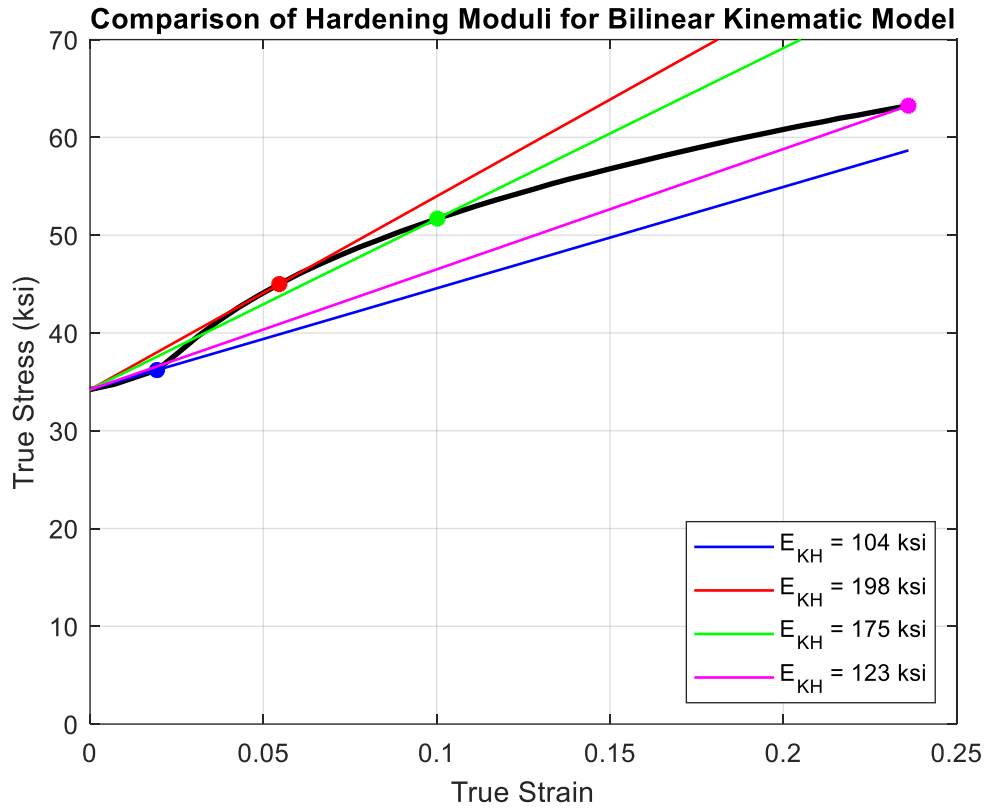


Figure 40. Comparison of kinematic hardening moduli using different calibration points.

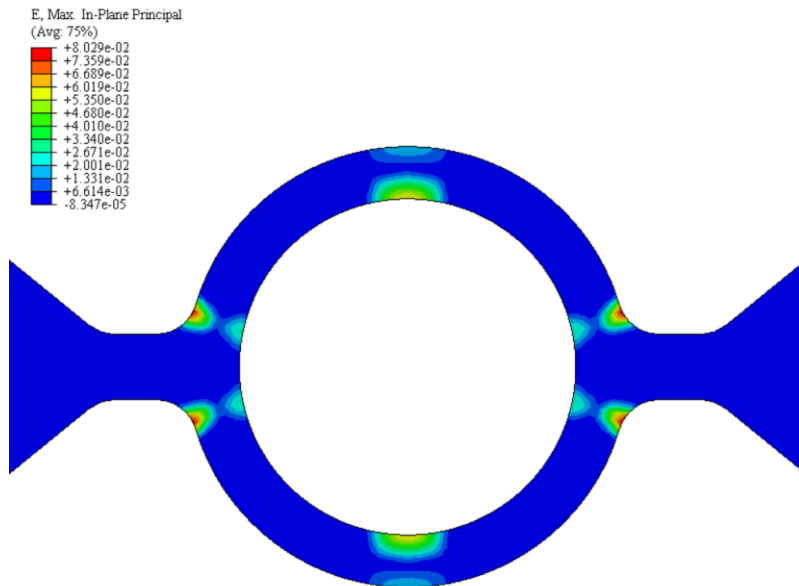


Figure 41. Average maximum strain in yielding plate. Ring only with no elements shown for clarity.

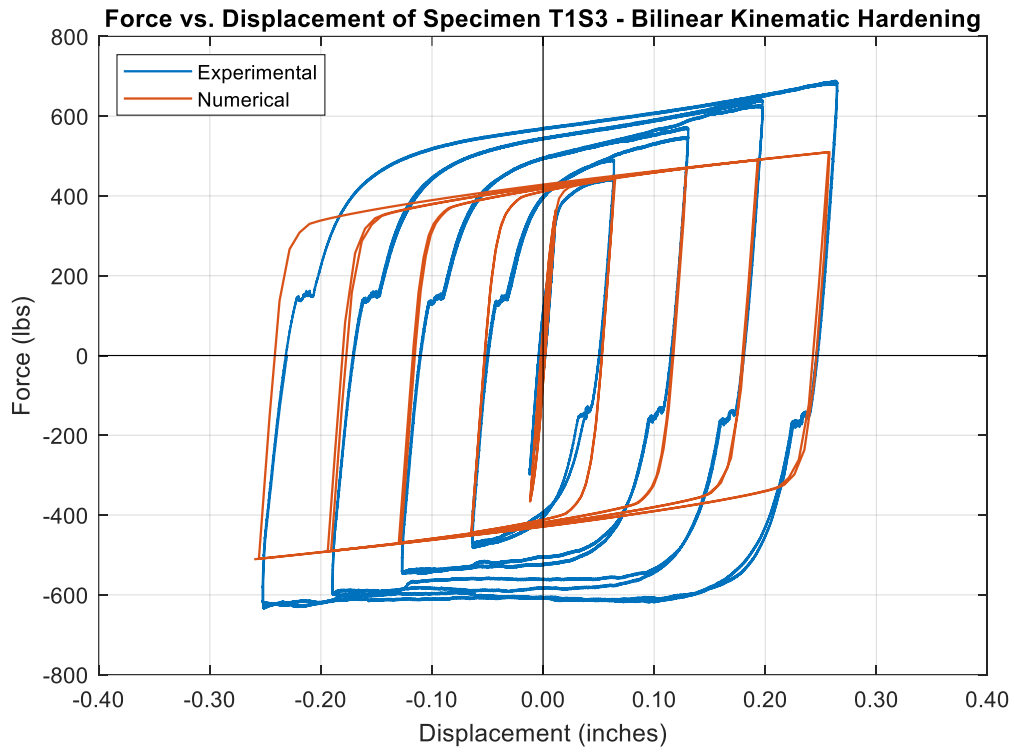


Figure 42. Bilinear kinematic hardening.

any changes in hardening behavior at different strain levels. In order to verify the extent of impact that variation in the hardening modulus may have on the behavior of this specimen, a multilinear kinematic hardening model was tested next.

6.1.4 Multilinear Kinematic Hardening Model

The multilinear kinematic hardening model improves on the weakness of the bilinear model by accounting for different hardening moduli at different strain levels. As seen in Figure 43, there is little visible difference in the overall specimen behavior between the bilinear and multilinear kinematic hardening models. The axial force capacity only increases by a maximum of approximately 6%. This shows that defining the hardening modulus in a more complex manner does not solve the overall modeling issues.

While these flaws demonstrate that the kinematic hardening model does not provide adequate numerical simulation regardless of the hardening modulus, this does not mean the model is useless. Bilinear kinematic hardening models are better at limiting the size of the stress surface during cyclic deformation than isotropic models. In the case of the isotropic model, the size of the yield surface is not constrained unless the stress state reaches the ultimate stress. Then, the stress surface becomes constrained to the size set by the ultimate state due to the elastic perfectly-plastic model considerations past this point. In contrast, the kinematic hardening model restricts this growth and therefore does not require an elastic perfectly-plastic assumption in order for the growth of the yield surface to be constrained. This means the effects of strain hardening can still be seen at higher strain levels, as shown by the post-yield stiffness present at all displacement amplitudes in Figure 42 and Figure 43. In reality, the response of a metal to cyclic deformation is a combination of these two types of hardening.

This phenomenon of combined hardening is seen by looking at the behavior of the experimental specimen in Figure 42. In the initial stages of cyclic displacement, the size of the experimental yield surface grows. This is clearly seen in the tensile portion of the displacement amplitudes at 0.065 inches and 0.13 inches. At both of these amplitudes, the value of the axial force capacity increases from the first to the second cycle of the same amplitude. After these cycles, the increase in axial force capacity from the first to second cycle is less dramatic and eventually is no longer visible. The disappearance of this growth in axial capacity for cycles at the same displacement amplitude indicates the material has reached a point that defines saturation of yield surface growth and is now deforming in a manner consistent with the kinematic hardening model. Therefore, it is plausible that a combined hardening model will more adequately describe the force-displacement behavior of the yielding plate under cyclic load demands.

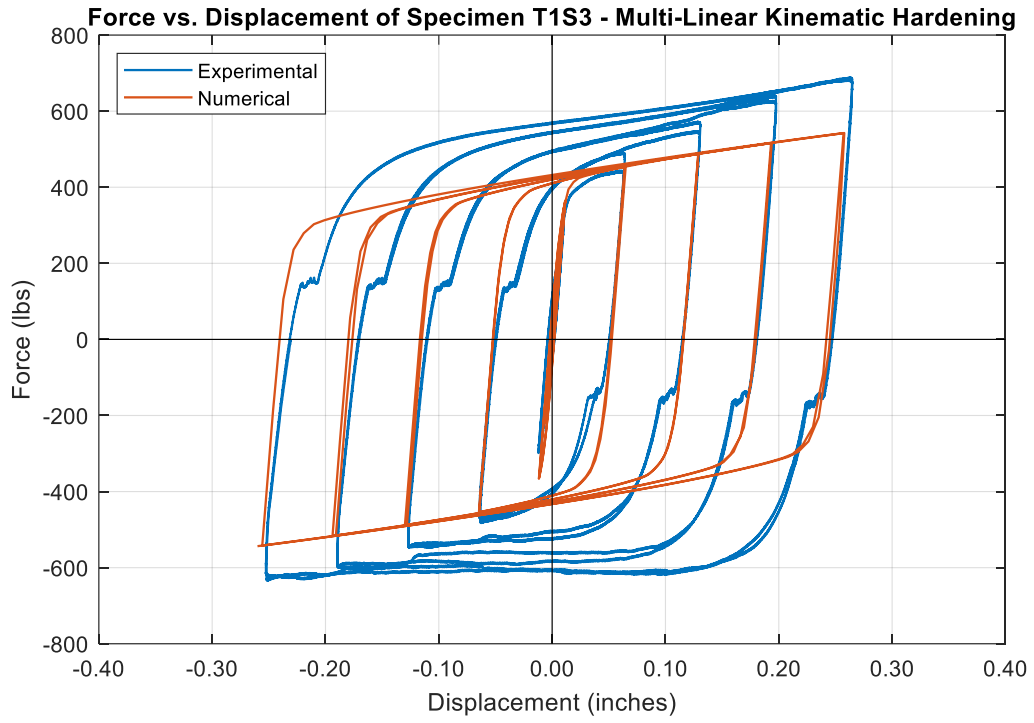


Figure 43. Multilinear kinematic hardening model.

6.2 Combined Isotropic and Kinematic Hardening

Based on the results presented, it is obvious that neither the isotropic hardening model nor the kinematic hardening model provide adequate representations of the hysteretic behavior of the yielding plate. It was therefore necessary to determine an adequate combined hardening model. The best way to define a combined hardening model is using cyclic test data; however, cyclic data of the form necessary is not accessible. In order to use cyclic data to define a combined hardening model, it would be necessary to obtain cyclic stress and strain data from a coupon test. The only cyclic data available is the cyclic force and displacement readings from the BRB component testing. While useful for analysis of hysteretic behavior, this type of cyclic data does not provide stress-strain behavior, nor is it feasible to process the data in order to obtain this stress-strain behavior due to the complex geometry of the yielding plate. In lieu of cyclic coupon tests, the literature has suggested that mild metals may be adequately defined by a combined hardening model using 50% isotropic hardening and 50% kinematic hardening (Hu et al. 2016; Jia and Kuwamura 2014; Xiang et al. 2017).

The hardening model chosen is the Chaboche model with nonlinear isotropic hardening. This model is easily input in ABAQUS using the “combined model” with multiple backstresses and manual calibration of cyclic hardening parameters. The necessary parameters for kinematic hardening are calibrated in ABAQUS using tabular true stress-true strain data points from the original coupon testing. Multiple backstresses provides differing kinematic hardening relationships at different levels of plastic strain. For low plastic strain, the movement of the center of the yield surface is governed by a nonlinear function of equivalent plastic strain. At high plastic strains, the translation of the center of the yield surface is governed by a linear hardening law. This is visualized in Figure 44 where three backstresses are shown. The total backstress is determined by superimposing all of the defining backstress laws at each value of equivalent plastic strain. Including multiple backstresses in this manner provides a more accurate estimation of the actual hardening characteristics of the material at multiple strain levels. ABAQUS incorporates this hardening law implicitly in the combined material definition when tabular data points are used as input.

To add the isotropic hardening component to the model, the “cyclic hardening” suboption is chosen in ABAQUS and the calibrated material parameters are input. These parameters include the equivalent stress at which hardening begins (i.e. the true yield stress), the maximum radius of the yield surface (Q_∞), and the exponential material hardening parameter (b). The calibration of these parameters is performed following the procedures outlined in literature (Gong et al. 2010; Jia and Kuwamura 2014).

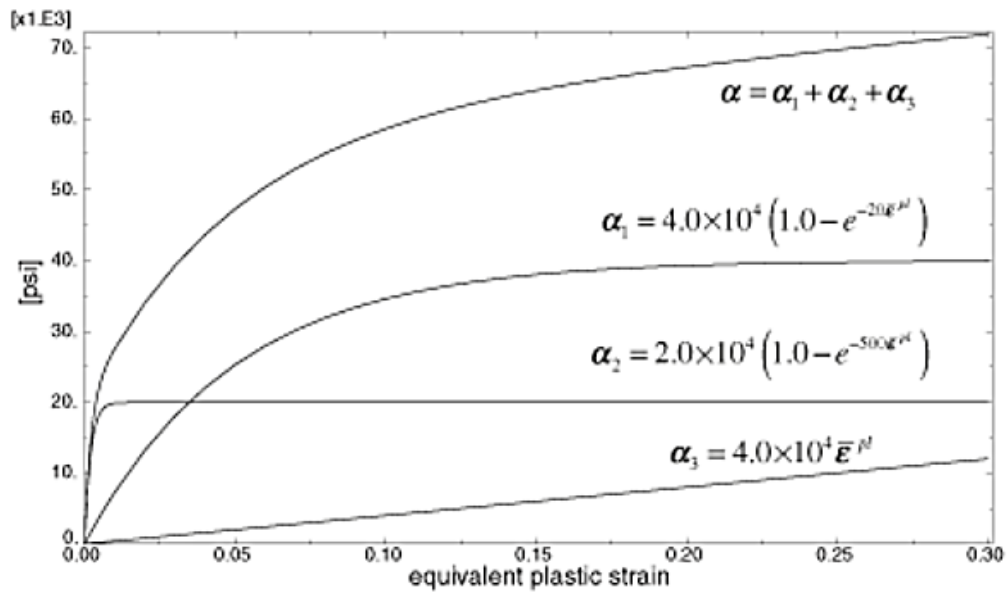


Figure 44. Graphical representation of multiple backstresses defining kinematic hardening component.

Reproduced from (Dassault Systèmes Simulia Corp. 2010).

This hardening model assumes a growth of the yield surface that follows the evolution rule:

$$dR = b(Q_\infty - R)d\varepsilon_{eq} \quad (6.1)$$

Differentiating equation (6.1) with respect to time, the size of the yield surface can be defined for a uniaxial state as:

$$R = Q_\infty \left(1 - e^{-b\varepsilon_{eq}}\right) \quad (6.2)$$

Considering the assumption that the isotropic component of hardening is constrained to 50% of the total hardening, the maximum growth of the yield surface is defined as:

$$Q_\infty = \frac{\sigma_{mono} - \sigma_{y0}}{2} \quad (6.3)$$

Figure 45 provides a visualization of the variables used in the definition of Q_∞ . The value of σ_{mono} should be defined such that the calculated parameters model the necessary strain range as accurately as possible. Similar to the definition of the hardening modulus, the value of σ_{mono} is chosen by the analyst. A higher value will allow the yield surface to grow more prior to saturation, while a lower value will limit the isotropic growth of the yield surface to a lower value. In the case of this design, the best value to choose for σ_{mono} is not well defined due to the lack of a uniform average strain at high displacement amplitudes. Because of this, the average maximum strain shown previously in Figure 41 was chosen as a reasonable strain range in which to focus the calibration of hardening parameters. Therefore, σ_{mono} was set equal to the true stress at a strain of $\varepsilon_{pl} \approx 0.10$. The hardening parameter, b , must then be calibrated from a known point prior to σ_{mono} . This point is taken as a point at approximately half the maximum considered plastic strain. The hardening parameter can then be calculated as:

$$b = \frac{\ln\left(1 - R/Q_\infty\right)}{\varepsilon_{eq}} \quad (6.4)$$

Because the data is from a monotonic tension test, the equivalent plastic strain is equal to the measured plastic strain in the axial direction. The simplified tabular input for defining backstresses and a graphical representation of these tabulated values is shown in Table 15 and Figure 46. The calibrated material parameters for the isotropic hardening component are shown in Table 16. The ABAQUS results of the combined hardening model is shown in conjunction with test results from T1S3 in Figure 47. Again, it is acknowledged that the strain levels at certain points within the yielding plate may exceed the final plastic strain of 0.1002 input in the tabular data. However, this will not drastically affect results for two reasons. First, the overall average maximum strain in the high strain regions of the yielding ring is approximately half the maximum strain recorded for any individual element, as shown in Figure 41. This is a reflection of strain concentrations at the location of ring connection to the overall device. Secondly, as discussed

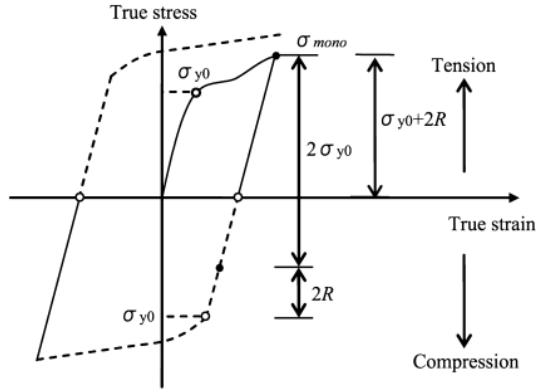


Figure 45. Visualization of parameters for isotropic hardening calibration.

Reproduced from (Jia and Kuwamura 2014).

Table 15. Simplified stress-strain tabular input for kinematic hardening calibration.

True Stress (psi)	True Strain
34,200	0.0000
36,200	0.0193
44,996	0.0546
51,695	0.1002

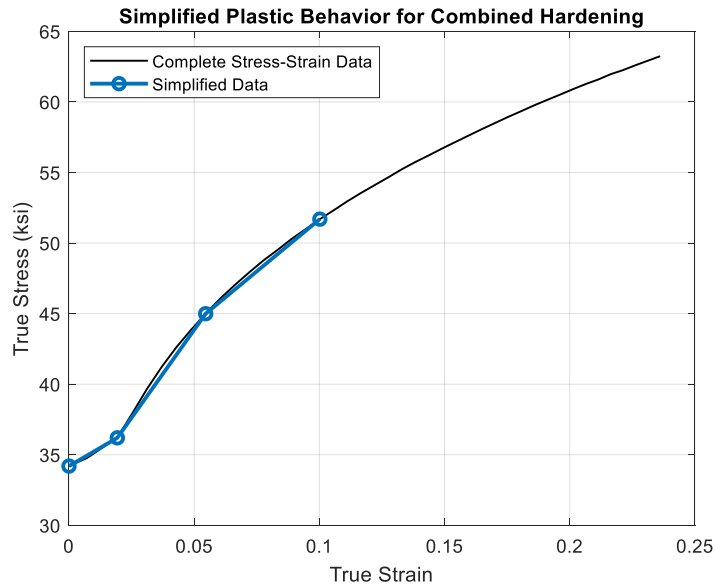


Figure 46. Simplified stress-strain data for ABAQUS model.

Table 16. Isotropic hardening parameters.

σ_{y0} (psi)	σ_{mono} (psi)	Q_{∞} (psi)	b
34,200	51,695	8,747	17.58

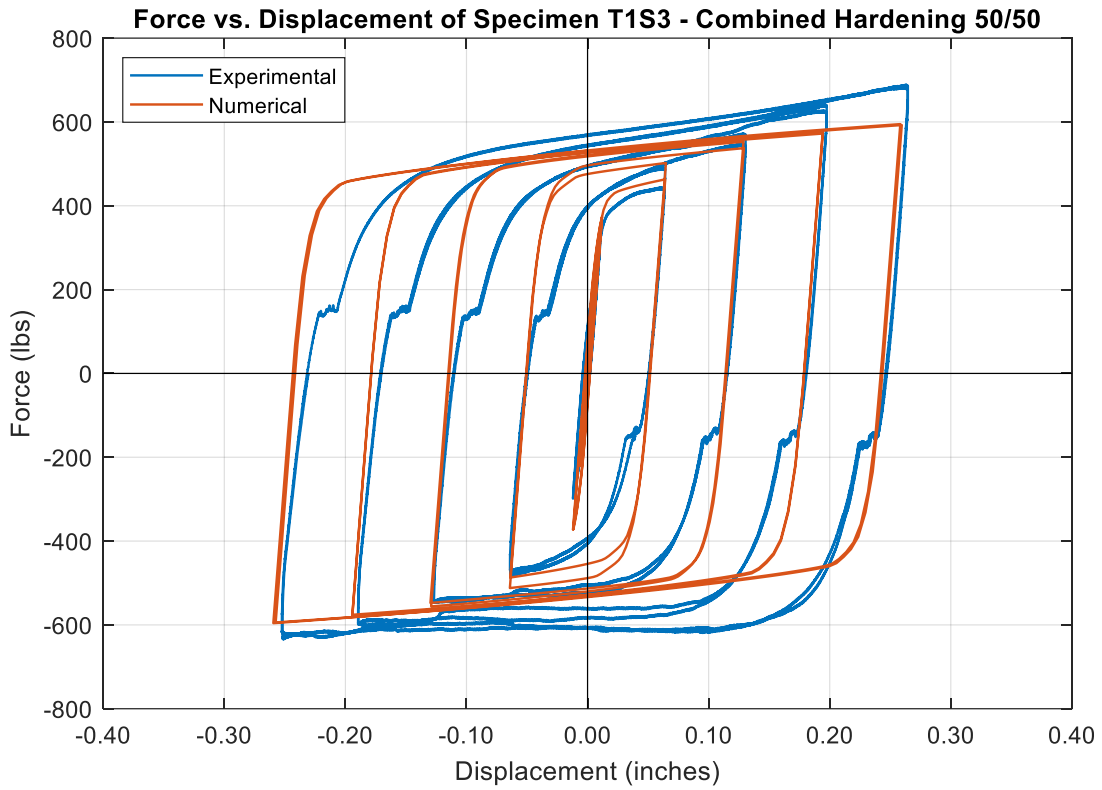


Figure 47. Combined hardening model.

previously, the linear hardening law is retained in ABAQUS at high strain levels, thus still providing an adequate estimate of hardening at strains slightly past 0.1002.

There are still inconsistencies between the behavior of the numerical model and the experimental model. Of particular interest is the discrepancy between the estimated behavior in extreme tension and the actual behavior in extreme tension. Despite this flaw, the combined hardening model provides significant improvement over the previous hardening models when considering the behavior of the specimen at large displacement levels. There is neither a gross overestimate nor a gross underestimate of the force levels as was previously seen. There is an overestimate of the initial compressive behavior just after yield. This is attributed to the exponential isotropic hardening behavior assumed in ABAQUS that overestimates the amount of isotropic hardening at some strain levels and underestimates at other strain levels. There is also potential that the tension and compression behavior is not symmetric. However, considerations of asymmetry in hardening are beyond the scope of this thesis. While the behavior of this model is not ideal, it is still reasonable, so the combined model is determined as the most accurate hardening model to use in future analyses.

6.3 Nonlinear Geometric Effects

The material nonlinearity is accounted for in the nonlinear combined hardening model previously discussed. However, the hardening model alone does not account for the increased tensile force capacity observed at high displacements. This phenomenon is attributed to large deformation effects that cause the specimen to be dominated by tensile stresses at large displacements as opposed to the bending stresses that control at smaller displacements. This behavior is seen clearly when the deformed shape at maximum compression is contrasted to the deformed shape at maximum tension in Figure 48. When experiencing the maximum tensile deformation, the source of plasticity in the yielding plate is a combination of flexural bending stress and axial stress across the top and bottom portions of the ring. The resistance capacity of the section is therefore increased at high tensile displacements because the axial resistance capacity is greater than the flexural resistance capacity. At high compressive deformation, flexural bending stresses dominate the plastic response in the section. This difference in plastic mechanism causes the axial force capacity at maximum compression to be much lower than the axial force capacity at maximum tension.

This behavior was not previously accounted for because the effect of nonlinear geometry was not included in the ABAQUS analysis. If there are any large strains or large deformations expected, the nonlinear geometry effects must be toggled to “on” in the step definition. Once this was done and the analysis re-run,

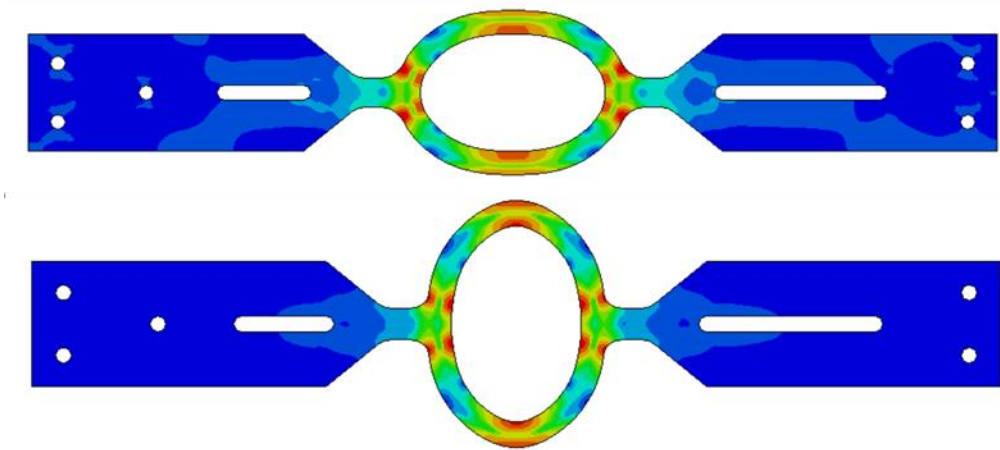


Figure 48. Deformed shape in tension (top) and compression (bottom). Showing contours for von Mises stress.

the effect of this increased capacity was clearly seen, as shown in Figure 49. This figure shows that the extreme deformation behavior at both tension and compression is matched well by the new numerical model for specimen T2S4. The tensile behavior of specimen T1S3 is also adequately captured. However, there are still inconsistencies in the comparison of the numerical and experimental results. The compression capacity of specimen T1S3 is not well captured. There is disagreement between the experimental compressive force capacity for specimen T1S3 and T2S4 at low displacement amplitudes. This leads to an overestimate of compressive capacity for specimen T2S4 at low displacement amplitudes, while the estimation is fairly accurate for specimen T1S3. Because there is a limited amount of experimental data, it is unknown which compressive behavior more accurately represents the average force capacity. Therefore, this potential error is not feasibly corrected and is rather accepted. The numerical model also begins to yield sooner than the experimental results show, especially on the tension side. These discrepancies show that this is not a perfect model. However, there are good aspects of this model that make it an acceptable model to use in following tests. First, the transition from the elastic region to the plastic region is well matched. This transition is not an exact match, but as discussed previously, this is likely due to manufacturing tolerances. This is the most important portion of the curve for designing a BRB with the correct yield force and elastic stiffness. The model also captures the overall behavior well and identifies the possibility of asymmetry in the hysteresis. This is of high importance for future iterations of this device because the goal of this work is to produce a device with a hysteretic curve that matches the form of the prototype BRB, which usually has a high degree of symmetry.

While the hardening model is not a perfect fit and the nonlinear geometric effects included in ABAQUS do not match the exact experimental results, the conclusion is that the proposed improvements to the numerical model are accurate enough in the areas that matter for this project that it will be beneficial for use in continued analyses. The focus of this stage of numerical updating is not on obtaining a numerical model that provides a highly accurate description of device behavior at all displacement levels. Rather, the goal at this phase in the project was to identify a geometric configuration of a yielding mechanism that can replicate the scaled parameter values of its prototype counterpart while still providing a symmetric hysteretic curve. This updated numerical model is useful in moving forward with the next phase in this project because it provides an adequate picture of the overall force-displacement behavior, as well as an accurate estimation of initial elastic properties of the model BRB. This numerical model will therefore be used to perform FE analyses of other brace shapes to determine if there is a different configuration of the physical yielding device that will perform in a manner more similar to that of the prototype BRB.

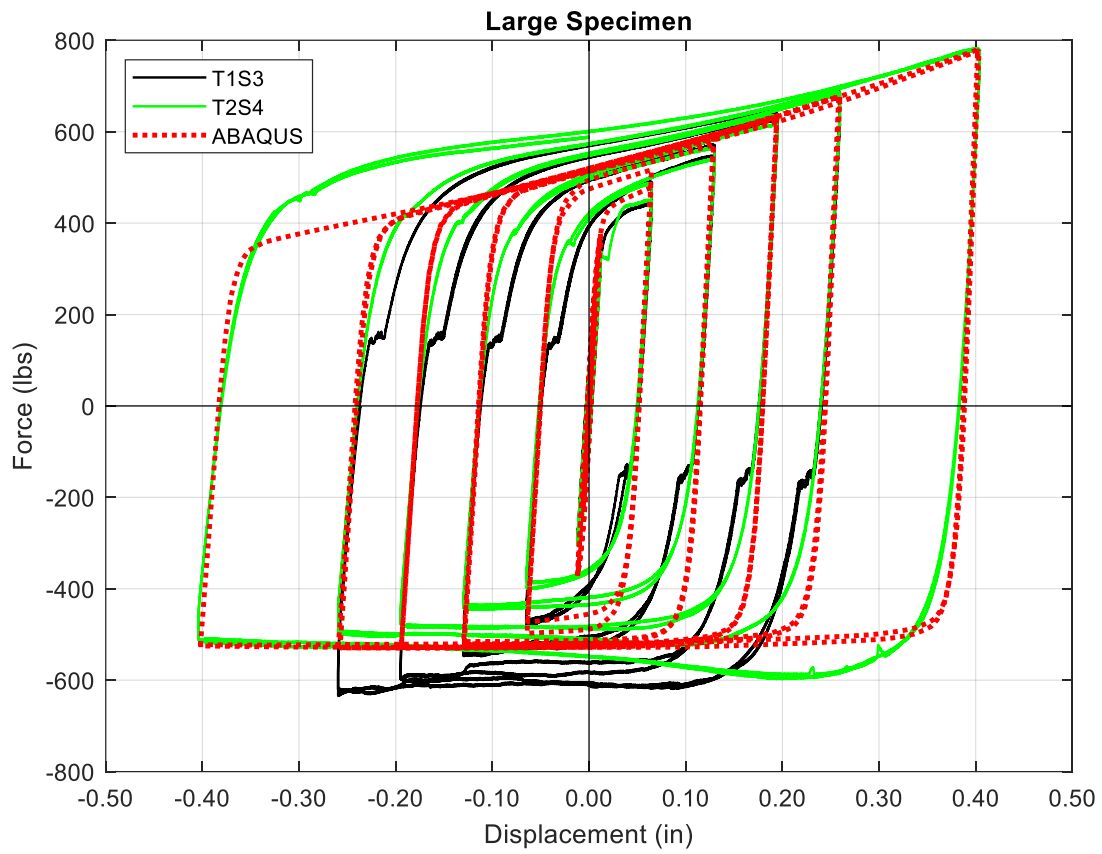


Figure 49. Analytical hysteretic curves including nonlinear geometric effects vs. experimental results.

Chapter 7

7 Updated Model: The Rectangle-Type BRB

Experimental results from chapter 5 and improved FE results from chapter 6 conclusively show that the initial design was inadequate for modeling BRB hysteresis at a large range of displacement values. While this means the initial model was not as successful as anticipated, these results still provided valuable insight into the proper design of a small-scale BRB counterpart. Building from this, the strengths of the original beam-type and ring-type design were combined to form the new rectangle-type BRB. Based on initial FE analyses using the improved material model and nonlinear geometric effects previously discussed, this new design was predicted to behave in a way similar to that of the large-scale BRB, as desired. Initial experimental results provide further proof of desirable performance of this new mechanism.

7.1 Conceptual and Physical Design

7.1.1 Targeted Improvements

There are several targeted improvement goals for the new design of the small-scale BRB. The first and most imperative of these improvements is to mitigate the increased tensile capacity identified in the ring-type specimen. A promising way to do this would be to force the deformed shape of the device to be similar in extreme compression as compared to extreme tension. This will encourage a similar mechanism of plastic deformation that will effectively lead to similar axial force capacities in both tension and compression. This is a strength of the previous beam-type mechanism discussed at the beginning of chapter 3. Recall Figure 11 from chapter 3, which shows the conceptual model initially used in the beam-type formulation of predictive equations. As opposed to the ring-type mechanism, which deforms into an oval of varying degree depending on whether displacement is tensile or compressive, the bending beam will have a similar deformed shape at all instances due to the high stiffness at the connections (previously idealized as fixed connections with infinite stiffness).

Another concern was that of the small-scale BRB geometrically fitting in the frame bay. This concern is mitigated by taking advantage of the strength of the ring-type BRB model. As previously shown in Table 6, the ring-type model was expected to have a diameter much smaller than the length of the beam-type model. This can be attributed to the ring having a higher percentage of the central geometry experiencing high moment demands as opposed to the beam. A higher portion of the part yielding allows the ring-type

design to perform at the relatively low yield force and elastic stiffness required while still maintaining a compact geometric configuration. The rectangle-type device effectively utilizes two bending beams as opposed to the single bending beam used previously in the beam-type model. This increases the portion of the central yielding mechanism that is expected to dissipate energy. This increase in available yielding area should decrease the overall beam length as compared to the original beam-type model. Therefore, the rectangle-type BRB should have no issue fitting in the allowable space in the frame bay.

Lastly, there was concern surrounding the manufacturing tolerance levels that affect the accuracy of the experimental parameters, as shown in chapter 5. One of the main issues is the percent error that may be attained if the part is nominally thin. The waterjet tolerance is an absolute measurement, so the larger the nominal width, the smaller the percent error in actual elastic stiffness, yield force, and yield displacement values. As previously documented in Table 6, the beam-type model produced larger required widths to fit the scaled parameterized BRB. While these predictive equations have been shown to be inaccurate due to modeling simplifications, it is still reasonable to expect that the use of a beam bending mechanism may increase the required part yielding width and therefore aid in reducing percent error due to manufacturing tolerances.

7.1.2 Conceptual Validation

Prior to performing any in-depth calculations, a cyclic analysis of the new rectangle-type design was performed in ABAQUS using the updated material model and including nonlinear geometric effects. This was a simple check to ensure there did not seem to be any excessive tensile or compressive capacity as seen in the previous ring-type model. Shown in Figure 50 is the hysteretic curve for a yielding plate with the rectangle-type geometry shown in Figure 51. The values of L and b are not calibrated to provide any goal elastic stiffness or yielding force values. This test was simply done to ensure the new design provided a symmetric hysteretic curve at large displacements. Since the hysteretic curve had the correct form, the design then proceeded to the next phase – calibration of the geometric parameters to obtain the proper elastic stiffness and yielding force required for the scaled specimen.

7.2 Parameter Calibration

In order to efficiently design the physical BRB to the dimensions necessary, it was vital that the predictive equations be more accurate than they were for the initial specimen. While a more detailed conceptual model would provide a better estimation of important parameters, even this is not accurate enough to exactly estimate required geometry for the BRB due to stresses and strains not being completely confined to the

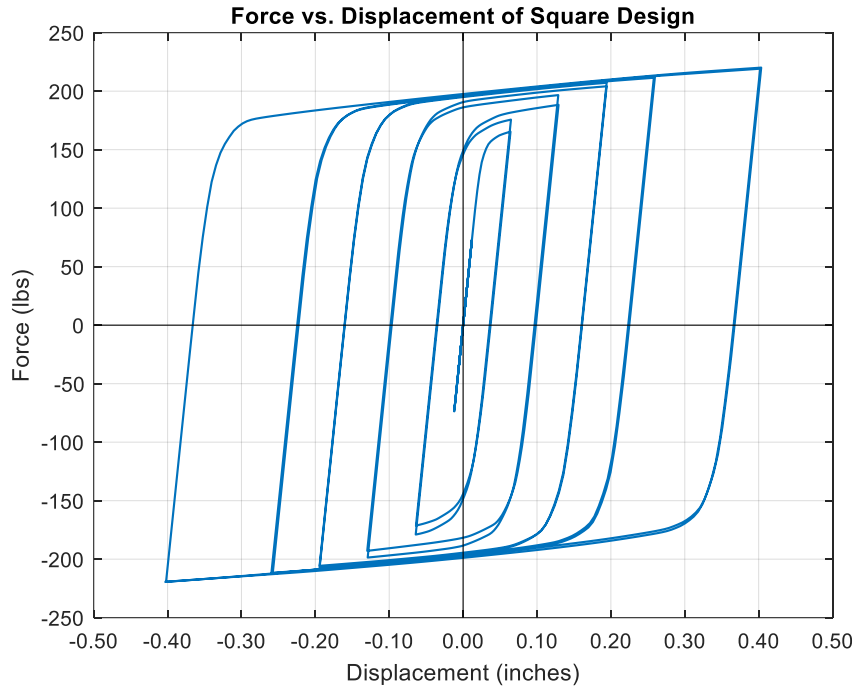


Figure 50. Force vs. displacement of square specimen using improved numerical model.

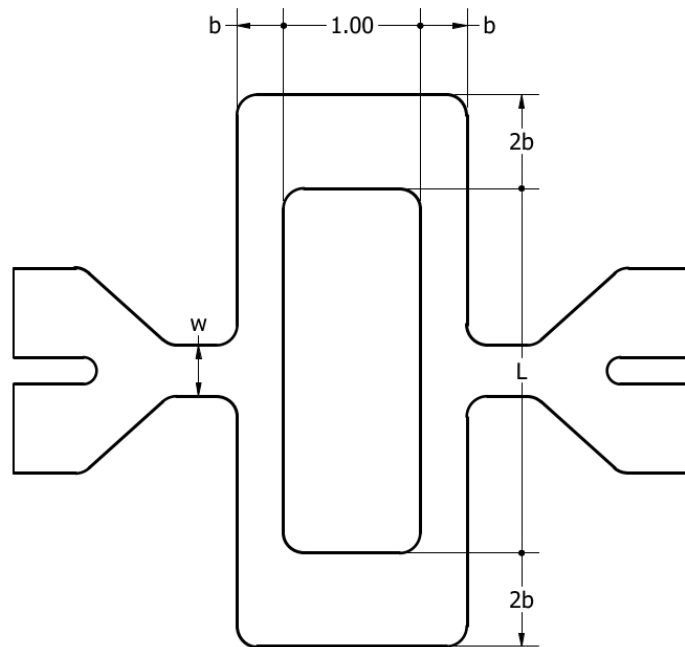


Figure 51. Physical rectangle-type device labeled with important design parameters. Only central yielding square shown for clarity of dimensions.

central square. While stresses will be concentrated in this area, the geometry of the entire plate is expected to somewhat impact the actual strength and stiffness. Therefore, a different approach was designed to accurately predict the elastic stiffness and yield force based on the length (L) and width (b) of the rectangle-type BRB. These parameters are defined visually in Figure 51. The progression of work is as follows:

- Define the form of an empirical equation to predict elastic stiffness and yielding force of the device.
- Perform numerical monotonic tension tests in ABAQUS on a suite of training values for L and b . Determine the elastic stiffness, yield strength, and yield displacement for all tests.
- Perform a nonlinear regression analysis using MATLAB to determine the values of all unknown constants in the predictive equations.
- Calculate elastic stiffness and yielding force of the training data set using the predictive equations. Determine the percent error in the equations to examine the fit of the model.
- Analyze the effectiveness of the predictive equations on a test set with different connecting widths.
- Analyze the effectiveness of the predictive equations on a test set with values for L and b both smaller and larger than the extents of the training set.
- Make any corrections necessary based on test set results.
- Use the predictive equations to solve for required b and L for a small and large BRB. Evaluate this geometry in ABAQUS to determine adequacy of the predictive equations for future use.

These steps are followed and the results presented in the subsequent sections.

7.2.1 The Initial Form of the Empirical Equations

The first and most critical step is defining the proper form of the empirical equations for elastic stiffness and yielding force. The final form of the empirical equations is presented below, followed by a qualitative discussion of the logical reasoning that led to this particular format.

$$P_y = (C_1 + C_2\alpha) \left[\frac{F_y d [(1 + C_3\beta)b]^2}{[(1 + C_4\beta)L_{\text{eff}}]} \right] \quad (7.1)$$

$$K = (C_5 + C_6\alpha) \left[\frac{Ed [(1 + C_7\beta)b]^3}{[(1 + C_8\beta)L_{\text{eff}}]^3} \right] \quad (7.2)$$

Where:

K = elastic stiffness

P_y = yielding force

$C_1 - C_8$ = constants to be determined using regression analysis

w = length of connecting portion

b = width of bending beam

L = length of bending beam

$L_{\text{eff}} = L - w$ = effective length of bending beam

d = thickness of yielding plate

E = Young's modulus of the plate material

F_y = yielding stress of the plate material

$$\alpha = \frac{w}{L}$$

$$\beta = \frac{b}{L_{\text{eff}}}$$

7.2.2 Qualitative Basis for Predictive Equations

A combination of basic mechanics, qualitative analysis of part behavior, and quantitative contour diagrams from ABAQUS analyses provide logical proof for the form of the predictive equations. First, consider the known equations that govern the moment and deflection at midspan of beams subject to certain loading patterns and support conditions, as presented in Table 17. These equations are derived from basic mechanics and are known to accurately describe the midspan deflections and moments of the beams shown. While there are different support and loading conditions for each case, the form of the deflection equation and moment equation is similar. If the total load for cases 2 and 4 is considered to be $P = p_0L$, the deflection and moment at midspan for each case can be described by the equations below, with A_1 and B_1 representing a multiplier specific to the loading and support conditions present.

$$\Delta_{\text{mid}} = A_1 \frac{PL^3}{EI} \quad (7.3)$$

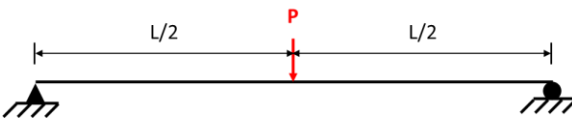
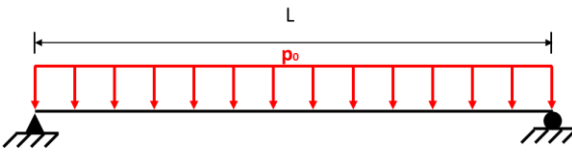
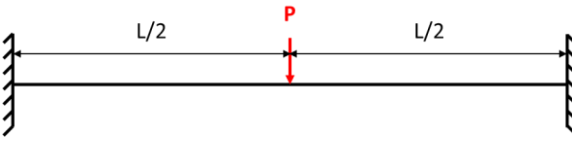
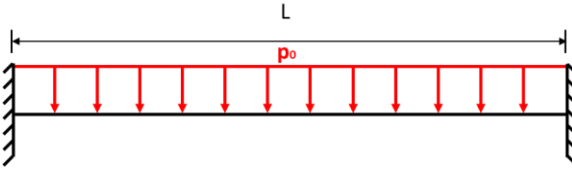
$$M_{\text{mid}} = B_1 PL \quad (7.4)$$

Substituting $I = \frac{1}{12} db^3$ into equations (7.3) and (7.4), the deflection equation can then be rearranged to

produce a bending stiffness. The constant A_2 represents a new coefficient value.

$$K = A_2 \frac{Edb^3}{L^3} \quad (7.5)$$

Table 17. Midspan deflection and moment for different support and loading conditions.

Case	Support & Loading Condition	Deflection at Midspan	Moment at Midspan
1		$\Delta_{\text{mid}} = \frac{PL^3}{48EI}$	$M_{\text{mid}} = \frac{PL}{4}$
2		$\Delta_{\text{mid}} = \frac{5p_0L^4}{384EI}$	$M_{\text{mid}} = \frac{p_0L^2}{8}$
3		$\Delta_{\text{mid}} = \frac{PL^3}{192EI}$	$M_{\text{mid}} = \frac{PL}{8}$
4		$\Delta_{\text{mid}} = \frac{p_0L^4}{384EI}$	$M_{\text{mid}} = \frac{p_0L^2}{24}$

Using the same derivation described in chapter 3 to determine the force at which plastic moment is achieved, the midspan moment equation can be used to form an expression for the yielding force of the beam, with B_2 representing a new coefficient value.

$$P_y = B_2 \frac{F_y db^2}{L} \quad (7.6)$$

It can therefore be deduced that for the four cases presented in Table 17, the elastic stiffness of the beam is dependent upon the material's elastic modulus, beam width, beam thickness, and beam length. The yielding force is dependent upon the material yield stress, beam width, beam thickness, and beam length. These dependencies are reflected in the formulation of the predictive equations. However, the actual loading conditions, support conditions, and geometric parameters of the rectangle-type yielding plate are more complex than the simple loading cases and support conditions presented in Table 17. The beam ends are neither pinned nor fixed. Rather, they have some rotational stiffness provided by the top and bottom of the central square. Due to the special design of these top and bottom members, the relative stiffness of the bending beam as compared to the support members remains constant for all beam widths. This encourages the “support conditions” of the beam to act in a similar manner for all sizes of BRBs and will therefore aid in forming more accurate predictive equations.

However, the deflected shape of the beam may still change as the width changes due to the stiffened central portion of the beam at the connection location. The equations in Table 17 account for a uniform cross-section along the entire length of the beam. This is not the case. Not only is the load distributed across the connecting length, w , but this connection itself provides increased stiffness to the beam at that location by effectively increasing the width of the beam. This increase in stiffness at the center of the bending portion of the beam will affect both the maximum deformation and the distribution of stresses. This is clearly seen when comparing Figure 52 and Figure 53, which represent two very different stiffness values. Let us first compare the x-direction stress distribution. Figure 52 clearly shows bending stress in the top and bottom of the central square with a maximum stress of 33.4 ksi. There is negligible tensile stress in the connecting portions of the yielding plate. Figure 53 also shows appreciable bending stress in the top and bottom of the central square with a maximum stress of 36.8 ksi. However, in contrast to Figure 52, Figure 53 also shows high tensile stresses across the connecting length. These tensile stresses are at an average value of approximately 20 ksi, which is significant in magnitude. Now, let us shift focus to the y-direction stress distribution. Both figures show bending stresses distributed at predicted locations along the bending beam – at the connections and in the center. Both of these locations are expected to have high moment and therefore should experience high bending stress. Figure 52 shows an intersection of extreme compressive

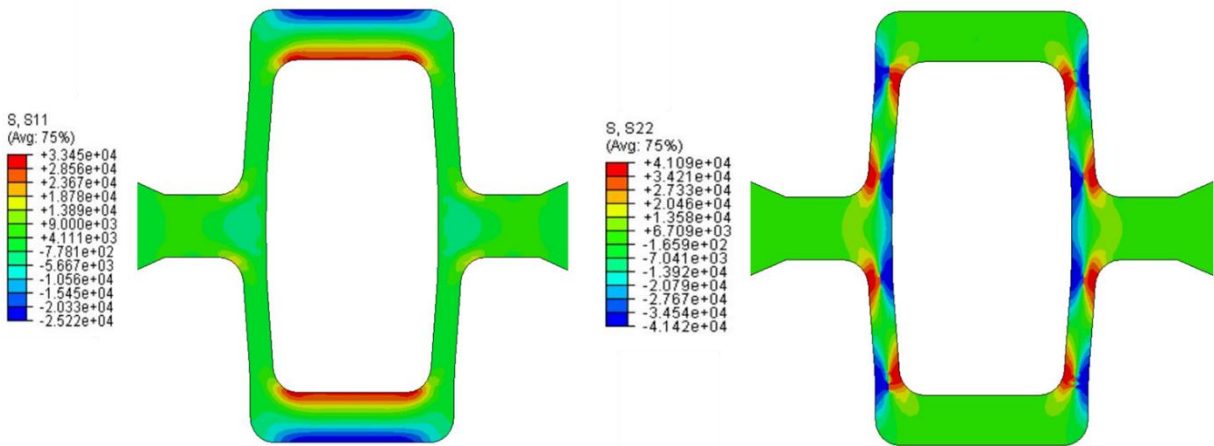


Figure 52. Comparison of x- (left) and y-direction (right) stresses for $L = 2.00$ in. and $b = 0.15$ in. Stress in psi.

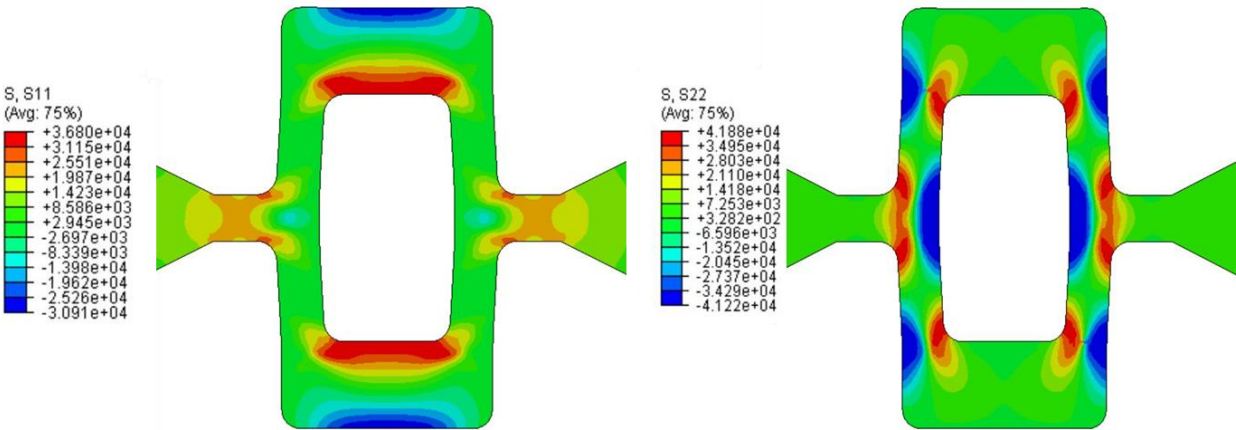


Figure 53. Comparison of x- (left) and y-direction (right) stresses for $L = 2.00$ in. and $b = 0.35$ in. Stress in psi.

and extreme tensile stress at the locations of maximum bending, which implies the plastic moment capacity of the beam is well utilized. In contrast, Figure 53 shows a larger distribution of high stress areas and no intersection of extreme tensile and compressive stress across the bending plane. This suggests that plasticity is not as concentrated in the specimen with higher stiffness and the assumption of plastic moment capacity defining the onset of overall device yielding may not be as accurate.

A third consideration in the formulation of the predictive equations was that the connection length, w , was set to be 0.375 inches for all sizes of model BRB. This affects the stress distribution, as discussed previously, but this also affects the deformation due to the percentage of the beam length that is loaded. In the case of a short beam length, more of the beam is loaded with a distributed axial load than if the overall beam length is larger. This will affect both the elastic stiffness and the yield force. If a greater percentage of the beam is loaded, both the midspan deflection and midspan moment decrease. This corresponds to an increase in both elastic stiffness and yield force. Therefore, this parameter must be accounted for in the final formulation of the predictive equation.

After considering all of these influential factors, the form of the predictive equation was finalized. The use of L_{eff} as the main length parameter is justified by the fact that the actual bending portion of the beam is the portion which is not stiffened by the connection. Therefore, calculation of moment and deflection should account for only effective bending length. There are three distinct factors that effectively describe the behavior of the yielding mechanism of the rectangle-type BRB: a constant, a “load distribution” factor, and a “stiffness correction” factor. The first constant simply reflects the base yielding force and elastic stiffness of the mechanism. The other two constants are more complex.

The “load distribution” factor reflects the constant value of w combined with the changing value of L . As previously shown in Table 17, the overall maximum deflection and midspan moment both decrease with an increase in the load distribution if considering the total resultant load to remain unchanged. Therefore, this factor either raises or lowers the base value of strength and stiffness to account for a greater or lesser load distribution.

The “stiffness correction” factor reflects the previous qualitative discussion of the stress distribution within the beam as a variation of relative stiffness. A shorter beam length combined with a larger beam width increases the stiffness of the bending portions of the beam and thus increases the tensile (or compressive) force in the connecting portion of the yielding plate and more evenly distributes the plastic response of the beam over more of the beam length. Conversely, a combination of a long length and small width decreases

the stiffness of the bending portion of the beam, thus decreasing the amount of stress concentrated in the connecting portion of the yielding plate and intensifying the concentration of plasticity to specific plastic hinge locations within the beam. Applying this stiffness correction factor to the width and effective length individually allowed the regression analysis more flexibility to provide a more accurate fit of the training data.

7.2.3 Suite of ABAQUS Analyses

The suite of training data used to initially fit the empirical equations needed to be composed of enough tests that the behavior of the device over a range of elastic stiffnesses and yield forces could be thoroughly investigated. However, it was also important that this training data did not include outliers representing a combination of parameters unlikely to be used in the BRB analog, as the inclusion of such outliers would ultimately reduce equation accuracy. After analyzing a few initial rectangle-type plates, the lower and upper bounds of length were set to 2.00 and 3.00 inches, respectively. The lower and upper bounds for width were set to 0.15 and 0.45 inches, respectively. A list of all 24 training tests is presented in Table 18. The same procedure described in chapter 4 and graphically shown in Figure 18 for determining elastic stiffness, yield force, and yield displacement was followed for each test. Following the mesh refinement study previously conducted for the ring-type yielding plate, 8 CPS4R elements across the bending width were used for each ABAQUS analysis, along with the same material model and simplified boundary conditions previously discussed.

7.2.4 Results of Regression Analysis

Using the suite of specimen geometries, calculated elastic stiffnesses, yield forces, and yield displacements, MATLAB nonlinear regression capabilities were used to determine the constants C_1 - C_8 . Placing these constants in their appropriate places in equations (7.1) and (7.2), the predictive equations as solved by the regression analysis are seen below, with variables defined in the same manner as previous.

$$P_y = (2.011 + 6.432\alpha) \left[\frac{F_y d [(1 - 0.847\beta)b]^2}{[(1 - 0.847\beta)L_{eff}]^2} \right] \quad (7.7)$$

$$K = (11.030 - 2.579\alpha) \left[\frac{Ed [(1 - 0.487\beta)b]^3}{[(1 + 2.561\beta)L_{eff}]^3} \right] \quad (7.8)$$

While it is not possible to obtain a simple closed form solution for the yield force and elastic stiffness to validate the constants found via linear regression, it is important to qualitatively inspect the equations for any notable flaws. One noticeable disagreement between the previous qualitative discussion and the final solution is the negative value of C_6 . Previously, it was discussed that a higher percentage of a beam being

Table 18. Training data for empirical equations.

Test Number	L (in)	b (in)	w (in)	K (lb/in)	P _y (lb)	δ _y (in)	PE, K (%)	PE, P _y (%)	PE, δ _y (%)
1	2.00	0.15	0.375	12,674	159	0.0125	-3.76	-2.55	1.26
2	2.00	0.20	0.375	23,225	271	0.0117	-1.37	-1.59	-0.22
3	2.00	0.25	0.375	35,784	407	0.0114	0.06	-0.64	-0.70
4	2.25	0.15	0.375	9,001	130	0.0145	-2.38	-0.26	2.17
5	2.25	0.20	0.375	17,080	226	0.0132	-0.79	-0.35	0.44
6	2.25	0.25	0.375	27,171	343	0.0126	-0.08	-0.07	0.01
7	2.25	0.30	0.375	50,827	635	0.0125	0.69	0.55	-0.15
8	2.50	0.15	0.375	6,582	111	0.0168	-0.77	0.67	1.45
9	2.50	0.20	0.375	12,844	193	0.0150	0.17	0.46	0.29
10	2.50	0.25	0.375	20,949	295	0.0141	0.34	0.35	0.00
11	2.50	0.30	0.375	30,470	416	0.0137	0.32	0.26	-0.06
12	2.50	0.35	0.375	41,006	553	0.0135	0.16	0.34	0.18
13	2.50	0.40	0.375	52,095	708	0.0136	0.07	0.12	0.04
14	2.50	0.45	0.375	63,339	874	0.0138	0.10	0.13	0.03
15	2.75	0.25	0.375	16,387	258	0.0158	1.19	0.82	-0.36
16	2.75	0.30	0.375	24,285	366	0.0151	0.81	0.56	-0.24
17	2.75	0.35	0.375	33,297	490	0.0147	0.21	0.15	-0.06
18	2.75	0.40	0.375	43,048	628	0.0146	-0.26	-0.14	0.12
19	2.75	0.45	0.375	53,177	780	0.0147	-0.52	-0.22	0.30
20	3.00	0.25	0.375	13,009	229	0.0176	2.20	1.04	-1.14
21	3.00	0.30	0.375	19,607	326	0.0166	1.39	0.55	-0.83
22	3.00	0.35	0.375	27,276	437	0.0160	0.54	0.22	-0.32
23	3.00	0.40	0.375	35,773	564	0.0158	-0.23	-0.35	-0.13
24	3.00	0.45	0.375	44,805	702	0.0157	-0.77	-0.58	0.19

loaded corresponds to a higher stiffness value. Intuitively, it then follows that the factor multiplying α should be positive. However, upon further inspection, the negative value does not disqualify the solution. While α is the factor representing the “load distribution” factor, this is not the only portion of the equation accounting for the connecting width. The width of the connecting portion is also implicitly included in the “stiffness correction” factor because the magnitude of w directly impacts the magnitude of L_{eff} , which in turn directly impacts β . This complexity means that the calculation of C_6 is not straightforward and therefore supports the integrity of the negative constant value.

Although qualitative understanding is important, quantitative proof is also useful in validating the final form of equations (7.7) and (7.8). Consider a rectangle-type BRB defined by the length, $L = 2.50$ inches and $b = 0.30$ inches. Now, consider one situation in which the connecting width, w , is 0.375 inches and a second situation in which the connecting width 0.400 inches. Because the larger connecting width both increases the load distribution factor and decreases the effective bending length, the overall elastic stiffness should be higher for this case. Using equations (7.7) and (7.8), we do indeed find this to be the case. In the first case, the yield force and elastic stiffness are calculated as 417 lbs. and 30,566 lb./in., respectively. In the second case, these values are calculated as 431 lbs. and 31,214 lb./in. This quantifiable increase, while not yet verified as accurate, does prove that the equation itself does produce a higher yield force and higher elastic stiffness value for a greater connecting width. This makes physical sense, so the regression analysis is considered trustworthy.

Table 18 shows the parameter values calculated using numerical analysis, as well as the error in parameter estimation using equations (7.7) and (7.8). The overall absolute maximum error is 3.76%, 2.55%, and 2.17% for the elastic stiffness, yield force, and yield displacement, respectively. The mean error is much lower for all three parameters. A scatter plot showing the error in graphical form is show in a later section. These error values prove that the equations do a good job of predicting parameter values using the training data, but this does not validate the effectiveness of these equations for lengths and widths not specific to the training set. Therefore, the next step in the solution process was to analyze different combinations of L , b , and w to further validate the predictive equations.

7.2.5 In-Bounds Test Set

This set of test data is termed the “in-bounds” test set because all values of L and b are chosen such that they do not extend past either the lower or upper bound of the training data. This will test the effectiveness of the data for interpolation. In addition, values of w other than the original connecting width of 0.375 inches are tested. The complete set of test data geometry, as well as the ABAQUS calculated values of

elastic stiffness, yield force, and yield strength are presented in Table 19. None of these lengths or widths were previously used in the training data, and the values of all three parameters under consideration are within a reasonable range of the training data, so it is expected that the previous empirical equation will fit the data well.

While the original empirical equations fit the test data within reasonable error, the error in yield force was higher than anticipated with a maximum of approximately 6%. This is an acceptable error in experimental testing since there are so many sources of error possible in the experimental test; however, it is preferable to minimize the error in numerical calculations so that the overall error is ultimately decreased. Figure 54 graphically presents the percent error in yield force vs. the ABAQUS calculated yield force value. The error is smallest for tests 4 and 5, which are also the test points with a connecting width closest to the original 0.375 inches. This provides proof that an adjustment must be made to equations (7.7) and (7.8) in order to accurately predict all three parameters if the connecting width by necessity must be changed.

The solution to this is provided by adding a correction factor to the “load distribution” factor already in the equation. This width correction factor, λ , accounts for the difference in actual connecting width and assumed connecting width based on the constant value for w used in the training data set. The correction factor is seen in the new predictive equations as:

$$P_y = (2.011 + 6.432\alpha(1 - \lambda)) \left[\frac{F_y d [(1 - 0.847\beta)b]^2}{[(1 - 0.847\beta)L_{\text{eff}}]} \right] \quad (7.9)$$

$$K = (11.030 - 2.579\alpha(1 - \lambda)) \left[\frac{Ed [(1 - 0.487\beta)b]^3}{[(1 + 2.561\beta)L_{\text{eff}}]^3} \right] \quad (7.10)$$

Where: $\lambda = \frac{(w_0 - w)}{L}$ and $w_0 = 0.375$ inches

If the actual connecting width is larger than the original calibration width, λ will be negative. When substituted into equations (7.9) and (7.10), this will increase the yield force and decrease the percent error in calculation. When the actual width is less than the calibration width, the opposite will occur. If the actual width is the same as the calibration width, λ is equal to zero and no change occurs to either equation. Figure 55 shows the improvement in yield force error when using this correction factor.

7.2.6 Out-of-Bounds Test Set

Another potential concern when using the predictive equations is the validity of the equation when either the length or width is outside the upper or lower bounds of the training data set. The impact of this is

Table 19. "In-bounds" test data set.

Test Number	L (in)	b (in)	w (in)	K (lb/in)	P _y (lb)	δ _y (in)
1	2.10	0.175	0.315	14,435	187	0.0129
2	2.20	0.225	0.330	22,159	284	0.0128
3	2.30	0.225	0.345	20,122	268	0.0133
4	2.40	0.275	0.360	27,846	371	0.0133
5	2.60	0.325	0.390	33,018	462	0.0140
6	2.70	0.375	0.405	40,421	579	0.0143
7	2.80	0.375	0.420	37,711	556	0.0147
8	2.90	0.425	0.435	44,734	677	0.0151

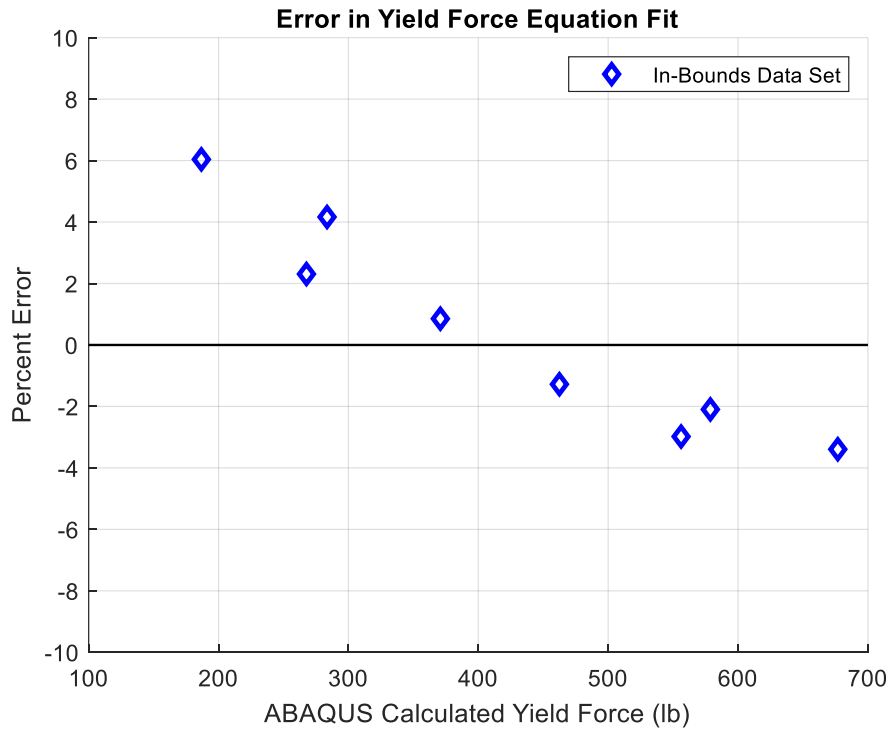


Figure 54. Original error in calculated yield force for in-bounds test data.

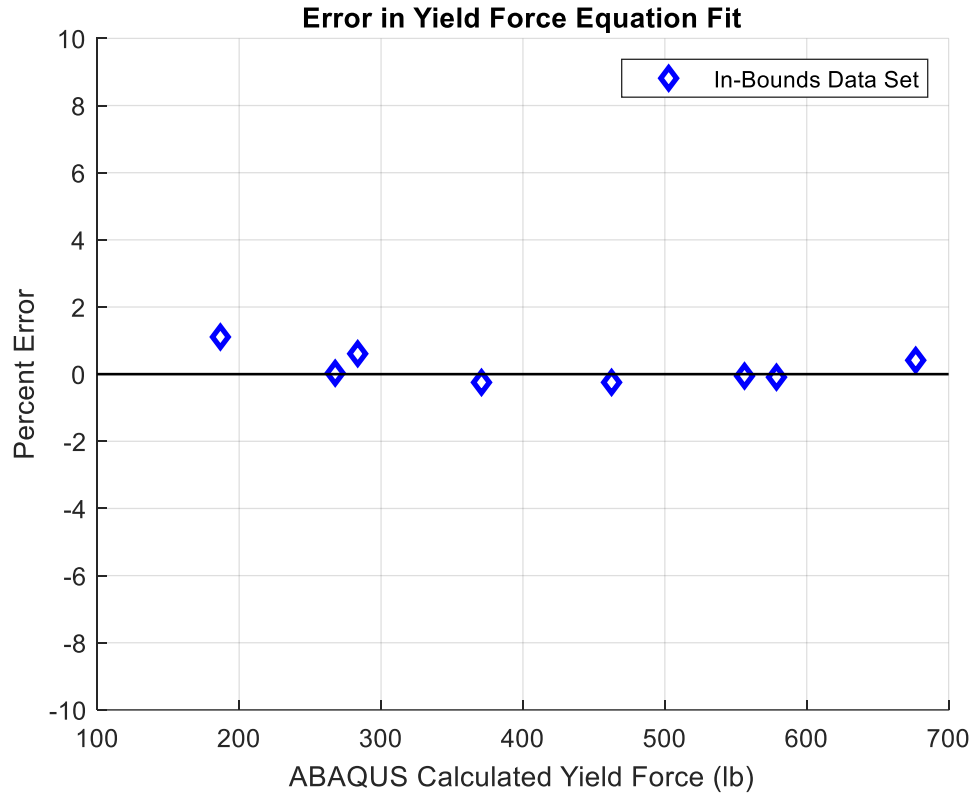


Figure 55. Error in calculated yield force when considering width correction factor.

explored in this section. Six data points were chosen for this test set – each corresponding to one or both of the parameters in question being extrapolated. A limit of 15% deviation from original bounds was set as the maximum, as it is not expected that the original estimation of necessary extents for the geometric parameters will have greater error than this. Table 20 shows the lengths and widths chosen, as well as the ABAQUS calculated values for all parameters of interest. The results of the equation fit are shown in the following section in conjunction with a final discussion on the strengths and weaknesses of the empirical equations as they apply to this work.

7.2.7 Conclusions Drawn based on Empirical Equations

The previous sections discussed the procedures used to arrive at the final form of the empirical equations, as well as two different groups of test data used to validate the usefulness of the equations for future BRB fabrication. Figure 56 through Figure 58 show the error in each estimated parameter using equations (7.9) and (7.10). Most data points are estimated within $\pm 2\%$ of the ABAQUS calculated value; however, there are notable exceptions. The most obvious of these exceptions are the three data points in the out-of-bounds test data set that utilize lengths and widths below the lower limit of the training set. The error in the predicted elastic stiffness and yield force is approximately 4 – 8%. This is very high when considering most other predictions are below 2% error. This shows that the predictive equations do not hold true if extrapolating past the lower bound of either geometric parameter. While this is not ideal, it is not an area of concern because the combination of such small width and length are not desirable to produce the elastic stiffness and yield force of the scaled BRBs needed in this project.

In addition to this, it is noticeable that there is a poorer fit to the data for lower elastic stiffness and yield force in general. But, these low stiffness values and higher estimation error generally correspond to a width values of 0.15 inches. This small of a width is not expected to be used for model BRBs necessary for this work, so the larger error in this instance is considered acceptable. In addition, the extrapolated data points past the upper bounds of the training data limits appear to be well estimated. These results provide confidence that the final form of the predictive equations will be highly useful in determining required dimensions for model BRBs based on the values of scaled strength and stiffness requirements even if the necessary strength and stiffness values are higher than currently expected and require a larger geometry.

7.3 Experimental Testing of the Rectangle-type BRB

The tests presented in this section were completed in an effort to validate the numerical model using experimental data. The new set of drawings for these experimental specimens can be found in Appendix B. The test specimens are labeled as “T3SX”, with “X” representing the specimen number. Specimens number

Table 20. Out-of-bounds test data set.

Test Number	L (in)	b (in)	w (in)	K (lb/in)	P _y (lb)	δ _y (in)
1	2.00	0.128	0.375	8,815	116	0.0132
2	1.70	0.150	0.375	19,973	207	0.0104
3	1.70	0.128	0.375	14,302	154	0.0108
4	3.00	0.518	0.375	57,410	906	0.0158
5	3.45	0.450	0.375	33,299	593	0.0178
6	3.45	0.518	0.375	43,800	771	0.0176

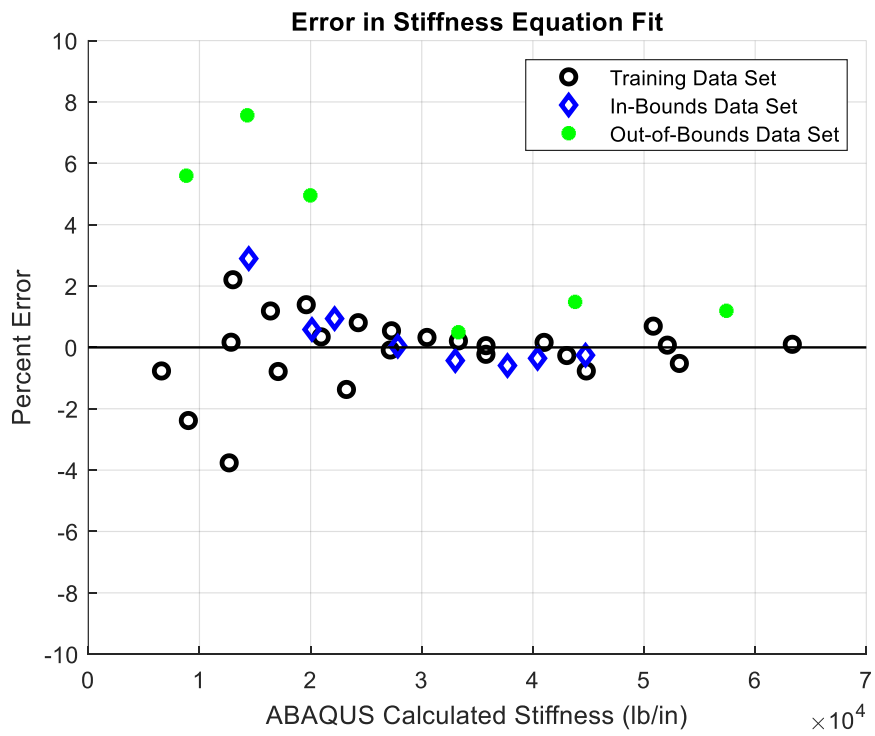


Figure 56. Percent error in stiffness estimation of all data points.

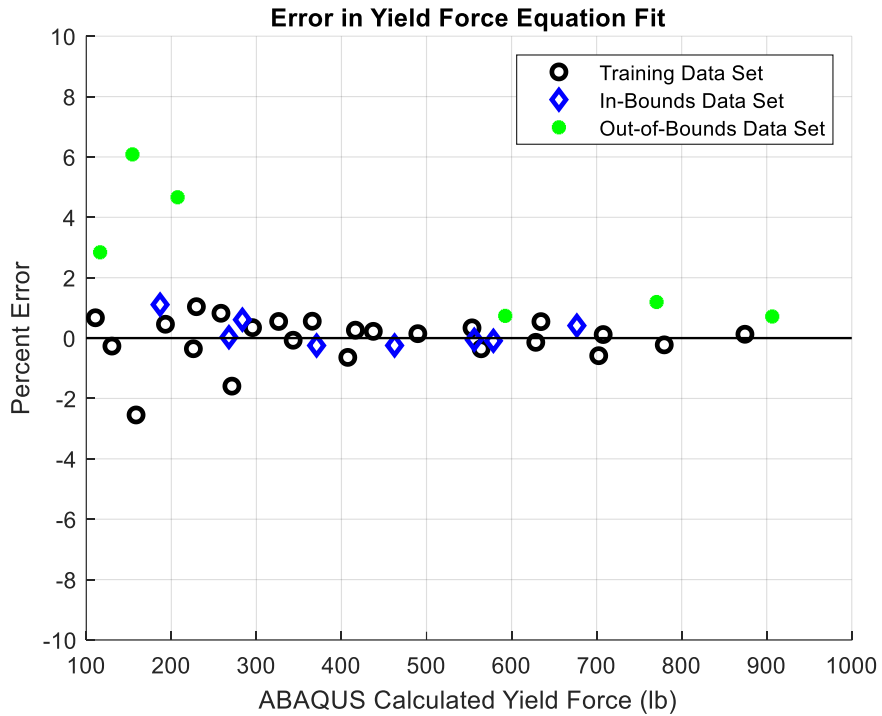


Figure 57. Percent error in yield force estimation of all data points.

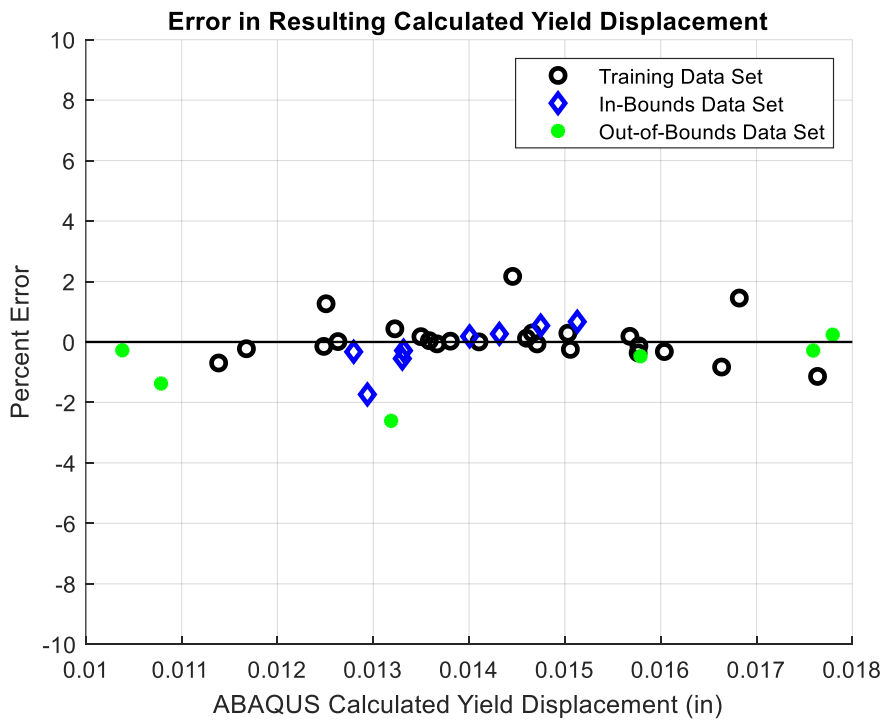


Figure 58. Percent error in yield displacement estimation of all data points.

1 and 2 are small BRBs, and specimens 3 and 4 are large BRBs. Prior to testing, measurements of all specimens were taken to determine the amount of tolerance in the waterjet cutting. These tolerances are shown in Table 21. Similar to the ring-type BRB calculations, tolerance levels were determined by subtracting the nominal dimension from the measured dimension. Therefore, a negative tolerance means the actual value was smaller than nominal, and a positive tolerance means the actual value was larger than nominal. Measurements were taken at multiple location, but only the average is shown for concise presentation.

Using the equations presented, the required length and width of a small and large BRB can be estimated using the scaled elastic stiffness and yield force values already obtained and presented in Table 4. The calculated geometric values are seen in Table 22, along with an estimate of the expected parameter values using ABAQUS analysis. The difference in the goal values from Table 4 and the estimated values in Table 22 are all less than 1%, which further validates the regression analysis used to obtain the form of the predictive equations. The next step in evaluating this new design was to experimentally test the small and large BRB. The experimental sizes of both specimens are presented in Table 23 along with an estimate of all parameters of interest. The length of the large experimental specimen is slightly different than the length estimated by the predictive equations because these experimental specimens were cut prior to completion of the full regression analysis. However, the estimated parameter values obtained in ABAQUS are still within 1% of the required values for the experimental specimens, so they will still provide useful results.

7.3.1 Small Rectangle-type BRB Experimental Results

Two experimental tests were completed for the small BRB. Both tests used the same displacement control pattern as described in chapter 5 for T2SX specimens, with $\Delta_{by} = 0.0143$ inches and $\Delta_{bm} = 0.13$ inches. The goal of these tests was threefold: (1) provide preliminary validation of the predictive equations, (2) test repeatability of the device, and (3) provide an experimental comparison for the entirety of the numerical force-displacement curve. The results of these 2 tests, along with their relevance to the stated goals are discussed in the following paragraphs.

The first goal of experimental testing was to provide preliminary validation of the predictive equations. This was done by calculating the elastic stiffness, yield force, and yield displacement of each experimental specimen to compare to the numerical results. A graphical comparison of the initial cyclic behavior of the two experimental test specimens and the corresponding ABAQUS specimen is seen in Figure 59. Table 24 lists the calculated elastic stiffness, yield force, and yield displacement for all three results. When calculating these parameters, no monotonic data was available as had been used in the initial parameter

Table 21. Waterjet tolerance for rectangle-type BRB specimens.

Identifier	b (in.)	Tolerance (in.)	L (in.)	Tolerance (in.)	L + 4b (in.)	Tolerance (in.)
T3S1	0.173	0.002	2.293	-0.002	2.979	0.000
T3S2	0.170	-0.001	2.293	-0.002	2.976	-0.003
T3S3	0.342	0.000	2.662	-0.003	4.030	-0.003
T3S4	0.342	0.000	2.664	-0.001	4.033	0.000

Table 22. ABAQUS estimated parameter values for BRB using predictive equations.

Specimen	L (in.)	b (in.)	K_m (lb./in.)	$P_{y,m}$ (lb.)	δ_y (in.)
Small	2.295	0.171	11,428	162	0.0142
Large	2.671	0.342	33,970	487	0.0143

Table 23. ABAQUS estimated parameter values for BRB using experimental geometry.

Specimen	L (in.)	b (in.)	K_m (lb./in.)	$P_{y,m}$ (lb.)	δ_y (in.)
Small	2.295	0.171	11,428	162	0.0142
Large	2.665	0.342	34,141	489	0.0143

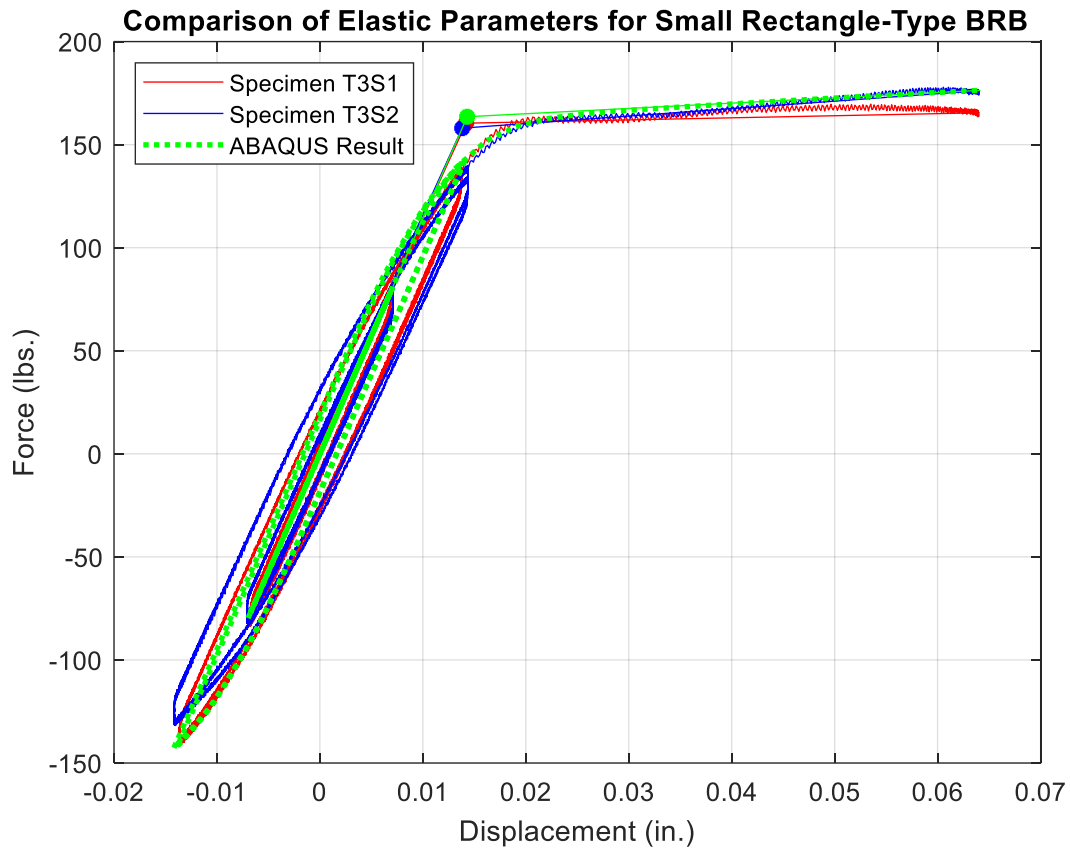


Figure 59. Graphical comparison of initial cyclic behavior for small rectangle-type BRB.

Table 24. Cyclic experimental results vs. cyclic ABAQUS results – small specimen.

Identifier	K_m (lb./in.)	$P_{y,m}$ (lb.)	δ_y (in.)
T3S1	10,960	160	0.0142
T3S2	10,991	158	0.0138
ABAQUS	11,433	165	0.0144

calculations. Therefore, an approximate yield force and yield displacement was calculated by finding the intersection of the initial elastic behavior and the plastic behavior at the beginning of the first cycle at an amplitude of $\Delta_b = 0.065$ inches, since this cycle was the first cycle to extend fully into the plastic range. Because some hardening has occurred by this point, the calculated yield point is slightly larger in magnitude than when calculated using a monotonic tension test, as is obvious when comparing the ABAQUS estimated values in Table 23 and Table 24. However, this estimation still provides a valid comparison between numeric and experimental parameters if performed in the same manner for all data sets.

The ABAQUS estimate matched the experimental data within approximately 4% for all parameters in both tests. Graphically, the behavior is also very similar between experimental and numerical analysis. There is some apparent hysteretic area in the experimental specimens at the first cyclic amplitude, but this is reasonably explained by compliance in the overall fixture due to the more complex interaction between the yielding plate and all physical connecting elements that was not modeled in the numerical analysis. Even with several simplifications to the numerical model, ABAQUS results still provide a good estimate of actual part behavior in the elastic and initial plastic ranges. The high degree of accuracy in numerical estimation of elastic parameters provides confidence that the predictive equations are accurate and can be used to determine model geometry for other sizes of BRB specimens in later phases of this project.

The second goal of these experimental tests was to determine if the device behavior was repeatable. According to the results in Table 24 and Figure 59, the behavior is very repeatable. All estimated parameters for T3S1 and T3S2 were very close in value, so it is reasonably concluded that the device behavior is well defined and repeatable. It is also worth noting that the rectangle-type device appears to be more accurately cut with the waterjet device as compared to the ring-type mechanism. This is obvious when comparing the tolerance values from Table 14 to those in Table 21. The reason for this improved accuracy is likely two-fold. The waterjet control is likely improved when cutting a less complex shape, so the straight lines of the rectangle-type device are beneficial. Secondly, physical measurement of the device geometry is more straightforward when measuring length and width as compared to diameter, so there is likely less human error in the measurements for the rectangle-type device. This improved accuracy is beneficial when considering the need to manufacture several small-scale devices that provide the same force-displacement behavior.

The third goal of these experimental tests was to obtain data for comparison against the entire numerical force-displacement curve. The comparison of the entire hysteretic curve for T3S1, T3S2, and the numerical analysis is shown in Figure 60. The numerical analysis does a very good job fitting the experimental data

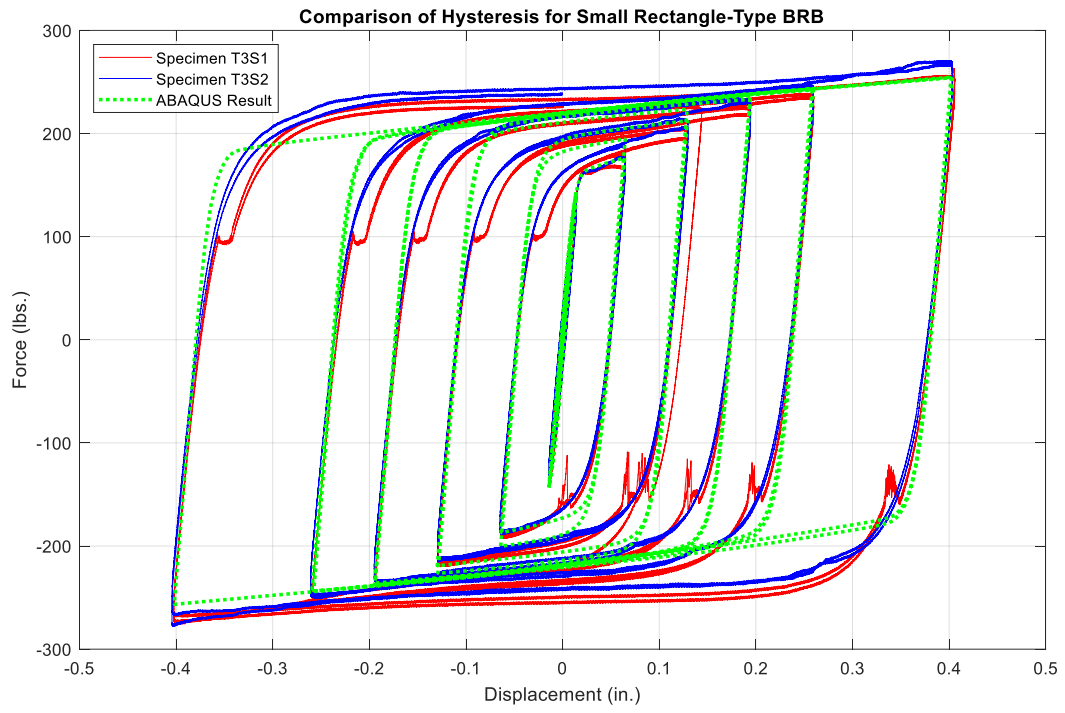


Figure 60. Comparison of entire hysteresis for small rectangle-type BRB.

up until a displacement amplitude of 0.13 inches. After this, the numerical estimate of force capacity is too low. This shows that the updated numerical model presented in chapter 6 was not adequate to capture the entirety of the behavior of the rectangle-type BRB. This is not unexpected because of the limited data that was available when forming the previous material model. The only cyclic data previously available was that of the ring-type BRB, so this is what was used to predict the hardening behavior of the rectangle-type BRB. However, the cyclic behavior of the ring-type specimen was a combination of the material behavior and the complex geometry of the part. It is therefore not directly transferable to the new device geometry. Even though the material model is not well suited to predict the axial force capacity of the rectangle-type BRB at high displacements, it is reasonable to conclude that a simple adjustment to the material input parameters may be made in ABAQUS to better fit the experimental results. This change in numerical modeling will be a part of future work to provide better estimates of experimental behavior for calibration of the OpenSees model to be used for the larger overall project.

The last notable result from the experimental tests of specimen T3S1 and T3S2 is the inconsistency in connection tightness. This is obvious when comparing the hysteresis of T3S1 with that of T3S2 in Figure 60. T3S1 still has some slip present in the connections, which is seen graphically when the curve changes displacement without a large change in force. This happens consistently at approximately 100 lbs. in tension and 150 lbs. in compression. This slip is no longer visible for specimen T3S2. This difference is due to human error in the tightening of the bolted connections. The bolts at either end of the yielding plate (bolts B1-B4 in Figure 24) were manually tightened by feel. There is inherently a lot of error in this. While the goal was to tighten these bolts as much as possible, there was an obvious difference in tightness that led to slip in the first experimental test. It is therefore imperative to have a method of tightening the connections that provides a higher degree of certainty for the actual slip resistance of the connection. This is an area of future work.

7.3.2 Large Rectangle-type BRB Experimental Results

It was intended to capture accurate results from large BRB tests using specimens T3S3 and T3S4; however, there was notable error in the testing of T3S3 that led to the test being stopped. This error was due to the poor connection strength of the bolts, as discussed previously. Therefore, the connection of the yielding plate to the grip plate was redesigned and specimen T3S4 was tested with the new connection detail. The new connection detail featured 1/4-28 Grade 8 bolts in place of the #10 machine screws previously used at locations B1 – B4 in Figure 24. These bolts were each torqued to 15 ft-lb, and the larger bolts (location A1 & A2 in Figure 24) were torqued to 45 ft-lb to ensure adequate preload force to resist slip in the connections. This improved design detail is shown in Figure 61.

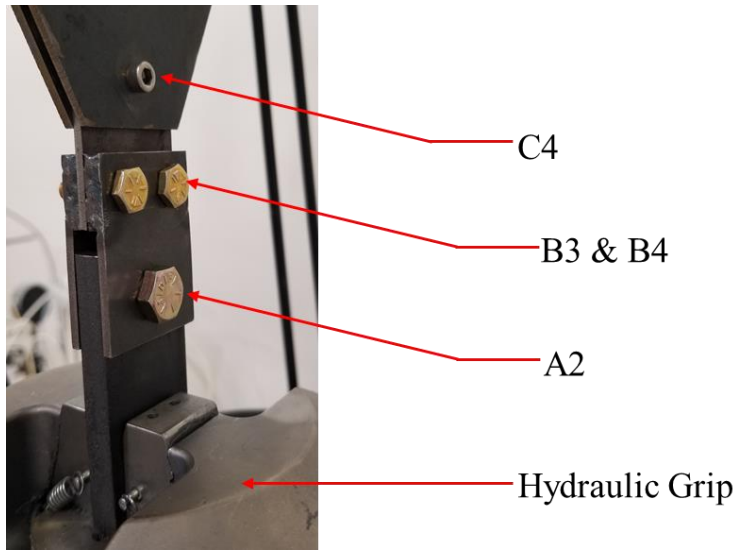


Figure 61. Updated connection detail to resist slip.

Specimen T3S4 was then tested using the same displacement control as used in previous tests. The results in the elastic zone up to the initial transition to the plastic zone are seen in Figure 62 for both T3S4 and the ABAQUS numerical estimation. The estimated value of elastic stiffness, yield force, and yield displacement are seen in Table 25. The ABAQUS estimation was higher than the experimental data for all three parameters, but the maximum percent error was only 0.80%. This shows there is a strong correlation between the parameter estimates from the numerical simulation and those obtained experimentally. This provides validation of the rectangle-type parameterized design for both small and large model BRBs.

Figure 63 shows the full hysteretic curve of both the experimental specimen and the ABAQUS analysis. Similarly to the observation from the small specimen, it is clear that the material hardening model needs to be updated to better capture the entire hysteretic behavior of this device. Even though there are still numeric updates to be done, this experimental result clearly shows the symmetric behavior of the model BRB at multiple displacement amplitudes, which was the overall desired outcome of these tests.

7.4 Conclusions on the Rectangle-type BRB

Initial experimental tests of the small-scale BRB provide confidence that this design will yield an appropriately scaled hysteretic curve that mimics its large-scale counterpart. Figure 64 shows the comparison of the small BRB to the large BRB. The behavior is the same, with the large BRB acting as a scaled version of the small BRB. This is the goal of this work, so these initial experimental tests provide validation of the completion of this goal. The asymmetric behavior of the ring-type BRB is not seen in either size of specimen, showing this issue has been mitigated with the design updates. The predictive equations also provide reasonable geometric values for a range of scaled specimens that are large enough to be accurately cut with the waterjet machine but are small enough that they will fit in the overall frame bay when used in future shake table testing. The results presented in this chapter conclusively provide numeric evidence that supports the use of this device to replicate the prototype BRB.

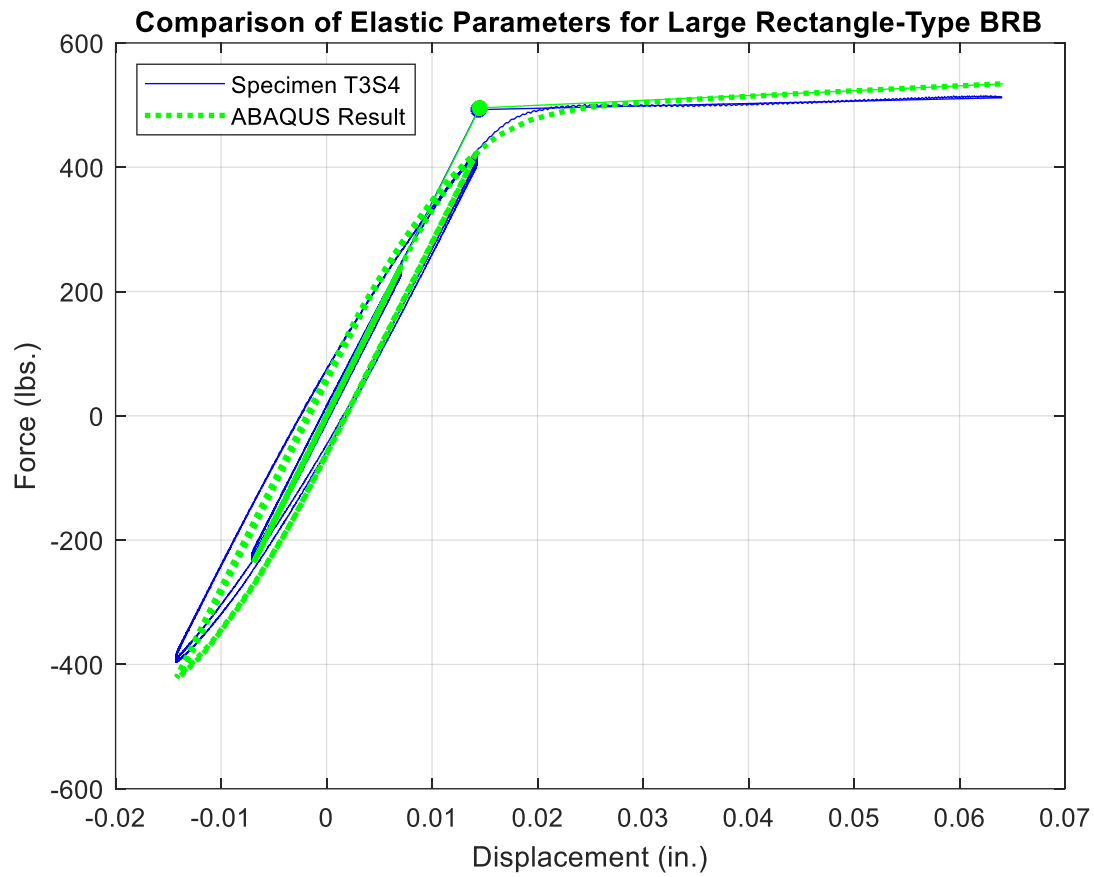


Figure 62. Graphical comparison of initial cyclic behavior for large rectangle-type BRB.

Table 25. Cyclic experimental results vs. cyclic ABAQUS results - large specimen.

Identifier	K_m (lb./in.)	$P_{y,m}$ (lb.)	δ_y (in.)
T3S4	33,870	493	0.0144
ABAQUS	34,141	495	0.0145

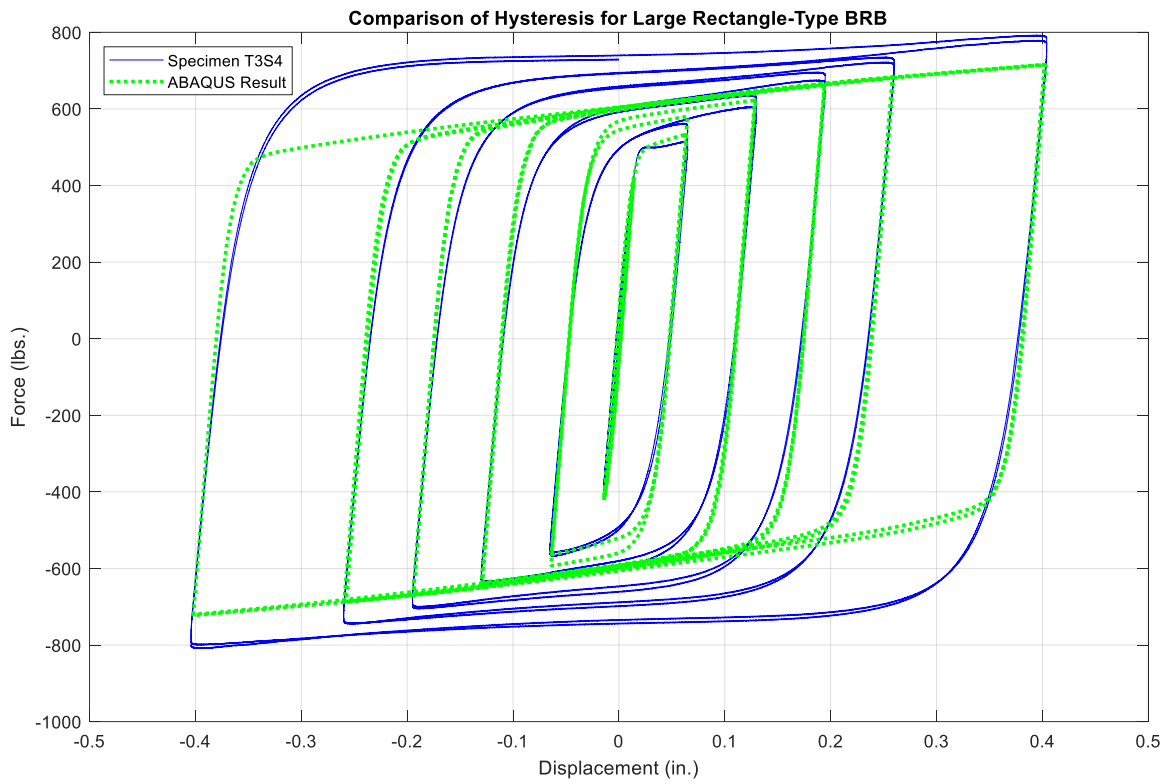


Figure 63. Comparison of entire hysteresis for large rectangle-type BRB.

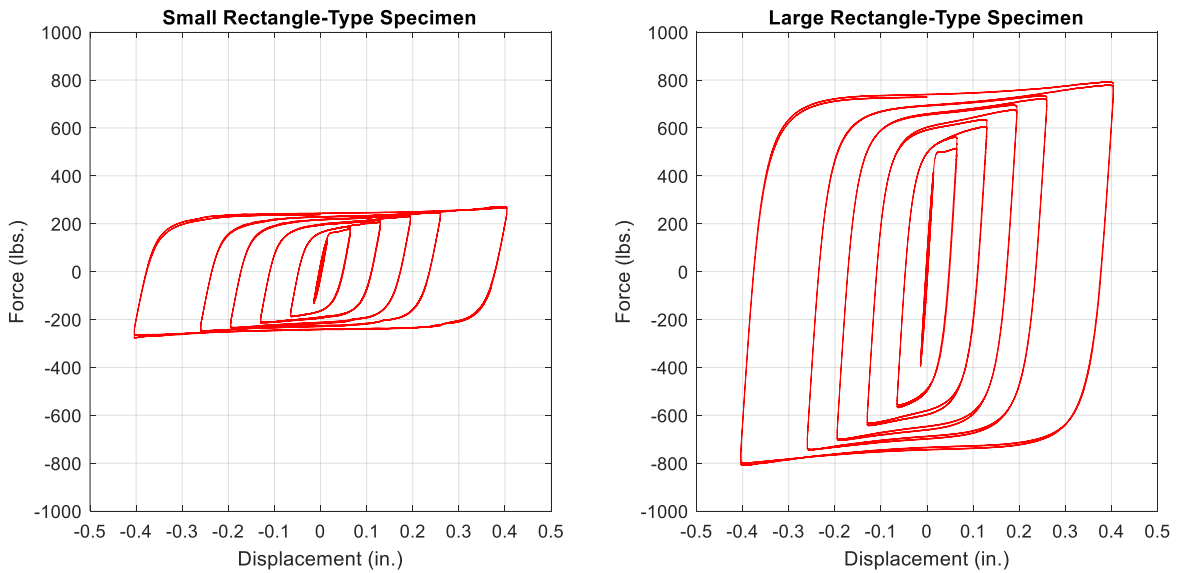


Figure 64. Comparison of small and large BRB experimental hysteretic curve.

8 Conclusions & Future Work

The work presented in this thesis is a compilation of the design development process for a small-scale BRB. It is a part of a larger project that aims to evaluate the resiliency of strongback braced frames (SBF) when resisting dynamic loads during seismic events. Small-scale experimental shake table tests will be performed as part of the project. The main source of energy dissipation in SBFs are buckling restrained braces (BRB). While there is extensive literature documenting both large-scale BRB functionality and the use of small-scale testing, to the best of the knowledge of the author, there is no literature focused on the design and validation of a BRB at a scale small enough for use in the planned shake table tests. Therefore, the goal of this work was to design a geometrically dissimilar but functionally similar device that produced a properly scaled, symmetric force-displacement curve characteristic of BRBs.

The first step in this process was the identification of required scaling ratios. A geometrically similar model was not necessary, as the main goal of this work is to model the strength and stiffness of the SBF in order to evaluate its global response to seismic load demands. The scaling ratios were chosen such that the size of the device is reasonable for assembly while still maintaining a required seismic load less than the maximum payload of the shake table available for testing. Following these decisions, an initial iteration of the small-scale device was discussed. This device was designed to dissipate energy through flexural yielding and was initially sized using moment and deflection relationships from basic mechanics. However, the required geometry of this device was larger than desired, so it was abandoned in favor of the colinear ring-type yielding device.

The ring-type device was still formulated to dissipate energy through flexural bending, but the geometry of the central yielding portion of the device was circular as opposed to beam-like in nature, which allowed the device to better fit in the frame bay of the overall structure. The ring-type device was initially sized using an approximation from basic mechanics, refined using ABAQUS finite element software, and eventually tested experimentally. Errors in the initial numerical analysis and material hardening model were captured during the experimental tests, and the numerical model was updated to better reflect the actual device behavior. The ring-type device was ultimately shown to provide an asymmetric response due to differences in the deformed shape and stress distribution at extreme tension as compared to extreme compression.

Because of this, a new rectangle-type device was designed. This device was first tested numerically using the refined finite element model to ensure an expected symmetric response at high displacement levels. Once this was confirmed, a suite of ABAQUS analyses were utilized in a nonlinear regression analysis to

determine the form of predictive equations that would accurately calculate required BRB geometry. The device was then experimentally tested to determine the accuracy of the numerical estimate of its behavior. The parameterized elastic stiffness, yield force, and yield displacement of both a small and large size of BRB were determined to be within a reasonable range of accuracy, which lends validity to the overall design and provides confidence in future work.

There are many potential pathways of future work to broaden the impact of the model BRB. The main area of future work as it pertains to the overall project is continuation of numerical updating. The hardening model used in the current ABAQUS design performs well for estimation of the elastic stiffness and yield force of the BRB. However, it does not well match the entire experimental hysteretic curve. This can be addressed by utilizing an OpenSees numerical model rather than continued updating of the ABAQUS model. This is a favorable option because OpenSees is the program better fit to overall numerical analysis of the SBF. Development of an equivalent uniaxial stress-strain relationship to fit the behavior of the model BRB would facilitate numerical evaluation of a small-scale SBF that utilized this BRB device.

There is also potential for exploration of the device functionality using different materials, or with slight changes to the yielding plate geometry. As already discussed, changing the connecting width, w , was shown to have a rather significant impact on the effectiveness of the yield force and elastic stiffness predictive equations. There is potential that other changes in geometry or material parameters may have a similar impact. There are still many areas of research that need to be explored for further expansion of the understanding of this small-scale device. However, the experimental success of this design has proven this device can provide an accurately scaled analog of prototype BRB behavior. This design will be used as the inelastic energy dissipation mechanism in shake table tests, which are an integral part of the overall project.

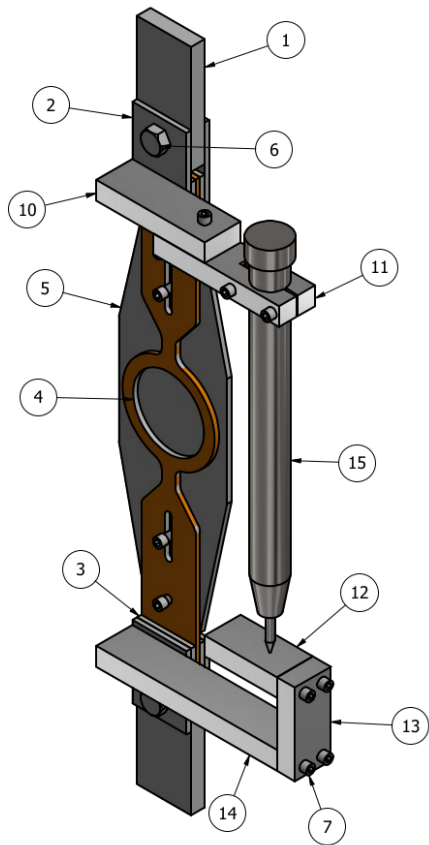
References

- A01 Committee. (2018). Specification for Steel, Sheet and Strip, Hot-Rolled, Carbon, Structural, High-Strength Low-Alloy, High-Strength Low-Alloy with Improved Formability, and Ultra-High Strength. ASTM International.
- AISC. (2016). "Seismic Provisions for Structural Steel Buildings." American Institute of Steel Construction.
- ASCE. (2017). "Minimum Design Loads and Associated Criteria for Buildings and Other Structures." American Society of Civil Engineers.
- Buckingham, E. (1914). "On Physically Similar Systems; Illustrations of the Use of Dimensional Equations." *Physical Review*, 4(4), 345–376.
- Casaburo, A., Petrone, G., Franco, F., and De Rosa, S. (2019). "A Review of Similitude Methods for Structural Engineering." *Applied Mechanics Reviews*, 71(3).
- Chung, W.-J., Yun, C.-B., Kim, N.-S., and Seo, J.-W. (1999). "Shaking table and pseudodynamic tests for the evaluation of the seismic performance of base-isolated structures." *Engineering Structures*, 21(4), 365–379.
- Chunyu, T., Xiao, C., Hong, Z., and Jinzhe, C. (2012). "Shaking Table Test and Seismic Performance Evaluation of Shanghai Tower." *International Journal of High-Rise Buildings*, 1(3).
- Coutinho, C. P., Baptista, A. J., and Rodrigues, J. D. (2016). "Reduced scale models based on similitude theory: A review up to 2015." *Engineering Structures*, 119, 81–94.
- Dassault Systèmes Simulia Corp. (2010). "Abaqus Analysis User's Manual." <http://130.149.89.49:2080/v6.10/books/usb/default.htm?startat=pt09ch35s02aus173.html>.
- Dehghani, M., and Tremblay, R. (2018). "Design and full-scale experimental evaluation of a seismically enduring steel buckling-restrained brace system." *Earthquake Engineering & Structural Dynamics*, 47(1), 105–129.
- E28 Committee. (2016). Test Methods for Tension Testing of Metallic Materials. ASTM International.
- Engineering Library. (2021). "Circular Rings and Arches." <https://engineeringlibrary.org/reference/circular-rings-arches-air-force-stress-manual>.
- Gong, Y. P., Hyde, C. J., Sun, W., and Hyde, T. H. (2010). "Determination of material properties in the Chaboche unified viscoplasticity model." *Proceedings of the Institution of Mechanical Engineers, Part L: Journal of Materials: Design and Applications*, 224(1), 19–29.
- Goodier, J. N., and Thomson, W. T. (1944). Applicability of Similarity Principles to Structural Models. Technical Note, National Advisory Committee for Aeronautics, 69.

- Gray, M., Christopoulos, C., and Packer, J. (2017). "Design and Full-Scale Testing of a Cast Steel Yielding Brace System in a Braced Frame." *Journal of Structural Engineering*, 143(4).
- Gray, M., Christopoulos, C., Packer, J., and Lignos, D. (2012). "Development, Validation, and Modeling of the New Cast Steel Yielding Brace System." 20th Analysis and Computation Specialty Conference, American Society of Civil Engineers, Chicago, Illinois, United States, 71–82.
- Hu, F., Shi, G., and Shi, Y. (2016). "Constitutive model for full-range elasto-plastic behavior of structural steels with yield plateau: Calibration and validation." *Engineering Structures*, 118, 210–227.
- Jia, L.-J., Ge, H., Maruyama, R., and Shinohara, K. (2017). "Development of a novel high-performance all-steel fish-bone shaped buckling-restrained brace." *Engineering Structures*, 138, 105–119.
- Jia, L.-J., and Kuwamura, H. (2014). "Prediction of Cyclic Behaviors of Mild Steel at Large Plastic Strain Using Coupon Test Results." *Journal of Structural Engineering*, 140(2).
- Kersting, R. A., Fahnestock, L. A., and Lopez, W. A. (2016). *Seismic design of steel buckling-restrained braced frames: a guide for practicing engineers*. National Institute of Standards and Technology, Gaithersburg, MD.
- Kim, N.-S., Kwak, Y.-H., and Chang, S.-P. (2004). "Pseudodynamic Tests on Small-Scale Steel Models Using the Modified Similitude Law." Vancouver, B.C., Canada.
- Kim, W., El-Attar, A., and White, R. N. (1988). *Small Scale Modeling Techniques for Reinforced Concrete Structures Subjected to Seismic Loads*. Technical Report, National Center for Earthquake Engineering Research, 92.
- Knappett, J. A., Reid, C., Kinmond, S., and O'Reilly, K. (2011). "Small-Scale Modeling of Reinforced Concrete Structural Elements for Use in a Geotechnical Centrifuge." *Journal of Structural Engineering*, 137(11), 1263–1271.
- Koetaka, Y., Narihara, H., and Tsujita, O. (2001). "Experimental Study on Buckling Restrained Braces." Beijing, China, 7.
- Leicester, R. H. (1973). *Effect of Size on the Strength of Structures*. Division of Building Research Technological Paper, Commonwealth Scientific and Industrial Research Organization, Australia.
- Li, C. S., Lam, S. S., Zhang, M. Z., and Wong, Y. L. (2006). "Shaking Table Test of a 1:20 Scale High-Rise Building with a Transfer Plate System." *Journal of Structural Engineering*, 132(11), 1732–1744.
- Lignos, D. (2008). "Sidesway Collapse of Deteriorating Structural Systems Under Seismic Excitations." Stanford University.
- Lu, X., Chen, Y., and Mao, Y. (2012). "Shaking table model test and numerical analysis of a supertall building with high-level transfer storey." *The Structural Design of Tall and Special Buildings*, 21(10), 699–723.

- Lu, X., Zhou, Y., and Yan, F. (2008). "Shaking Table Test and Numerical Analysis of RC Frames with Viscous Wall Dampers." *Journal of Structural Engineering*, 134(1), 64–76.
- Murphy, G. (1950). *Similitude in Engineering*. The Ronald Press Company, New York.
- Palazzo, G., López-Almansa, F., Cahís, X., and Crisafulli, F. (2009). "A low-tech dissipative buckling restrained brace. Design, analysis, production and testing." *Engineering Structures*, 31(9), 2152–2161.
- Simpson, B., and Mahin, S. (2018a). "Experimental and Numerical Investigation of Strongback Braced Frame System to Mitigate Weak Story Behavior." *Journal of Structural Engineering*, 144(2).
- Simpson, B., and Mahin, S. (2018b). "Design Development of a Four-Story Strongback Braced Frame." *Key Engineering Materials*, 763, 1050–1057.
- Talebi, E., Tahir, M. M., Zahmatkesh, F., and Kueh, A. B. H. (2014). "Comparative study on the behaviour of Buckling Restrained Braced frames at fire." *Journal of Constructional Steel Research*, 102, 1–12.
- Talley, P. C. (2018). "Capacity design methods for strongback braced frames." The University of Tennessee, Knoxville.
- Tanamal, A., Eatherton, M., and Hajjar, J. F. (2009). *Controlled Rocking of Steel-Framed Buildings with Replaceable Energy Dissipating Fuses*. University of Illinois at Urbana-Champaign, 65.
- Torkamani, S., Jafari, A. A., and Navazi, H. M. (2008). "Scaled Down Models for Free Vibration Analysis of Orthogonally Stiffened Cylindrical Shells Using Similitude Theory." Anchorage, AL, 12.
- Tremblay, R., Poncet, L., Neville, R., and DeVall, R. (2004). "Testing and Design of Buckling Restrained Braces for Canadian Application.pdf." Vancouver, B.C., Canada.
- Wang, W., Fang, C., Zhao, Y., Sause, R., Hu, S., and Ricles, J. (2019). "Self-centering friction spring dampers for seismic resilience." *Earthquake Engineering & Structural Dynamics*, 48(9), 1045–1065.
- Wissmunn, W. (1968). "Dynamic Stability of Space Vehicles." 53.
- Xiang, P., Jia, L.-J., Shi, M., and Wu, M. (2017). "Ultra-low cycle fatigue life of aluminum alloy and its prediction using monotonic tension test results." *Engineering Fracture Mechanics*, 186, 449–465.

Appendix A



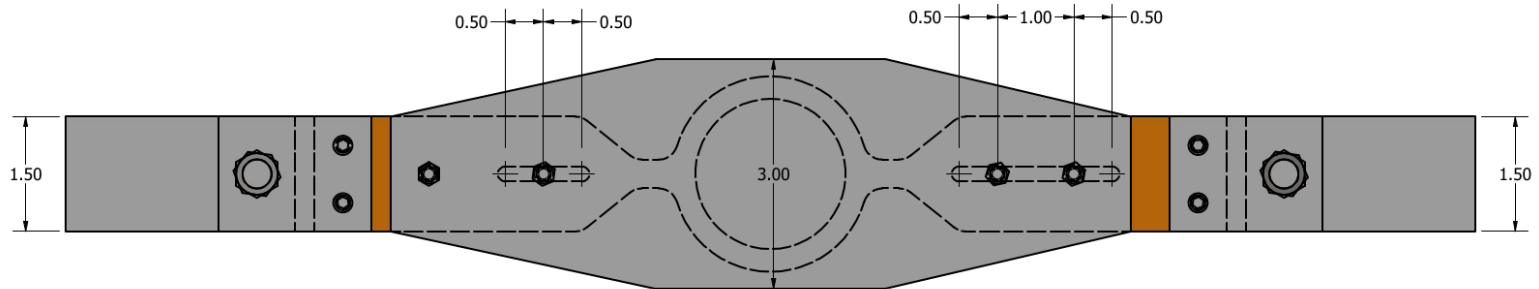
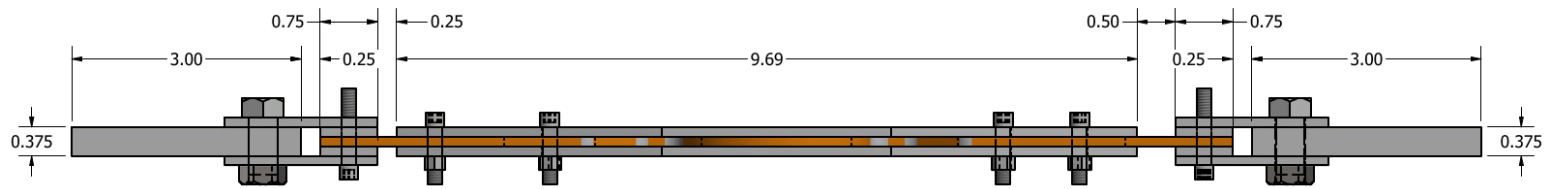
NOTE: Top confining plate not shown for clarity.

FABRICATED PARTS			
Item Number	Part Description	Qty	Page Number
1	Grip Plate	2	3
2	Splice Plate	4	4
3	Filler Plate	4	5
4	Yielding Plate	3	6 & 7
5	Confining Plate	2	8 & 9
10	LVDT Brace #1	1	10
12	LVDT Brace #3	1	11
13	LVDT Brace #4	1	12
14	LVDT Brace #5	1	13

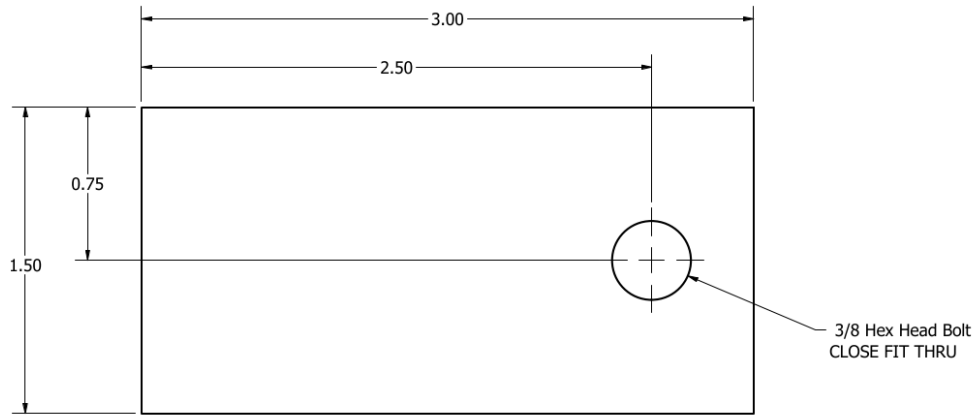
PURCHASED PARTS				
Item Number	Part Description	Qty	Part Number	Supplier
6	1" Lg. 3/8"-24 Class 2A Gr. 8 Steel Hex Head Screw	2	92620A655	McMaster-Carr
7	1" Lg. 10-32 Class 3A 18-8 Stainless Steel Socket Head Screw	12	92196A274	McMaster-Carr
8	3/8"-24 Class 2B Gr. 8 Steel Hex Nut	2	94895A815	McMaster-Carr
9	10-32 Class 3B 18-8 Stainless Steel Hex Nut	4	91834A105	McMaster-Carr

PREVIOUSLY FABRICATED & PURCHASED PARTS		
Item Number	Part Description	Qty
11	LVDT Brace #2	1
15	LVDT	1

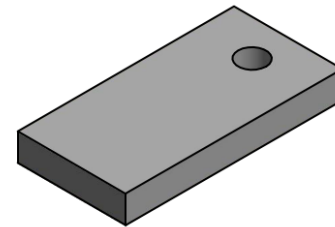
TITLE			
BUCKLING RESTRAINED BRACE - COMPONENT TEST			
DEPARTMENT			PART MATERIAL
CIVIL & ENVIRONMENTAL ENGINEERING - STRUCTURAL			STEEL & ALUMINUM
DESIGNED BY	DATE	UNITS	SHEET NUMBER
LINDSAY HELFERICH	12/2/2020	INCHES	1 OF 14



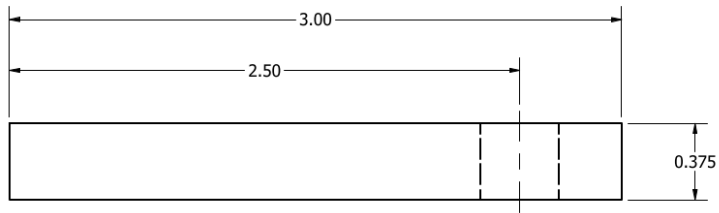
TITLE			
ALTERNATE VIEWS			
DEPARTMENT			PART MATERIAL
CIVIL & ENVIRONMENTAL ENGINEERING - STRUCTURAL			STEEL
DESIGNED BY	DATE	UNITS	SHEET NUMBER
LINDSAY HELFERICH	12/2/2020	INCHES	2 OF 14



PLAN VIEW
SCALE 2 : 1

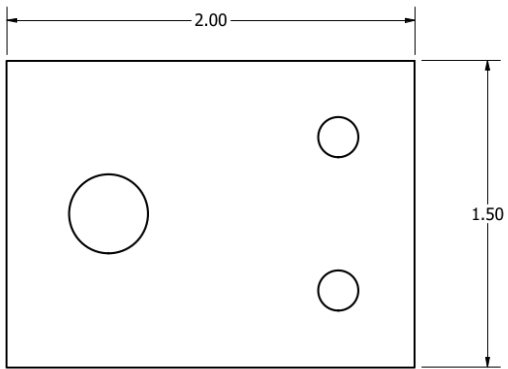


ISOMETRIC VIEW
SCALE 1 : 1

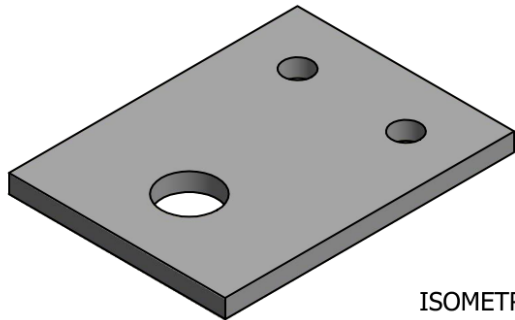


SIDE VIEW
SCALE 2 : 1

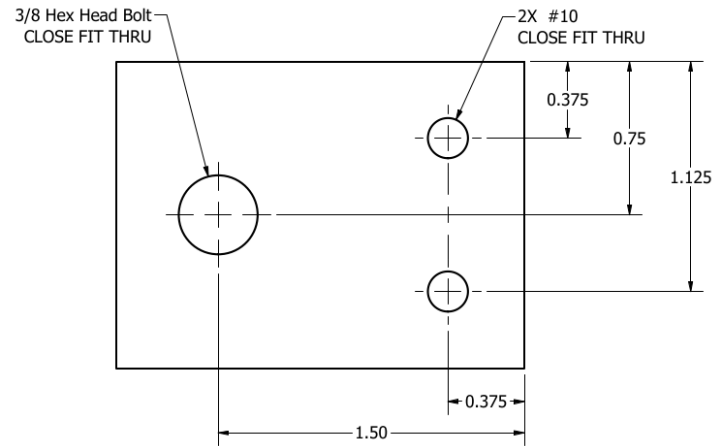
TITLE			
GRIP PLATE			
DEPARTMENT			PART MATERIAL
CIVIL & ENVIRONMENTAL ENGINEERING - STRUCTURAL			STEEL
DESIGNED BY	DATE	UNITS	SHEET NUMBER
LINDSAY HELFERICH	12/2/2020	INCHES	3 OF 14



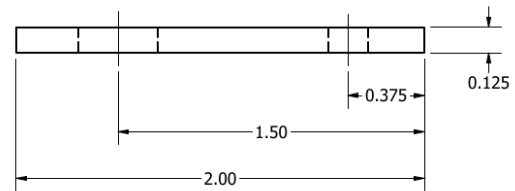
PLAN VIEW - GEOMETRY
SCALE 2 : 1



ISOMETRIC VIEW
SCALE 2 : 1



PLAN VIEW - HOLE DIMENSIONS
SCALE 2 : 1

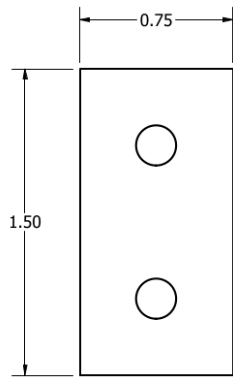


TOP VIEW
SCALE 2 : 1

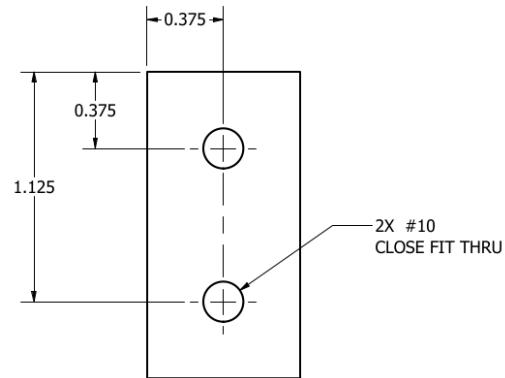
NOTES:

1. This piece is to be fabricated via waterjet cutting.

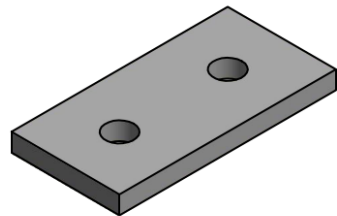
TITLE			
SPLICE PLATE			
DEPARTMENT			PART MATERIAL
CIVIL & ENVIRONMENTAL ENGINEERING - STRUCTURAL			STEEL
DESIGNED BY	DATE	UNITS	SHEET NUMBER
LINDSAY HELFERICH	12/2/2020	INCHES	4 OF 14



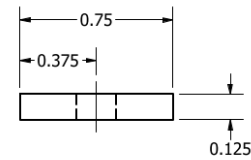
PLAN VIEW - GEOMETRY
SCALE 2 : 1



PLAN VIEW - HOLE DIMENSIONS
SCALE 2 : 1



ISOMETRIC VIEW
SCALE 2 : 1

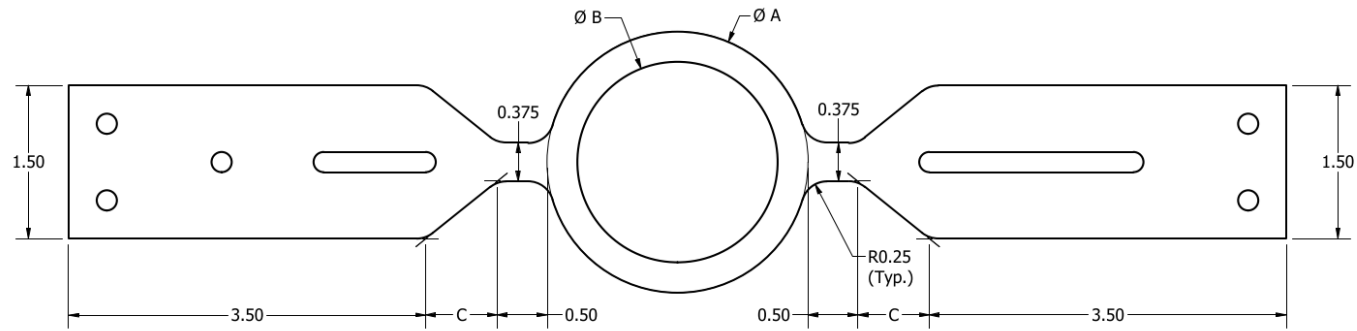


TOP VIEW
SCALE 2 : 1

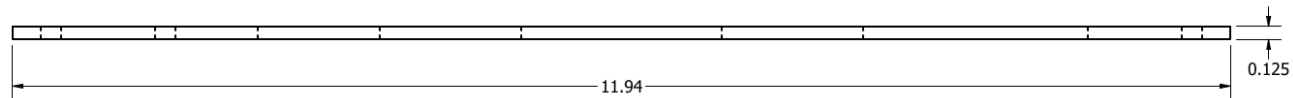
NOTES:

1. This piece is to be fabricated via waterjet cutting.

TITLE			
FILLER PLATE			
DEPARTMENT			PART MATERIAL
CIVIL & ENVIRONMENTAL ENGINEERING - STRUCTURAL			STEEL
DESIGNED BY	DATE	UNITS	SHEET NUMBER
LINDSAY HELFERICH	12/2/2020	INCHES	5 OF 14



FRONT VIEW
SCALE 1 : 1

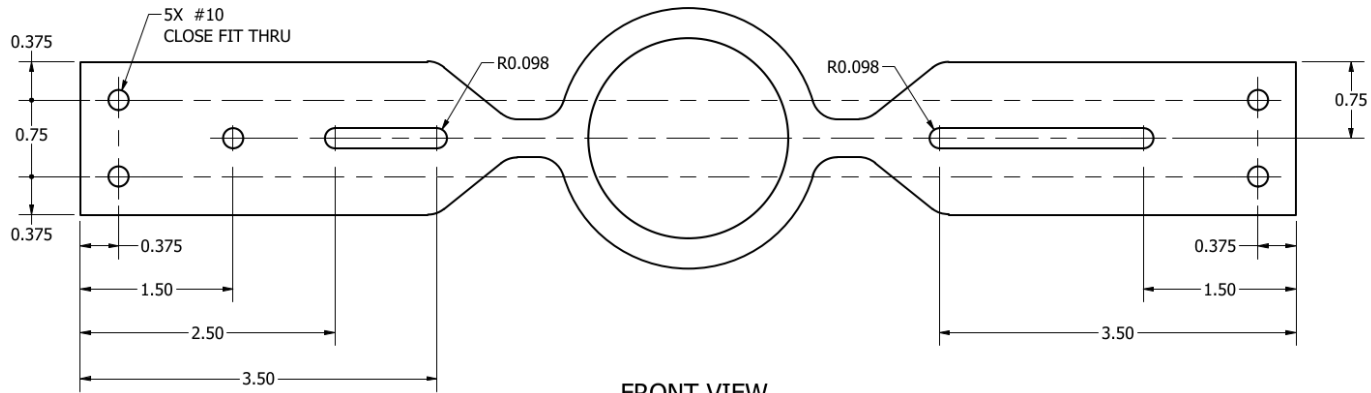


TOP VIEW
SCALE 1 : 1

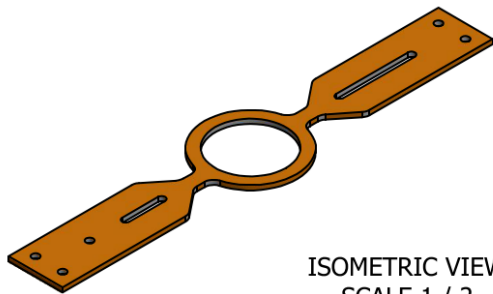
YIELDING PLATE DIMENSIONS			
PLATE NUMBER	DIMENSION "A"	DIMENSION "B"	DIMENSION "C"
1	1.959	1.671	0.988
2	2.330	1.870	0.803
3	2.555	1.962	0.690

- NOTES:
 1. This piece is to be fabricated via waterjet cutting.
 2. Hole geometry and dimensions are shown on sheet 7.

TITLE			
YIELDING PLATE - SHEET 1			
DEPARTMENT			PART MATERIAL
CIVIL & ENVIRONMENTAL ENGINEERING - STRUCTURAL			STEEL
DESIGNED BY	DATE	UNITS	SHEET NUMBER
LINDSAY HELFERICH	12/2/2020	INCHES	6 OF 14

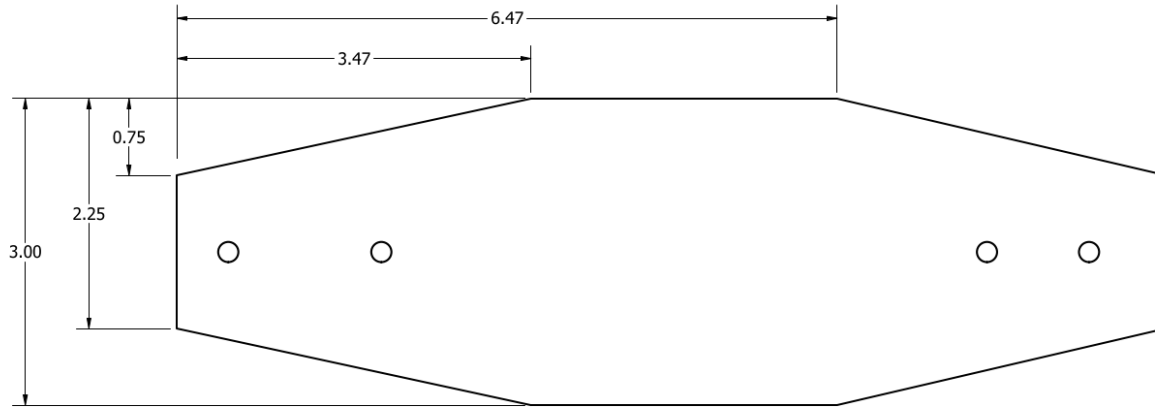


FRONT VIEW
SCALE 1 : 1

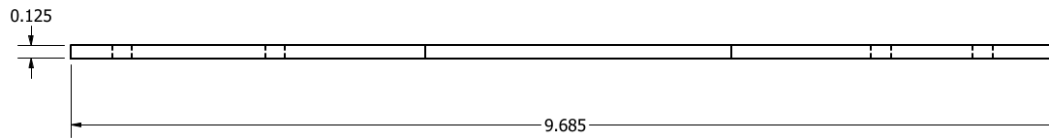


ISOMETRIC VIEW
SCALE 1 / 2

TITLE			
YIELDING PLATE - SHEET 2			
DEPARTMENT			PART MATERIAL
CIVIL & ENVIRONMENTAL ENGINEERING - STRUCTURAL			STEEL
DESIGNED BY	DATE	UNITS	SHEET NUMBER
LINDSAY HELFERICH	12/2/2020	INCHES	7 OF 14



PLAN VIEW - GEOMETRY
SCALE 1:1

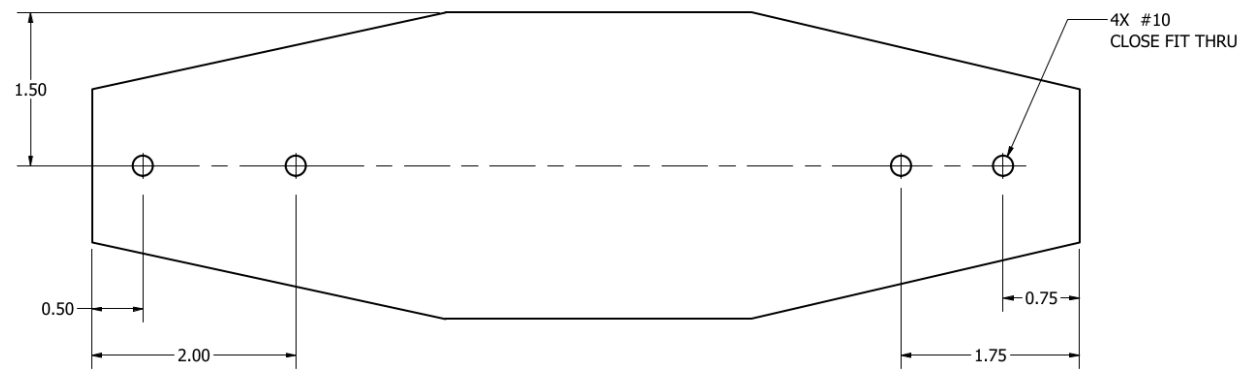


SIDE VIEW
SCALE 1:1

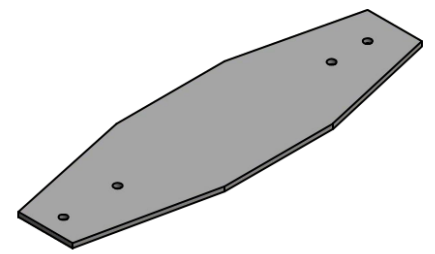
NOTES:

1. This piece is to be fabricated via waterjet cutting.
2. Hole geometry and dimensions are shown on sheet 9.

TITLE			
CONFINING PLATE - SHEET 1			
DEPARTMENT			PART MATERIAL
CIVIL & ENVIRONMENTAL ENGINEERING - STRUCTURAL			STEEL
DESIGNED BY	DATE	UNITS	SHEET NUMBER
LINDSAY HELFERICH	12/2/2020	INCHES	8 OF 14

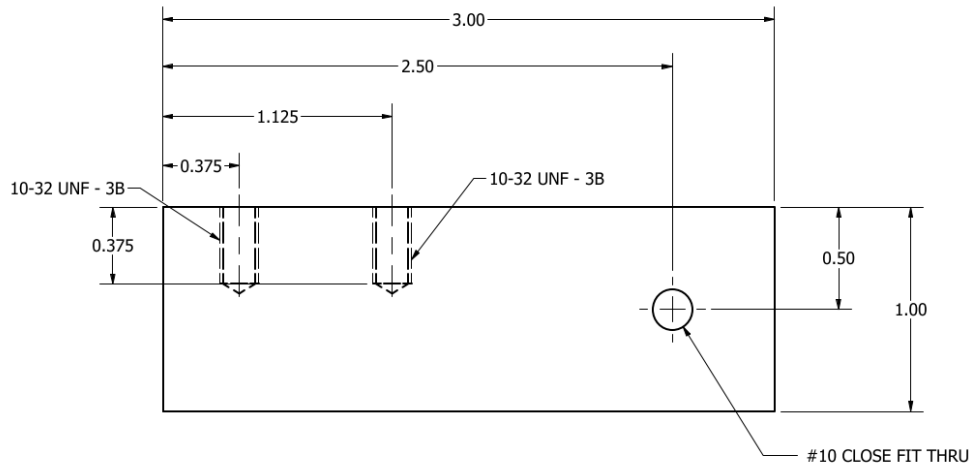


PLAN VIEW - HOLE DIMENSIONS
SCALE 1 : 1

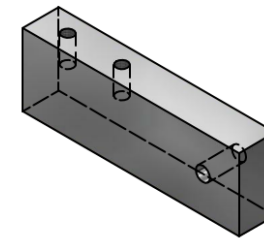


ISOMETRIC VIEW
SCALE 1 / 2

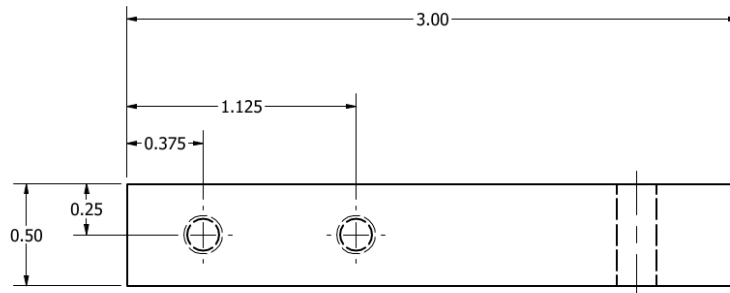
TITLE			
CONFINING PLATE - SHEET 2			
DEPARTMENT			PART MATERIAL
CIVIL & ENVIRONMENTAL ENGINEERING - STRUCTURAL			STEEL
DESIGNED BY	DATE	UNITS	SHEET NUMBER
LINDSAY HELFERICH	12/2/2020	INCHES	9 OF 14



PLAN VIEW
SCALE 2 : 1

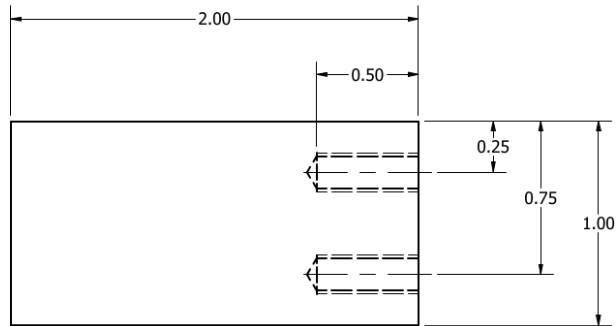


ISOMETRIC VIEW
SCALE 1 : 1

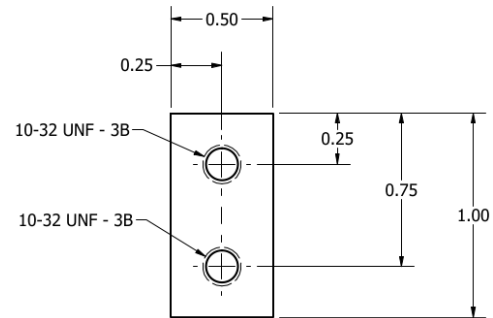


SIDE VIEW
SCALE 2 : 1

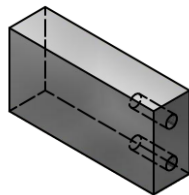
TITLE			
LVDT BRACE #1			
DEPARTMENT			PART MATERIAL
CIVIL & ENVIRONMENTAL ENGINEERING - STRUCTURAL			ALUMINUM
DESIGNED BY	DATE	UNITS	SHEET NUMBER
LINDSAY HELFERICH	12/2/2020	INCHES	10 OF 14



PLAN VIEW
SCALE 2 : 1

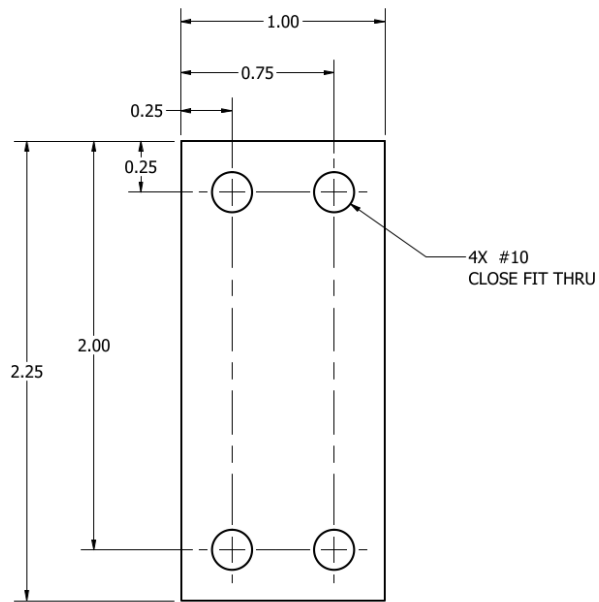


SIDE VIEW
SCALE 2 : 1

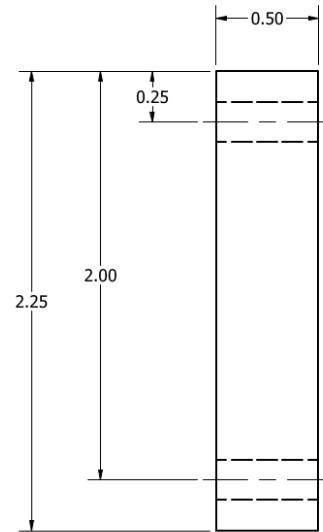


ISOMETRIC VIEW
SCALE 1 : 1

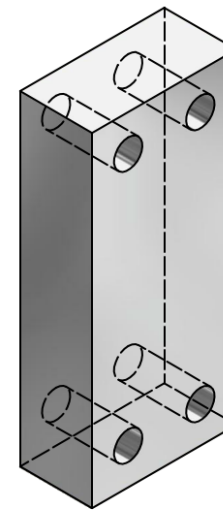
TITLE			
LVDT BRACE #3			
DEPARTMENT			PART MATERIAL
CIVIL & ENVIRONMENTAL ENGINEERING - STRUCTURAL			ALUMINUM
DESIGNED BY	DATE	UNITS	SHEET NUMBER
LINDSAY HELFERICH	12/2/2020	INCHES	11 OF 14



PLAN VIEW
SCALE 2 : 1

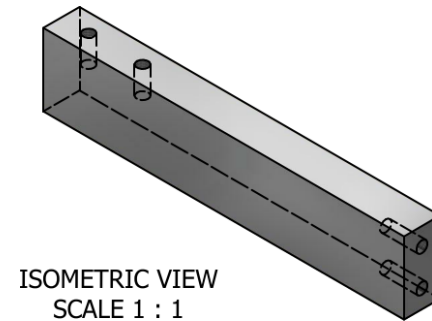
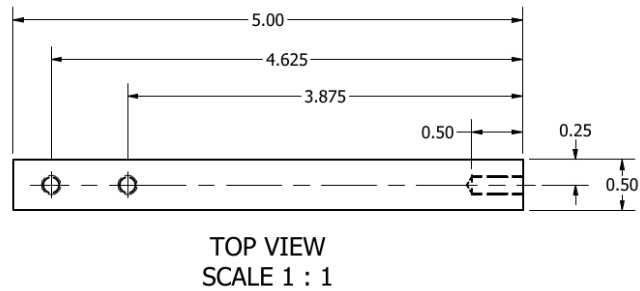
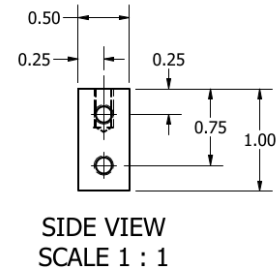
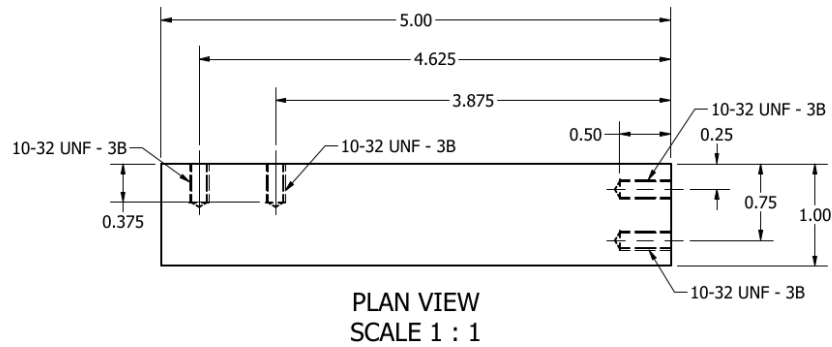


SIDE VIEW
SCALE 2 : 1

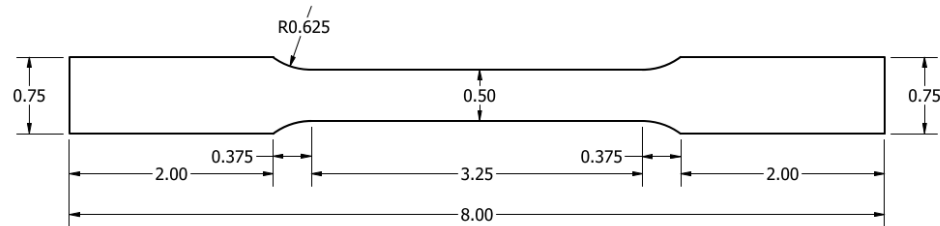


ISOMETRIC VIEW
SCALE 2 : 1

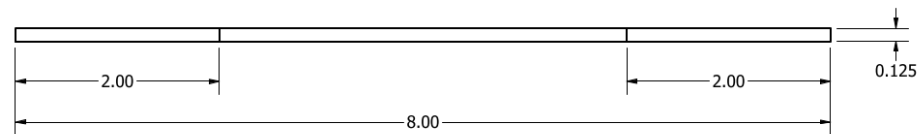
TITLE			
LVDT BRACE #4			
DEPARTMENT			PART MATERIAL
CIVIL & ENVIRONMENTAL ENGINEERING - STRUCTURAL			ALUMINUM
DESIGNED BY	DATE	UNITS	SHEET NUMBER
LINDSAY HELFERICH	12/2/2020	INCHES	12 OF 14



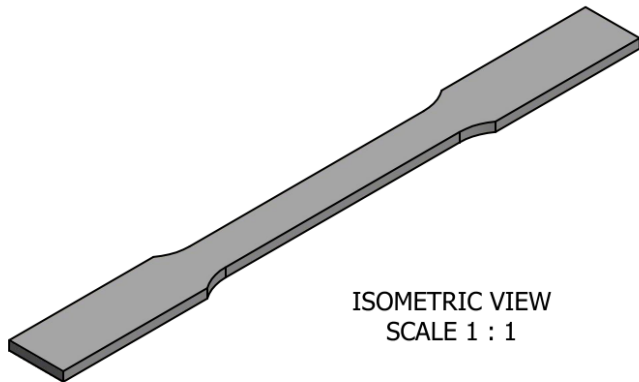
TITLE			
LVDT BRACE #5			
DEPARTMENT			PART MATERIAL
CIVIL & ENVIRONMENTAL ENGINEERING - STRUCTURAL			ALUMINUM
DESIGNED BY	DATE	UNITS	SHEET NUMBER
LINDSAY HELFERICH	12/2/2020	INCHES	13 OF 14



PLAN VIEW
SCALE 1 : 1



SIDE VIEW
SCALE 1 : 1



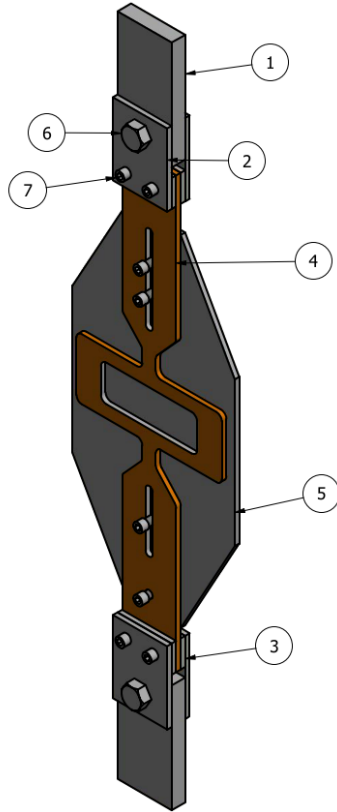
ISOMETRIC VIEW
SCALE 1 : 1

NOTES:

1. This piece is to be fabricated via waterjet cutting.

TITLE			
DOG BONE - TENSION TEST			
DEPARTMENT			PART MATERIAL
CIVIL & ENVIRONMENTAL ENGINEERING - STRUCTURAL			STEEL
DESIGNED BY	DATE	UNITS	SHEET NUMBER
LINDSAY HELFERICH	12/2/2020	INCHES	14 OF 14

Appendix B



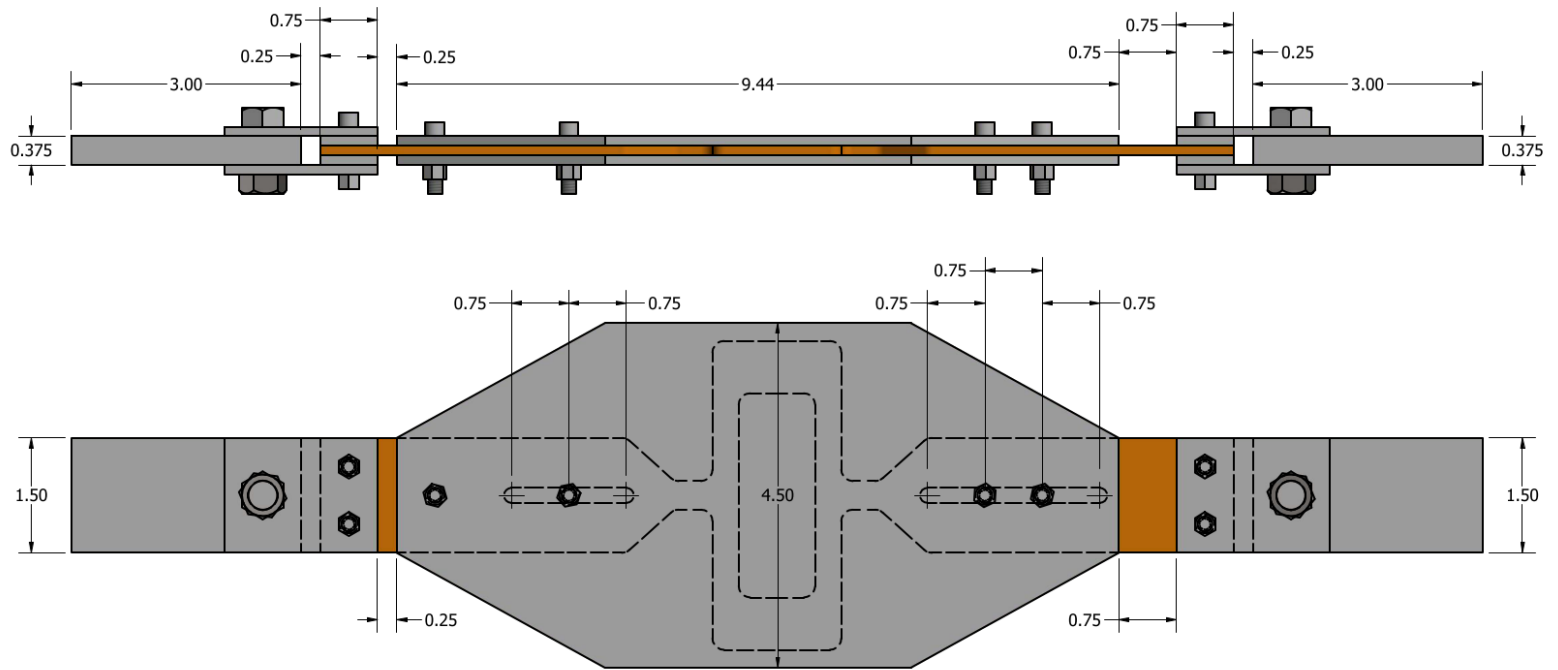
NOTE: Top confining plate not shown for clarity.

NEW FABRICATED PARTS			
Item Number	Part Description	Qty	Page Number
4	Yielding Plate	2	6 & 7
5	Confining Plate	2	8 & 9

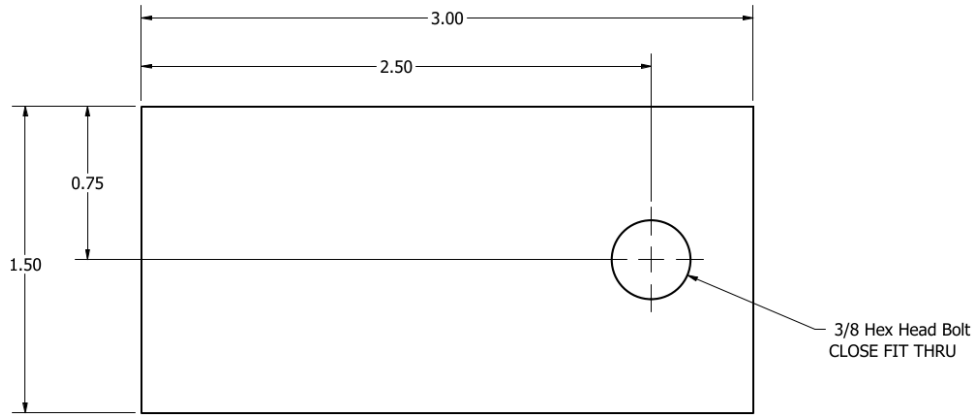
PREVIOUSLY FABRICATED PARTS			
Item Number	Part Description	Qty	Page Number
1	Grip Plate	2	3
2	Splice Plate	4	4
3	Filler Plate	4	5

PREVIOUSLY PURCHASED PARTS				
Item Number	Part Description	Qty	Part Number	Supplier
6	1" Lg. 3/8"-24 Class 2A Gr. 8 Steel Hex Head Screw	2	92620A655	McMaster-Carr
7	1" Lg. 10-32 Class 3A 18-8 Stainless Steel Socket Head Screw	12	92196A274	McMaster-Carr
8	3/8"-24 Class 2B Gr. 8 Steel Hex Nut	2	94895A815	McMaster-Carr
9	10-32 Class 3B 18-8 Stainless Steel Hex Nut	4	91834A105	McMaster-Carr

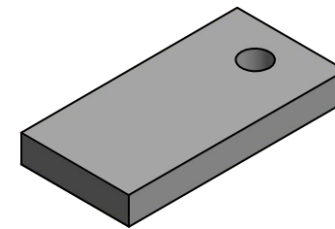
TITLE			
BUCKLING RESTRAINED BRACE - COMPONENT TEST			
DEPARTMENT			PART MATERIAL
CIVIL & ENVIRONMENTAL ENGINEERING - STRUCTURAL			STEEL
DESIGNED BY	DATE	UNITS	SHEET NUMBER
LINDSAY HELFERICH	3/31/2021	INCHES	1 OF 9



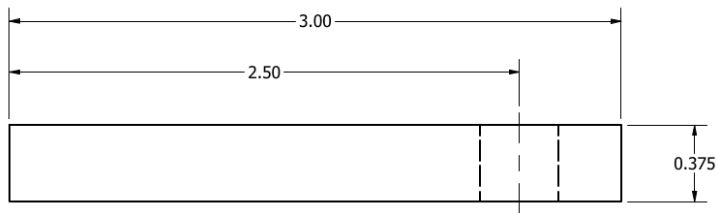
TITLE			
ALTERNATE VIEWS			
DEPARTMENT			PART MATERIAL
CIVIL & ENVIRONMENTAL ENGINEERING - STRUCTURAL			STEEL
DESIGNED BY	DATE	UNITS	SHEET NUMBER
LINDSAY HELFERICH	3/31/2021	INCHES	2 OF 9



PLAN VIEW
SCALE 2 : 1

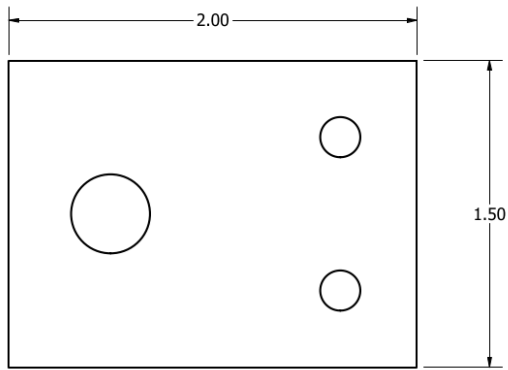


ISOMETRIC VIEW
SCALE 1 : 1

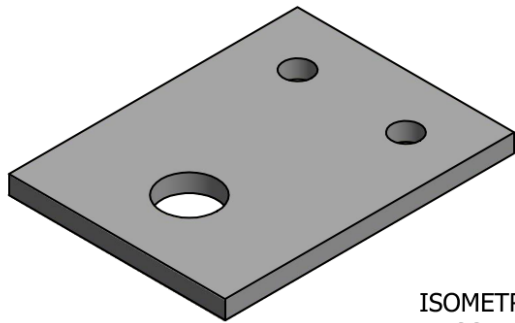


SIDE VIEW
SCALE 2 : 1

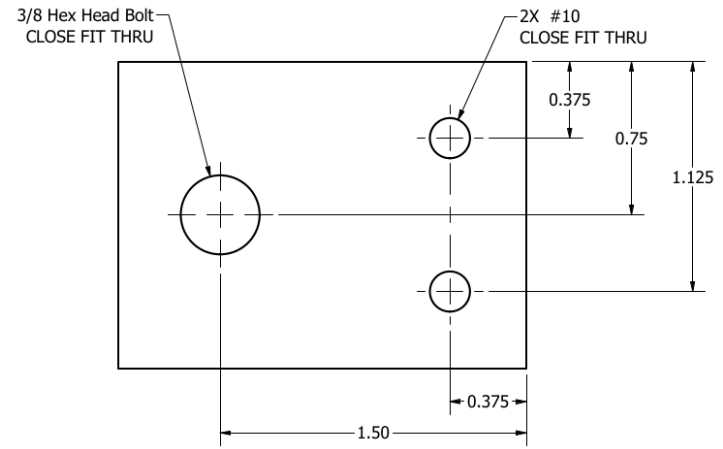
TITLE			
GRIP PLATE			
DEPARTMENT			PART MATERIAL
CIVIL & ENVIRONMENTAL ENGINEERING - STRUCTURAL			STEEL
DESIGNED BY	DATE	UNITS	SHEET NUMBER
LINDSAY HELFERICH	3/31/2021	INCHES	3 OF 9



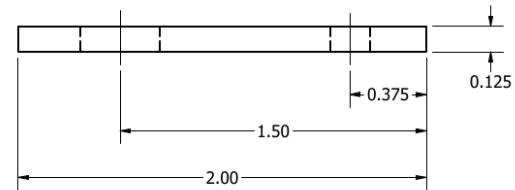
PLAN VIEW - GEOMETRY
SCALE 2 : 1



ISOMETRIC VIEW
SCALE 2 : 1



PLAN VIEW - HOLE DIMENSIONS
SCALE 2 : 1

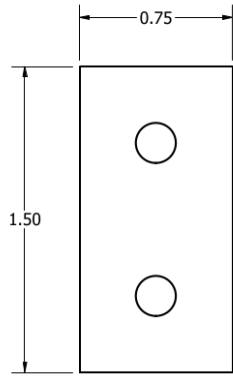


TOP VIEW
SCALE 2 : 1

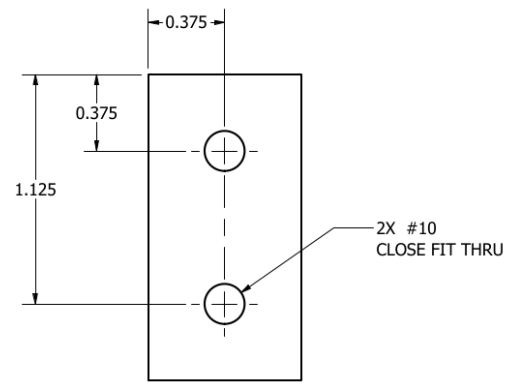
NOTES:

1. This piece is to be fabricated via waterjet cutting.

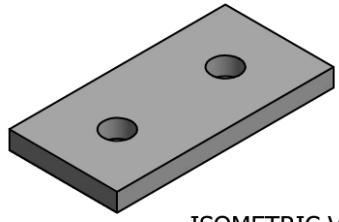
TITLE			
SPLICE PLATE			
DEPARTMENT			PART MATERIAL
CIVIL & ENVIRONMENTAL ENGINEERING - STRUCTURAL			STEEL
DESIGNED BY	DATE	UNITS	SHEET NUMBER
LINDSAY HELFERICH	3/31/2021	INCHES	4 OF 9



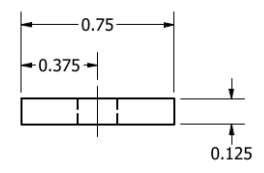
PLAN VIEW - GEOMETRY
SCALE 2 : 1



PLAN VIEW - HOLE DIMENSIONS
SCALE 2 : 1



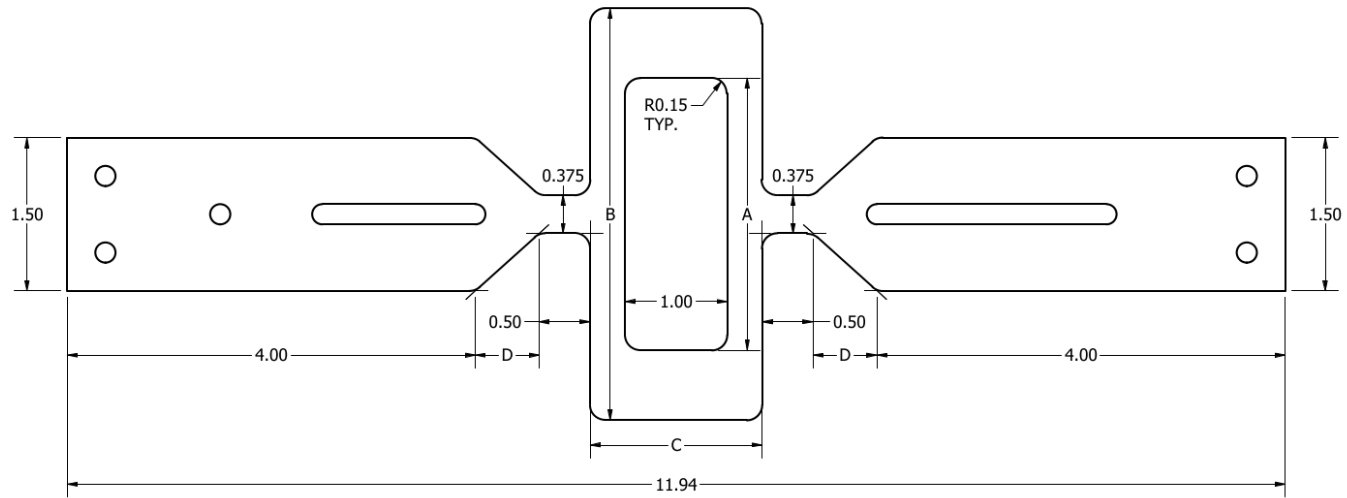
ISOMETRIC VIEW
SCALE 2 : 1



TOP VIEW
SCALE 2 : 1

NOTES:
1. This piece is to be fabricated via waterjet cutting.

TITLE			
FILLER PLATE			
DEPARTMENT			PART MATERIAL
CIVIL & ENVIRONMENTAL ENGINEERING - STRUCTURAL			STEEL
DESIGNED BY	DATE	UNITS	SHEET NUMBER
LINDSAY HELFERICH	3/31/2021	INCHES	5 OF 9



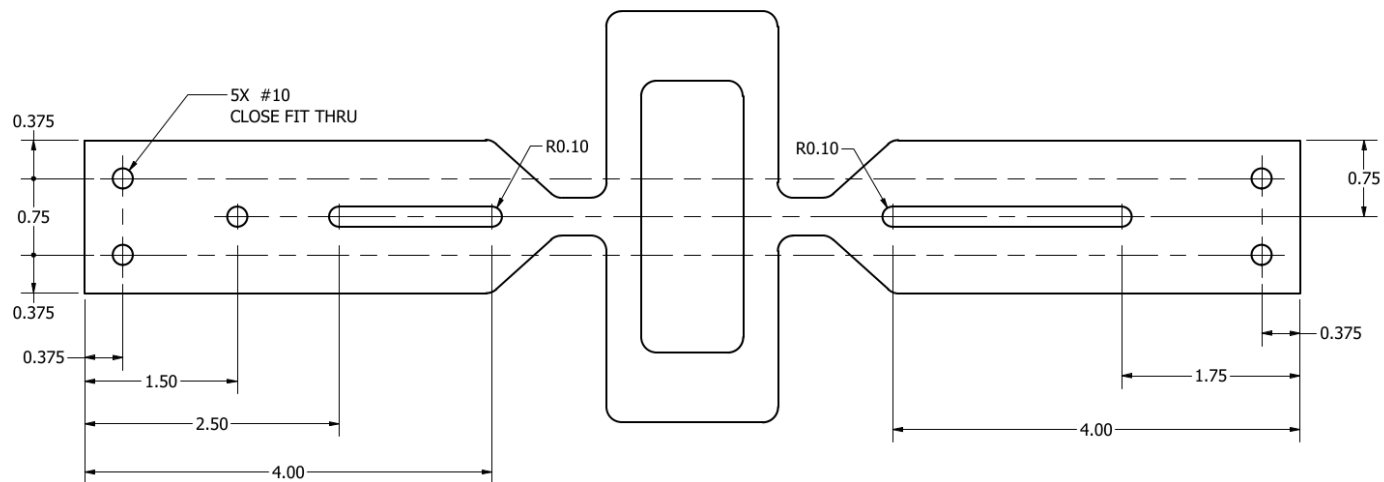
PLAN VIEW
SCALE 1 : 1

YIELDING PLATE DIMENSIONS				
PLATE NUMBER	DIMENSION "A"	DIMENSION "B"	DIMENSION "C"	DIMENSION "D"
1	2.295	2.979	1.342	0.799
2	2.665	4.033	1.684	0.628

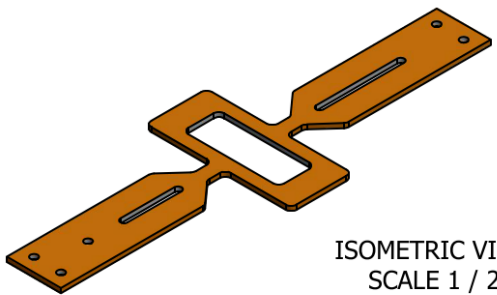
NOTES:

1. This piece is to be fabricated via waterjet cutting.
2. The same 11-gauge A1011-CS-B steel as previous shall be used.
3. Hole geometry and dimensions are shown on sheet 7.

TITLE			
YIELDING PLATE - SHEET 1			
DEPARTMENT		PART MATERIAL	
CIVIL & ENVIRONMENTAL ENGINEERING - STRUCTURAL		A1011-CS-B STEEL	
DESIGNED BY	DATE	UNITS	SHEET NUMBER
LINDSAY HELFERICH	3/31/2021	INCHES	6 OF 9

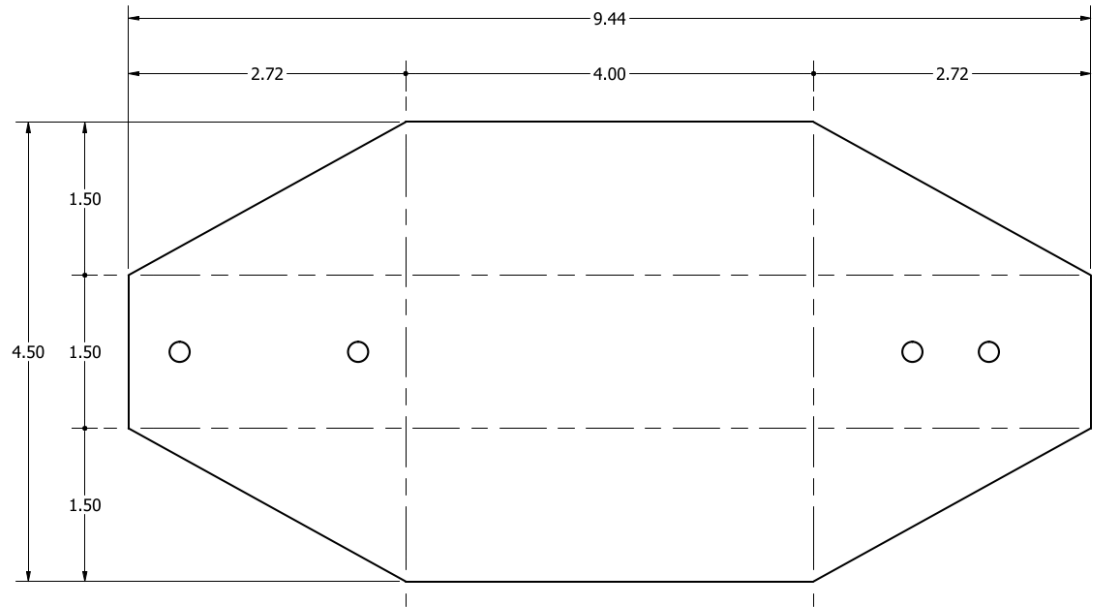


PLAN VIEW
SCALE 1 : 1



ISOMETRIC VIEW
SCALE 1 / 2

TITLE			
YIELDING PLATE - SHEET 2			
DEPARTMENT			PART MATERIAL
CIVIL & ENVIRONMENTAL ENGINEERING - STRUCTURAL			STEEL
DESIGNED BY	DATE	UNITS	SHEET NUMBER
LINDSAY HELFERICH	3/31/2021	INCHES	7 OF 9

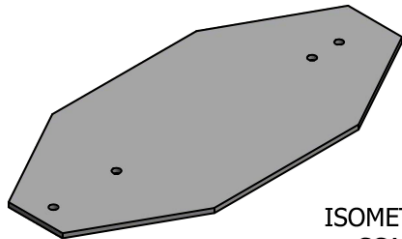
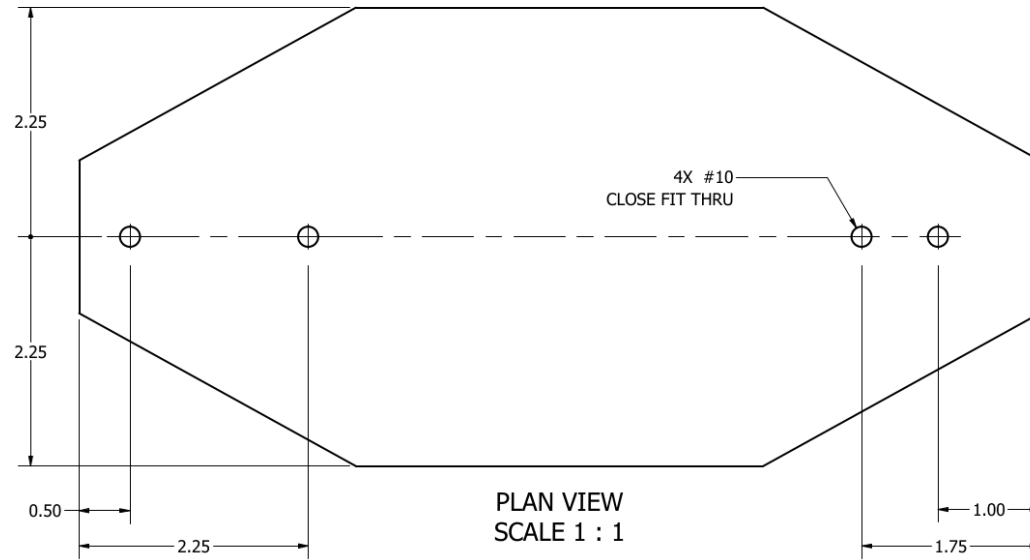


PLAN VIEW
SCALE 1 : 1

NOTES:

1. This piece is to be fabricated via waterjet cutting.
2. The same 11-gauge A1011-CS-B steel as previous shall be used.
3. Hole geometry and dimensions are shown on sheet 9.

TITLE			
CONFINING PLATE - SHEET 1			
DEPARTMENT			PART MATERIAL
CIVIL & ENVIRONMENTAL ENGINEERING - STRUCTURAL			STEEL
DESIGNED BY	DATE	UNITS	SHEET NUMBER
LINDSAY HELFERICH	3/31/2021	INCHES	8 OF 9



ISOMETRIC VIEW
SCALE 1 / 2

TITLE			
CONFINING PLATE - SHEET 2			
DEPARTMENT			PART MATERIAL
CIVIL & ENVIRONMENTAL ENGINEERING - STRUCTURAL			STEEL
DESIGNED BY	DATE	UNITS	SHEET NUMBER
LINDSAY HELFERICH	3/31/2021	INCHES	9 OF 9

Vita

Lindsay Helferich is originally from the great state of Texas where she attended Odessa High School and graduated as valedictorian of her class. She moved to the slightly colder state of Nebraska to continue both her education and her athletic career as a competitive swimmer. She initially studied architecture but switched to civil engineering after learning she enjoyed mechanics more than aesthetics. She graduated with her Bachelor of Science in Civil Engineering in May 2019. She then moved to Tennessee to pursue her Master of Science in Civil Engineering at the University of Tennessee. She will graduate in July 2021 and begin her career as a structural engineer at Haines Structural Group.